

**EXPERIMENTAL INVESTIGATION AND NUMERICAL
MODELING OF MICROPOROSITY FORMATION IN
ALUMINUM ALLOY A356**

by
LU YAO

A THESIS SUBMITTED IN PARTIAL FULFILLMENT OF
THE REQUIREMENTS FOR THE DEGREE OF

DOCTOR OF PHILOSOPHY

in

THE FACULTY OF GRADUATE STUDIES

(Materials Engineering)

THE UNIVERSITY OF BRITISH COLUMBIA

(Vancouver)

July 2011

© Lu Yao 2011

Abstract

Microporosity refers to small voids in the material in the size range from a few to hundreds of micrometers. These small voids can reduce the fatigue performance of the cast components. In the foundry industry, numerous efforts have been made to predict and control microporosity formation.

The present work studies the formation of microporosity in A356 (Al-7wt%Si-0.3wt%Mg) aluminum alloy castings. The focus is on prediction of pore size distribution, which is a crucial factor in fatigue analysis. This requires precise experimental characterization of pore size and simulation of both nucleation and growth kinetics of the pores.

In the initial stage of this work, microporosity formed in directionally solidified tapered cylindrical A356 casting samples were analyzed using high resolution X-ray microtomography (XMT). The results showed that increasing the cooling rate and degassing time yields lower microporosity within the microstructure.

These microporosity data were later used to validate a numerical model that simulates microporosity formation in A356 castings. In this model, the nucleation site distribution of the pores is a Gaussian function of hydrogen supersaturation in the melt. The pore growth is a hydrogen-diffusion controlled process. With the model it is possible to evaluate the relative contributions of hydrogen content, cooling rate and nucleation sites to microporosity formation, and to quantify the pore nucleation kinetics at given casting conditions.

Furthermore, this model was applied to study the effect of oxide inclusions on pore nucleation kinetics. Castings were prepared under different casting conditions aimed at manipulating the tendency to form and entrain oxides in the melt. Two alloy variants of A356 were tested in which the main difference was Sr content. By fitting the experimental results with the pore formation model, an estimate of the pore nucleation

site distribution has been made. It is shown increasing the tendency to form oxide films increases both the number and potency of nucleation sites. Based on the model prediction, Sr-modification impacts both the pore nucleation and pore growth kinetics.

Preface

This thesis includes, but is not limited to, materials from three manuscripts (Chapters 4-6). One manuscript (Chapter 4) has been published, one (Chapter 5) has been accepted and one (Chapter 6) is currently under peer-review by a journal in this field of research.

Published manuscript:

O. Lashkari, L. Yao, S.L. Cockcroft, D.M. Maijer, “X-Ray Microtomographic Characterization of Porosity in Aluminum Alloy A356”, *Metallurgical and Materials Transactions A: Volume 40, Issue 4 (2009)*, Page 991

Accepted manuscript:

Lu Yao, Steve Cockcroft, Jindong Zhu and Carl Reilly, “Modeling of Microporosity Size Distribution in A356 Tapered Cylinder Castings”, *Metallurgical and Materials Transactions A*, May 2011

In Chapter 4, the optical metallographic analysis and determination of threshold in XMT analysis were performed by the first author of the manuscript, Omid Lashkari. I completed the rest of the XMT data analysis including error assessment, measurement of pore size distribution and volume fraction.

In Chapter 5 and 6, I am the primary contributor to developing the model, performing the experiments, collecting data, analyzing the results and drafting the text and figures. My supervisor, Dr. Steve Cockcroft, the second author of both manuscripts, offered detailed advice on model development, experimental procedures, analysis methods, result interpretation and writing of the manuscripts. The other co-authors provided feedback and comments during implementation of these studies and acted as reviewers of the manuscripts.

Table of Contents

Abstract.....	ii
Preface.....	iv
Table of Contents.....	v
List of Tables.....	viii
List of Figures.....	ix
List of Symbols.....	xii
List of Subscripts and Superscripts.....	xiii
Acknowledgements.....	xiv
1 Introduction.....	1
1.1 Aluminum and aluminum alloys.....	1
1.1.1 History.....	1
1.1.2 Properties and applications.....	2
1.1.3 Aluminum casting process and casting-related defects.....	5
1.2 Porosity in aluminum alloy castings.....	7
2 Thesis Objectives and Scope.....	11
3 Literature Review.....	13
3.1 Microporosity in aluminum alloy castings.....	13
3.1.1 Classification of microporosity in aluminum alloy castings.....	13
3.1.2 Effect of microporosity on fatigue performance.....	15
3.2 Pore nucleation.....	17
3.2.1 Microporosity nucleation in aluminum alloy castings.....	17
3.2.2 Homogenous and heterogeneous nucleation theories.....	21
3.2.3 Bi-film entrainment theory.....	24
3.3 Pore growth.....	26
3.3.1 Equilibrium conditions.....	27
3.3.2 Pressure-drop controlled growth.....	28
3.3.3 Diffusion controlled growth.....	29
3.3.4 The role of impingement on pore growth.....	30
3.4 Factors affecting microporosity formation.....	31
3.4.1 Initial hydrogen concentration.....	31
3.4.2 Cooling conditions.....	33
3.4.3 Inclusion content.....	34
3.4.4 Alloy composition.....	35
3.4.5 Ambient pressure.....	36
3.5 Microporosity analysis.....	36
3.5.1 Optical microscopic analysis.....	36
3.5.2 X-ray microtomography (XMT) analysis.....	37
3.5.3 Scanning electron microscopic (SEM) analysis.....	39
3.6 Modelling of microporosity formation.....	40
3.6.1 Criterion functions.....	40

3.6.2	Interdendritic flow shrinkage models	41
3.6.3	Diffusion controlled pore growth models	43
3.6.4	Integrated macro-scale interdendritic flow and micro-scale diffusion controlled growth models	44
3.6.5	Cellular automata (CA) model.....	46
4	X-ray Micro-tomographic (XMT) Characterization of Microporosity in A356 Aluminum Alloy Castings	48
4.1	Experimental methods	48
4.1.1	Casting procedures.....	48
4.1.2	3-D XMT analysis.....	50
4.1.3	2-D optical analysis.....	51
4.2	Results and discussions.....	52
4.2.1	Solidification conditions	52
4.2.2	Assessment of errors in XMT analysis	55
4.2.3	Comparison between XMT and OM analysis.....	60
4.2.4	Effect of cooling rates and hydrogen content on porosity fraction.....	64
4.2.5	Effect of cooling rates and hydrogen content on pore size distribution ...	66
4.3	Summary and conclusions	70
5	Development of a Numerical Model for Prediction of Microporosity Formation in Aluminum Alloy Castings	71
5.1	Features of the microporosity model	71
5.1.1	Thermal-fluid flow model.....	72
5.1.2	Equilibrium condition	76
5.1.3	Pore nucleation.....	77
5.1.4	Hydrogen diffusion controlled pore growth	79
5.1.5	Solution technique	81
5.1.6	Novelty of the model	82
5.2	Results and discussions.....	83
5.2.1	Validation of the thermal model	83
5.2.2	Pore volume fraction.....	86
5.2.3	Pore size distribution.....	87
5.2.4	Determination of the fitting parameters.....	90
5.3	Numerical model analysis.....	92
5.3.1	Sensitivity of the model to initial pore radius (r_0)	92
5.3.2	The sensitivity to A , ss_0 and σ	94
5.3.3	The sensitivity to m and γ	98
5.3.4	The effect of the cooling rate.....	101
5.3.5	The effect of the initial hydrogen content.....	102
5.4	Summary and conclusions	103
6	Factors Affecting Nucleation Kinetics of Microporosity Formation in A356 Aluminum Alloy Castings	105
6.1	Experimental method.....	105
6.1.1	Casting procedures.....	106
6.1.2	Inclusion analysis.....	109

6.1.3	X-ray micro-tomography (XMT) analysis.....	110
6.2	Fitting procedure.....	111
6.3	Experimental results.....	114
6.3.1	Inclusion analysis based on PoDFA measurement.....	114
6.3.2	Microporosity analysis from XMT measurement.....	117
6.4	Mathematical model analysis.....	121
6.4.1	Determination of fitting parameter m	122
6.4.2	Determination of nucleation parameters.....	123
6.4.3	Model fit to experimental data.....	124
6.4.4	Pore nucleation kinetics.....	126
6.5	Summary and conclusions.....	129
7	Summary and Conclusions.....	132
7.1	Conclusions.....	132
7.2	Future work.....	134
	Reference.....	136

List of Tables

Table 1.1: Comparison of the physical properties of aluminum with iron and copper [8].	3
Table 1.2: Major aluminum wrought and cast alloys and their typical applications [10].	4
Table 1.3: Typical defects found in aluminum alloy castings [11-15].	6
Table 3.1: Summary of quantitative impurity analysis techniques[98].	34
Table 4.1: Nominal chemical analysis of the aluminum alloy A356 (wt%).	49
Table 4.2: Hydrogen content as a function of degassing time	50
Table 4.3: Procedures for preparation of metallographic samples	52
Table 5.1: Physical parameters in the thermal-fluid flow and microporosity model.	76
Table 5.2: Sensitivity of pore volume fraction f_p , average pore radius r_{avg} and maximum pore radius r_{max} to different parameters in the model.	95
Table 6.1: Description of casting conditions	107
Table 6.2: Chemical composition analysis for A356 aluminum alloy samples cast at local foundry (LF) and UBC (weight percentage).	109
Table 6.3: Results from PoDFA analysis showing major inclusions found in samples cast at local foundry (LF) and UBC.	115

List of Figures

Figure 1.1: World primary production (unit: millions of tons) of aluminum and other major non-ferrous metals in 2010 [7].	2
Figure 1.2: Macroshrinkage pores at a hot-spot area (spoke-rim junction cross section) of a Al-10wt%Si alloy cast in a permanent mold [31].	7
Figure 3.1: Solubility of hydrogen in aluminum at 1 atm pressure [11].	14
Figure 3.2: (a) Optical micrograph and (b) SEM image of hydrogen induced microporosity in Al-Si alloy ; (c) optical micrograph and (d) SEM image of interdendritic microshrinkage in Al-Si alloy; [42] (e) a shrinkage pore and a gas pore merged together to form a single pore[43].	15
Figure 3.3: Effect of altering the solidification velocity (low, medium and high from top to bottom in the graphs) on (a) nucleation temperature and (b) growth rates of the pores in Al-7wt%Si alloy [57].	19
Figure 3.4: Sequence of X-ray radiographs showing the formation of gas porosity in a directionally solidified Al-30wt%Cu alloy [61].	20
Figure 3.5: Variation of the system free energy with radius of the potential pore.	22
Figure 3.6: Schematic of (a)-(c) heterogeneous nucleation of a gas pore on a solid substrate; (d) $S(\theta) = (2 - \cos\theta)(1 + \cos\theta)^2 / 4$ as a function of contact angle.	23
Figure 3.7: (a) Schematic illustration of bi-films with their trapped air bubbles. (b) (c) Comparison of x-ray radiographs taken at same time after pouring from same melt of Al-7Si-0.4Mg alloy subjected to solidification under pressure (b) 1 atmosphere, showing diffuse images of furled bi-films; and (c) 0.01 atmosphere showing unfurled bi-films [67].	25
Figure 3.8: Schematic of all pressures applied on an isolated pore in equilibrium in the bulk liquid.	28
Figure 3.9: Schematic representation of: (a) a 1D columnar mushy zone; (b) temperature and pressure profiles (gravity g is towards left); (c) effective gas concentration $[H]_l$ and gas solubility limit $[H]_l^*$ in the liquid [72].	29
Figure 3.10: Schematic showing the hydrogen concentration profile at a hydrogen diffusion boundary layer around a growing pore.	30
Figure 3.11: Schematic of (a) gas fluxing and (b) rotary degassing in molten aluminum [87].	33
Figure 3.12: Schematic image of a shrinkage pore and the resulting two-dimensional image when sectioned [126].	37
Figure 4.1: Schematic of the mold configuration and the thermocouple positions.	50
Figure 4.2: Cooling curves at different distances from the chill in the 0.5, 1.0 and 2.0 min degassed samples.	54
Figure 4.3: Cooling rates during solidification as a function of distance from the chill.	55
Figure 4.4: (a) Sample X-ray tomographic image of the cast metal and porosity, (b) typical color intensity versus grayscale values for a X-ray tomography image, (c) Porosity, assuming grayscale threshold of 238, (d) Porosity, assuming greyscale threshold of 218, and (e) Porosity, assuming greyscale threshold of 198.	57
Figure 4.5: Variation of measured pore volume fraction with sample sizes in the 3-D XMT analysis.	58
Figure 4.6: Pore size distributions in a volume of (a) 25.7 mm ³ and (b) 12.9 mm ³ from the XMT analysis.	59

Figure 4.7: Variation of porosity fraction as a function of distance from the chill for the 0.5-min degassed sample.	60
Figure 4.8: The pore size distribution for the 0.5-min degassed sample based on (a) the radius of a spherical pore occupying the same volume from 3-D XMT measurement and (b) a circular pore occupying the same area from 2-D OM measurement.	62
Figure 4.9: Porosity fraction at different distances from the chill at high, medium and low hydrogen contents.	64
Figure 4.10: Porosity fraction as a function of cooling rate at high, medium and low hydrogen contents.	66
Figure 4.11: (a) 3-D rendering of the pores and (b) pore size distribution at different height in the 0.5-min degassed sample with an initial hydrogen content 0.32 ppm.	67
Figure 4.12: (a) 3-D rendering of the pores and (b) pore size distribution at different height in the 1.0-min degassed sample with an initial hydrogen content 0.20 ppm.	68
Figure 4.13: (a) 3-D rendering of the pores and (b) pore size distribution at different height in the 2.0-min degassed sample with an initial hydrogen content 0.11 ppm.	69
Figure 5.1: Schematic illustrating coupling of macro-scale thermal-fluid flow model with the millimeter-scale porosity model.	72
Figure 5.2: (a) Effective viscosity μ_{eff} [159] and (b) permeability K [152] as functions of temperature.	75
Figure 5.3: Schematic of a hydrogen diffusion boundary layer around a growing pore where the linear gradient approximation is applied.	81
Figure 5.4: Comparison between the measured and predicted cooling curves at different distances from the chill for (a) 0.5-min degassed and (b) 1.0-min degassed samples.	85
Figure 5.5: Heat transfer coefficient determined by fitting to the measured cooling curves using a trial-and-error approach.	85
Figure 5.6: Comparison between predicted and measured variation in porosity fraction as a function of distance from the chill in the 0.5-min and 1.0-min degassed samples.	87
Figure 5.7: Comparison between measured and predicted pore size distribution at different distances from the chill in the 0.5-min degassed sample.	88
Figure 5.8: Comparison between measured and predicted pore size distribution at different distances from the chill in the 1.0-min degassed sample.	89
Figure 5.9: m in the impingement factor as a function of cooling rate derived by fitting the model predictions with experimental measurement.	91
Figure 5.10: Pore nucleation site distribution at different degassing time derived by fitting the model predictions with experimental measurement.	92
Figure 5.11: Sensitivity of (a) pore size distribution, (b) pore volume fraction, average and maximum pore radius to initial pore radius.	93
Figure 5.12: Sensitivity of (a) pore size distribution, (b) pore volume fraction, average and maximum pore radius to A	95
Figure 5.13: Sensitivity of (a) pore size distribution, (b) pore volume fraction, average and maximum pore radius to ss_0	96
Figure 5.14: Sensitivity of (a) pore size distribution, (b) pore volume fraction, average and maximum pore radius to σ	97

Figure 5.15: Sensitivity of (a) pore size distribution, (b) pore volume fraction, average and maximum pore radius to m	99
Figure 5.16: Sensitivity of (a) pore size distribution, (b) pore volume fraction, average and maximum pore radius to γ	101
Figure 6.1: Schematic of the experiment setup for (a) normal pouring (NP), (b) Ar shielded pouring (ArP) and (c) high surface area pouring (HSAP) conditions. ...	107
Figure 6.2: (a) Schematic showing the principle of the porous disc filtration apparatus (PoDFA) and (b) a PoDFA sample showing the layer of residual metal, the concentrated inclusions and the filter[166]......	110
Figure 6.3: (a) Optical and (b) SEM image with (c) EDX analysis of a micrometer scale oxide film in the PoDFA samples.	116
Figure 6.4: An example of EDX mapping analysis that shows presence of oxygen associated with pores in (a) PoDFA samples and (b) casting samples.	117
Figure 6.5: Comparison between measured (symbol) and predicted (dashed line) (a) pore number density and (b) volume fraction in samples resulted from normal pouring (LF-NP) and Ar shielded pouring (LF-ArP) conditions.	118
Figure 6.6: Comparison between measured (shaded bars) and predicted (un-shaded bars) pore size distribution at different distances from the chill in samples resulted from (a) normal pouring (LF-NP) and (b) Ar shielded pouring (LF-ArP) conditions.	119
Figure 6.7: Comparison between measured (symbol) and predicted (dashed line) (a) pore number density and (b) volume fraction in samples resulted from normal pouring (UBC-NP) and high-surface-area pouring (UBC-HSAP) conditions.	120
Figure 6.8: Comparison between measured (shaded bars) and predicted (un-shaded bars) pore size distribution at different distances from the chill in samples resulted from (a) normal pouring (UBC-NP) and (b)high-surface-area pouring(UBC-HSAP) conditions.	121
Figure 6.9: m in the impingement factor as a function of cooling rate determined by fitting the model predictions with experimental measurement.	123
Figure 6.10: Optical micrograph of as-cast microstructures in samples resulted from different metal sources at (a) local foundry (LF) and (b) UBC.	123
Figure 6.11:Plots showing residual R as a function of ss_0 and σ used in the coarse fitting process for samples (a) LF-NP, (b) LF-ArP, (c) UBC-NP and (d) UBC- HSAP. ...	125
Figure 6.12: Pore nucleation site distribution under various casting conditions derived by fitting the model predictions with experimental measurement.	126

List of Symbols

C_l (mol/m ³)	hydrogen concentration in the bulk liquid
Δp (N/m ²)	pressure change
r (m)	pore radius
γ (N/m)	surface tension
θ (°)	contact angle
ΔG (J/mol)	energy barrier for pore nucleation
p (Pa)	pressure
C_{lp} (mol/m ³)	hydrogen concentration at the liquid/pore interface
K_L (mol/m ³ /atm ^{1/2})	equilibrium constant
ρ (kg/m ³)	density
h (m)	distance from the top of the casting
l_p (m)	average distance between the pores
l_{diff} (m)	thickness of the diffusion boundary layer
D_H (m ² /s)	hydrogen diffusion coefficient in the liquid phase
Δt (s)	solidification time or time step size
ϕ	impingement factor
f_s	solid fraction
f_l	liquid fraction
f_p	porosity fraction
m	fitting parameter in the impingement factor
G (°C/m)	thermal gradient
R (°C/s)	cooling rate
K (m ²)	permeability
μ (Pa·s)	viscosity
g (m ² /s)	gravitational acceleration
C_H^0 (mol/m ³)	initial hydrogen concentration
α (J/mol/K)	gas constant
k (W/m/K)	thermal conductivity or distribution coefficient
C_p (J/kg/K)	specific heat
L_m (J/kg)	latent heat
N_{nuc} (mm ⁻³)	number density of the nucleated pores
ss (mol/m ³)	supersaturation of hydrogen in the liquid
A (mm ⁻³)	total number of available nucleation sites
σ (mol/m ³)	deviation of nucleation site distribution
ss_0 (mol/m ³)	average hydrogen supersaturation required for pore nucleation

List of Subscripts and Superscripts

<i>a</i>	atmosphere
<i>d</i>	drop (in pressure)
<i>g</i>	gas phase
<i>h</i>	metallic head
H	hydrogen
<i>l</i>	liquid phase
<i>p</i>	pore
<i>s</i>	solid phase

Acknowledgements

This thesis would not have been completed without the guidance from my supervisor Professor Steven Cockcroft. I would like to express my gratitude for his support, patience and his effort for encouraging industrial collaboration throughout this project. I would also like to give thanks to Professor Daan Maijer for his involvement and advice during my studies and Dr. Jindong Zhu for the many helpful discussions.

I would like to acknowledge Canadian Autoparts Toyota Inc. (CAPTIN) and NSERC for the financial support, Rio Tinto Alcan for the in-kind support and the Swiss Light Source (SLS) at Paul Scherrer Institute (PSI) for the use of the TOMCAT beamline facilities. In particular, I would like to thank: Dr. Fred Major at Arvida Research & Development Center, Rio Tinto Alcan for loaning us the apparatus, providing access to the hydrogen analysis facility and giving technical advice on the assessment of melt cleanliness; Dominic Au and Ken Ng at CAPTIN for their effort to make the casting trials at CAPTIN possible and their assistance during my on-site visits; Andre Phillion at the University of British Columbia-Okanagon and Julie Fife at SLS, PSI for the arrangement and assistance on conducting the XMT experiment .

The graduate studies would be much more painful without help and advice from colleagues. I would like to give thanks to my group members, and many faculty and staff members in the department from whom I received assistance and training throughout my studies.

My deepest gratitude is to my parents and grandma, for their unconditional love and keeping me motivated. And friends with whom I share fun times and pieces of life. Special thanks to beautiful Vancouver for decorating this PhD journey with diverse life, fabulous Asian food and spectacular natural scenery.

1 Introduction

1.1 Aluminum and aluminum alloys

1.1.1 History

The history of aluminum is relatively short compared with metals such as iron and copper, which have been used for thousands of years. The existence of aluminum was first established only two hundred years ago in 1808 [1]. Another 17 years passed before it was produced. In the early years of its production, only tiny amounts of aluminum metal could be extracted, through an extremely complicated processes, due to aluminum's high affinity with oxygen [2]. The purity of aluminum obtained at that time can be questioned. It was not until 1845 that aluminum could be satisfactorily purified, and its low density, which distinguishes aluminum from the other metals, was established [3]. The first commercial process for extracting aluminum was created in 1854. However, the general application of aluminum was limited by its high cost, caused by its complex and time-consuming extraction process. In the 1800's aluminum was even more precious than gold and silver and was thus used in many luxury items (e.g., the aluminum watch chain presented by Napoleon to the King of Siam when he visited Paris) [4]. Throughout the late 1800s, the low density and high strength of aluminum gained increasing interest from around the world and numerous efforts were taken to facilitate research on its commercial production. In 1886, a new electrolytic process, called the Hall-Heroult process, was invented [5]. This process uses electrolytic cells to reduce the oxide to pure aluminum and lead to a dramatic reduction in the price of aluminum. It marks the beginning of modern aluminum production and still remains the fundamental method used today for commercial aluminum production [6]. The introduction of the Hall-

Heroult process and free enterprise in the aluminum industry has lead to aluminum becoming one of the most important engineering metals, indeed it is used in products ranging from aircraft and automobiles to house hold appliances.

Today more aluminum is produced than all other non-ferrous metals combined. In 2010, 36.9 million tons of aluminum, 15.8 million tones of copper, 3.9 million tons of lead and only 0.3 million tons of tin were commercially produced globally, as shown in Figure 1.1.

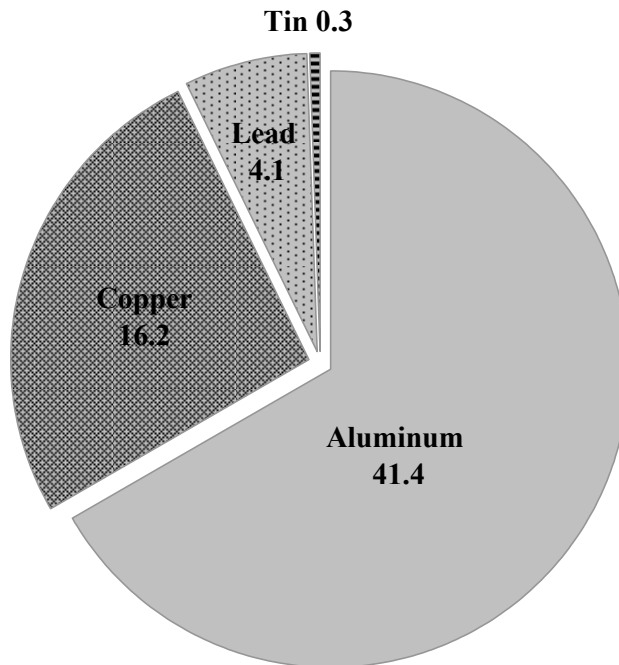


Figure 1.1: World primary production (unit: millions of tons) of aluminum and other major non-ferrous metals in 2010 [7].

1.1.2 Properties and applications

Its low density and high strength-to-weight ratio are the best known properties which distinguish aluminum from many other common engineering metals. Aluminum also has high corrosion resistance, ductility, thermal and electrical conductivity and an attractive

surface finish. Table 1.1 shows various physical properties of aluminum in comparison with iron and copper.

Table 1.1: Comparison of the physical properties of aluminum with iron and copper [8].

	density (g/cm ³)	melting point (°C)	boiling point (°C)	heat capacity (J/mol/K)	electrical resistivity (nΩ·m)	thermal conductivity (W/m/K)	thermal expansion (μm/m/K)	Young's modulus (GPa)	yield stress (MPa)	ultimate tensile strength (MPa)	Vickers hardness (MPa)
Al	2.7	660	2519	24.2	28.2	237	23.1	70	15-20	40-50	167
Fe	7.9	1538	2862	25.1	96.1	80	11.8	211	80-100	350	608
Cu	8.9	1084	2562	24.4	16.8	401	16.5	130	33	210	369

As can be seen in Table 1.1, pure aluminum has a relatively low yield stress and ultimate tensile stress. To increase its strength, aluminum is usually alloyed with other elements such as copper and magnesium. Based on the fabrication method, aluminum alloys are classified into two broad classes, wrought alloys and cast alloys [9]. Wrought alloys are those that are shaped by plastic deformation such as rolling, extruding, forging or drawing. These processes reduce the grain size of the microstructure and remove defects associated with the casting process, so that the mechanical properties of the components are improved. The other option, which is generally more economical, is to cast the alloy into its final or near-final shape. In the case of cast components, any defects resulting from the casting process can be carried over into the final product. Depending on the application of the component it may prove necessary to control or to minimize these defects, particularly in applications requiring mechanical performance including resistance to fatigue. Table 1.2 shows common aluminum wrought and cast alloys and their typical applications.

Table 1.2: Major aluminum wrought and cast alloys and their typical applications [10].

	alloy series	Composition	Ultimate tensile strength (MPa)	Heat treatable	Properties	Applications
Wrought	1xxx	Al	70 - 185	No	Exceptionally high formability, corrosion resistance, and electrical conductivity	Packaging, chemical equipment, electrical applications
	2xxx	Al-Cu	190-430	Yes	Low resistance to atmospheric corrosion	Aircraft, space shuttle
	3xxx	Al-Mn	110-285	No	High formability and corrosion resistance	Cooking utensils, heat exchanger, beverage cans
	4xxx	Al-Si	175-380	Yes	Low melting point, excellent flow characteristics	Forging, weld filler
	5xxx	Al-Mg	125-350	No	Excellent corrosion resistant, toughness and weldability	Building and construction, highway structures, marine application
	6xxx	Al-Mg-Si	120-400	Yes	High corrosion resistance, excellent extrudibility	Architectural and structural parts
	7xxx	Al-Zn-Mg(Cu)	220-610	Yes	High strength and toughness	Aircraft
Cast	2xx.x	Al-Cu	130-450	Yes	High strength at room and elevated temperatures, high toughness	Aerospace industry, machine tools, engine blocks, or bearings
	3xx.x	Al-Si(Cu/Mg)	130-275	Yes	Flexibility provided by the high silicon content	Aircraft, car wheels
	4xx.x	Al-Si	120-175	No	Excellent castability and weldability	Complex cast parts for computer housings and dental equipment
	5xx.x	Al-Mg	120-175	No	Good resistance to corrosion	Door and window fittings
	6xx.x	Al-Zn	210-380	Yes	Excellent finishing characteristics	Furniture, garden tools, office machines, and farming and mining equipment
	7xx.x	Al-Tin	105-210	Yes	Excellent machinability	Bushings and bearings

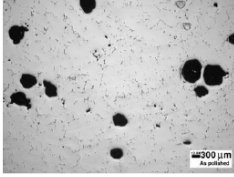
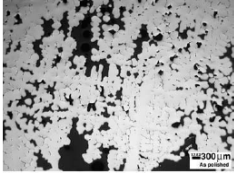
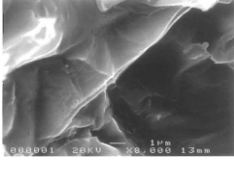
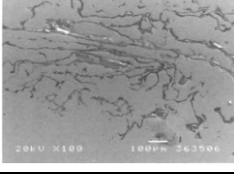
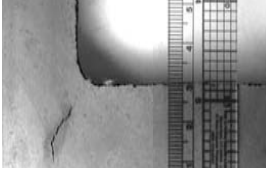
1.1.3 Aluminum casting process and casting-related defects

Aluminum casting processes can be classified into two broad categories: primary and secondary casting processes. The former is most commonly used to produce castings that are not the components final geometry. Primary casting products include rolling slab, extrusion billet and wire bar ingot which subsequently undergo further processing to transform into finished products. An example of a primary process is Direct Chill (DC) casting. The secondary casting processes are used to produce near net shape products. Examples of secondary casting processes include the sand casting, die casting and investment casting processes.

Aluminum alloy castings are particularly prone to the formation of void defects due to the high volume contraction (4-8%) associated with the liquid-to-solid transformation and the high hydrogen solubility in the liquid relative to the solid. They are also prone to oxide entrainment related defects owing to the high affinity of aluminum for oxygen. Depending on the application, it may be critical to control the formation of these defects as they can behave as stress concentrators and can significantly reduce the mechanical properties of the casting, particularly in applications requiring high mechanical performance such as resistance to fatigue failure.

Typical defects in aluminum include porosity, hot cracking and inclusions. It should be mentioned that the categorizations in Table 1.3. are not hard distinctions, e.g., a pore can be a result of both shrinkage and hydrogen dissolution effect. Also the oxide film inclusions in the melt may be associated with pore nucleation and be presented as substrate on which pores are formed.

Table 1.3: Typical defects found in aluminum alloy castings [11-15].

Type		Formation	Morphology	Size
Porosity	Hydrogen-induced	Hydrogen dissolution in the liquid metal		Micrometer-scale in diameter
	Shrinkage-induced	Lack of liquid feeding when directional solidification is lost		Can be as large as in millimeter-scale in thickness
Inclusions	Oxide film	Young oxide film		Nanometer-scale in thickness
		Old oxide film		Micrometer-scale in thickness
	Other exogenous inclusions	Entrained particles arising from furnace linings, die components and coatings, and upstream processes.		Micrometer-scale in thickness
Cracks	Hot tearing	Due to presence of thermal stresses in the semi-solid phase		Micrometer to millimeter in scale
	Cold cracking	Due to contraction-induced stress below the solidus temperature		Micrometer to millimeter in scale

1.2 Porosity in aluminum alloy castings

Porosity in aluminum alloys is a well known defect, which can cause cosmetic problems and reduce the ductility and fatigue performance of cast parts [16-30]. Porosity can be categorized by either its formation mechanism as hydrogen and shrinkage induced (Table 1.3), or by its size as macroporosity and microporosity. Macroporosity refers to pores with a diameter in the millimeter to centimeter scale. These relatively large pore sizes are the result of pore growth, which is driven by volume contraction of the solidifying alloy that cannot be compensated for by mass feeding during the solidification process. This happens when directional solidification is lost and a hot spot is formed. Hot spot is a term that is used in most literature to describe a region of liquid encapsulated within solidified metal in the castings. Figure 1.2 shows an example of pores formed in aluminum castings due to macroshrinkage. The other category, microporosity, refers to porosity in castings that is relatively small in scale, with a radius less than 500 μm . The formation of microporosity involves various micro-scale phenomena occurring during solidification such as the decrease in hydrogen solubility, entrainment of oxide film inclusions, the pressure drop in the mushy zone, insufficient interdendritic feeding, and the development of the solidification structure [15].

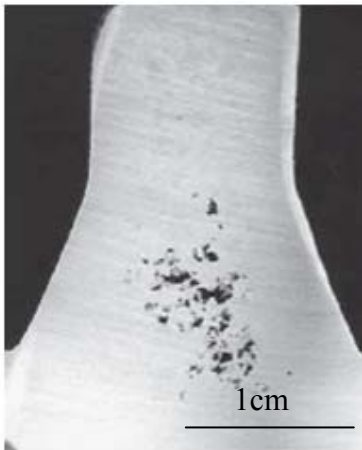


Figure 1.2: Macroshrinkage pores at a hot-spot area (spoke-rim junction cross section) of a Al-10wt%Si alloy cast in a permanent mold [31].

The quality issues related to porosity in aluminum castings include cosmetic problems and the degradation of mechanical properties. The former happens when the pores are visible at the surface of the castings and can be particularly problematic in castings that require application of paint or coatings such as automotive wheels. Although being difficult to control, cosmetic issues can normally be repaired. The effect of porosity on mechanical performance is more detrimental to castings. The features (e.g., location and severity) of porosity formation must be evaluated when assessing the mechanical properties of the casting components.

Porosity is known as a key factor that controls the fatigue properties of aluminum alloys. It is well known that the fatigue life of aluminum castings is sensitive to the size of microstructural defects (such as pores). For a given stress amplitude larger discrete pores increase the stress concentration and reduce the time spent on the crack initiation stage relative to smaller discrete pores [16, 19, 20, 22]. The distribution and location of the porosity within the casting is also an important factor in determining integrity of the component. The clustering of pores is generally undesirable as the stress concentration fields induced can result in material behavior equivalent to a material containing a much larger pore. In terms of location, the largest pore in the region exhibiting the largest peak tensile load in general determines the limit of the fatigue life [16, 23]. Therefore, the prediction of pore size is a crucial element in the evaluation of fatigue performance of cast components. The pore size distribution must be correctly represented to ensure accurate input data for prediction of fatigue life.

To this end, over the last three decades, increased attention has been focused on the prediction of porosity formation during the solidification process of aluminum alloy

castings. These studies have the potential to provide the foundry industry with useful tools for controlling porosity and therefore improving the mechanical properties of the cast components. Some studies are aimed at determining the mechanism and origin of porosity formation and hence better understand how to reduce the presence of the pores. For example, by being able to simulate porosity formation at a given hydrogen level and for a given mould filling process, foundry engineers may identify the cause and thus improve the casting by control of appropriate process parameters. One of the challenges in modeling porosity formation in aluminum alloy castings is the limited understanding of the nucleation mechanism of pores. In combination with the growth kinetics, pore nucleation kinetics is critical for predicting the size distribution of the pores.

A better understanding of the pore nucleation behavior is required for accurate pore size prediction modeling. Previous studies have shown that inclusions, especially oxide films, assist nucleation of the pores and thus have a significant influence on the initial stage of porosity formation [32-37]. Conventional theories suggest that oxide inclusions in the melt provide heterogeneous nucleation sites which reduce the nucleation energy barrier required for pore nucleation [33]. These inclusions provide unwetted surfaces on which supersaturated hydrogen precipitates to form gas cavities. Campbell proposed a nucleation-free mechanism for porosity formation in which the pores are formed when air is entrained in the melt within folded oxide films [14, 38-40]. This new theory has gained considerable attention in the field of aluminum alloy casting research even though there has been lack of direct experimental evidence because of the nanometer thickness and transparent nature of the oxide films involved in this process. The identification of the pore/oxide film interaction mechanism is still a subject of active research.

The focus of this study is on formation of hydrogen-induced microporosity in A356 (Al-7wt%Si-0.3wt%Mg) aluminum alloy with particular emphasis on nucleation kinetics. It is generally agreed that modeling of macroporosity has been well developed using existing heat transfer and fluid flow modeling techniques that determine when a volume can be completely cut off from sources of liquid metal [41]. Comparatively, the simulation of microporosity is less well developed and is more challenging due to its complex formation mechanisms, especially when considering the requirement of the maximum computational efficiency in the context of industrial applications. Existing models either make assumptions that over-simplify the pore formation process - e.g. pore nucleation kinetics and impingement between pores and solid dendrites are ignored - or examine pore formation in great detail at a high computational cost. To date, development of an industrially viable model accounting for various phenomena occurring during the manufacturing and solidification process requires further research.

2 Thesis Objectives and Scope

The objectives of this project are to study the formation of hydrogen-induced microporosity in A356 (Al-7wt%Si-0.3wt%Mg) aluminum alloy castings and to develop an application-oriented model to predict microporosity formation. The goal is to predict the final pore size distribution, which has been shown to significantly affect the fatigue behavior of the cast components. The specific sub-tasks of this project are:

- a. To precisely quantify and characterize microporosity using X-ray microtomography (XMT) methods and to compare the results to those obtained using conventional optical-based methods;
- b. To investigate the effect of cooling rate, degassing time and pouring conditions on microporosity formation in aluminum alloy A356 castings;
- c. To develop a model that predicts the size distribution and volume fraction of microporosity in A356 aluminum alloy castings under various casting conditions. The model should include both the nucleation and growth kinetics; it should be able to capture the effect of cooling rate, hydrogen content and pressure variation within the mushy regime;
- d. To provide a better understanding of pore nucleation process, especially the effect of oxide films on pore nucleation kinetics.

This thesis is organized as follows: Chapter 3 introduces key concepts that are used to describe microporosity formation mechanisms in the current literature. Well-recognized mathematical models that have been developed to simulate porosity formation are

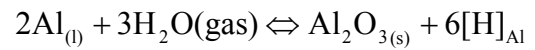
reviewed. In Chapter 4, the experimental procedures to produce a series of test castings made under directional solidification conditions with high, medium and low hydrogen content levels are described together with the procedures for the measurement of porosity fraction and pore size distribution in the test castings. Chapter 5 details the features and validation of the model that is developed for porosity prediction. Sensitivity analyses to the fitting parameters and pore-formation-related variables are also performed. Chapter 6 investigates the effects of oxide films/inclusions on microporosity nucleation and thus the final pore size distribution in directionally solidified A356 aluminum alloy castings poured using three different methods aimed at varying the entrained oxide film content. By fitting the experimental results against the porosity model, the variation of nucleation site distribution with inclusion content in the melt is revealed. Finally, Chapter 7 summarizes the result of the work and presents the conclusions and future work.

3 Literature Review

3.1 Microporosity in aluminum alloy castings

3.1.1 Classification of microporosity in aluminum alloy castings

Depending on the driving force for its formation, microporosity in castings can be categorized as being either gas or shrinkage induced. Since hydrogen is the only gas that has a measureable solubility in aluminum and its alloys [11], gas induced microporosity is caused by the precipitation of hydrogen from the liquid during solidification. Hydrogen can be picked up from water vapor in the surrounding environment by the following reaction:



Since hydrogen is less soluble in the solid phase than in the liquid phase (Figure 3.1), it is rejected into the liquid at the solid/liquid interface during solidification. Consequently, the concentration of hydrogen in the liquid increases with the evolution of the solid fraction. When the concentration exceeds the hydrogen solubility limit in the liquid, the liquid metal becomes supersaturated and hydrogen bubbles can precipitate, resulting in the formation of pores. Depending on the interaction between the growing pore and the developing solid structure, gas-induced pores can form spherical (Figure 3.2 (a) (b)) or complex shapes as they impinge with the developing solid dendrite arms.

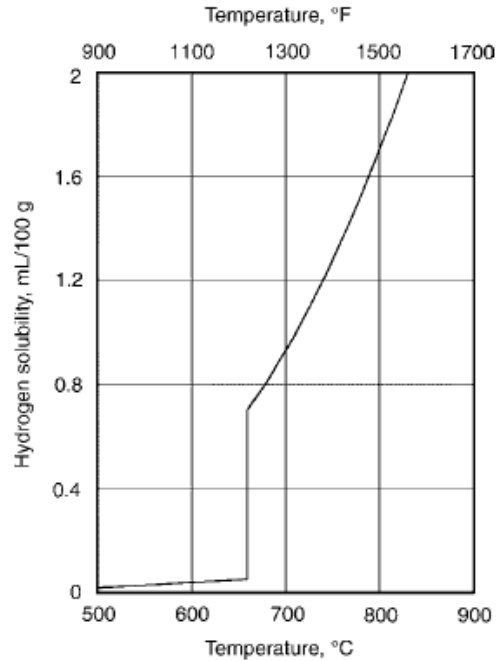


Figure 3.1: Solubility of hydrogen in aluminum at 1 atm pressure [11].

The other type of porosity, shrinkage microporosity, forms as a result of lack of interdendritic feeding during solidification. Like macro-porosity, as discussed in Chapter 1, it occurs due to the volumetric contraction associated with the liquid to solid transformation. As the casting solidifies, metal that is still liquid flows to the region of higher solid fraction to compensate for the liquid/solid volume reduction. The development of the solid microstructure results in increased resistance to fluid flow. Shrinkage microporosity is formed at the point when sufficient resistance develops that liquid flow through the solidifying dendrite network is stopped and the local pressure drops to the pressure of any dissolved gases in solution and/or the vapor pressure of aluminum. Shrinkage microporosity generally has irregular geometry because it forms at high fraction solid (Figure 3.2(c) (d)).

It should be noted that the categories defined above is somewhat misleading as porosity formation in commercial castings is always linked to a combination of hydrogen

solubility and the pressure drop associated with volumetric shrinkage during solidification and may involve both mechanisms - see Figure 3.2 (e), for example.

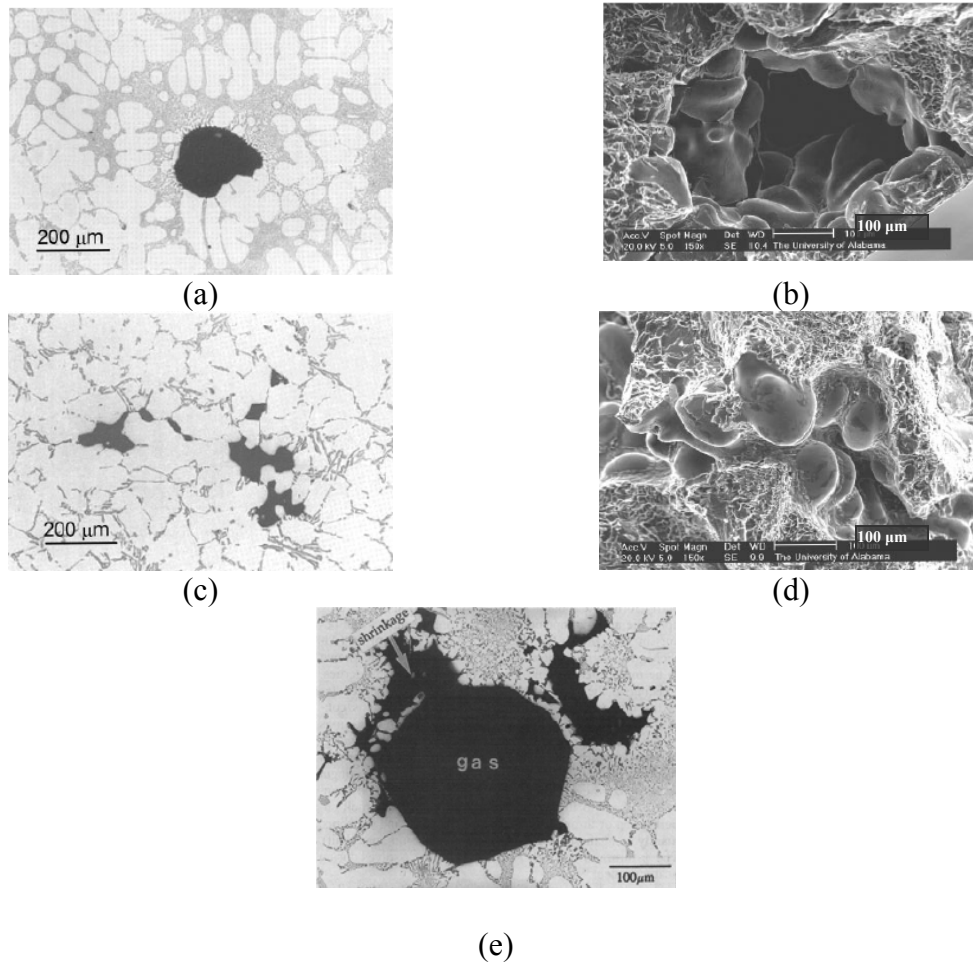


Figure 3.2: (a) Optical micrograph and (b) SEM image of hydrogen induced microporosity in Al-Si alloy ; (c) optical micrograph and (d) SEM image of interdendritic microshrinkage in Al-Si alloy; [42] (e) a shrinkage pore and a gas pore merged together to form a single pore[43].

3.1.2 Effect of microporosity on fatigue performance

Several studies [16-26, 44-49] have shown that microporosity is the key factor in controlling the fatigue properties of aluminum alloys. Components under cyclic loading are often observed to have surface or internal pores as crack initiators. Many researchers have conducted investigations on the mechanisms of fatigue life reduction in cast

aluminum alloys in relation with porosity [16-26, 44-49]. It has been shown that pores in the castings act as stress concentrators that encourage localized damage and lead to crack initiation and propagation. This process can be divided into four stages: 1) the microplasticity induced by the concentrated stress around the pore accumulates and initiates the formation of a fatigue crack. This initiation stage is negligible as it takes only a few cycles if a pore is present; 2) the fatigue crack propagates slowly along the crystallographic planes with high shear stress. This stage is dominant and the growth length in this stage is usually in the scale of several grains; 3) the crack grows wider and the crack tip opens up. The propagation rate increases dramatically in this stage. 4) The crack grows to a critical size that leads to the final failure.

The severity of the effect of casting pores on fatigue is related to a number of factors, such as pore size [16, 21-26, 46-49], morphology [25, 26, 48] and location within the cast part [16, 24, 25, 47]. Among these factors, the effect of pore size has been investigated most extensively. According to Dabaye *et al.* [21] and Zhu *et al.*[23] the pore size distribution can be divided into two populations. The first population is related to small pores (in the order of several to tens of micrometers) where the number of pores is relatively high but the fraction of porosity is low (these pores are observed to be homogeneously distributed in the casting). The second population is of larger pores (in the order of hundreds of micrometers). The number of these pores is lower and they are observed to be spatially less homogeneously distributed. The Paris law can be used to quantify the fatigue life of a specimen given a particular pore size [50]. Based on the Paris law, the propagation rate of a crack is related to the stress intensity factor. The magnitude of this stress intensity factor depends on both the size and location of the crack.

Recently, Murakami [51] proposed a formula that uses a shape factor, stress, and area of the defects (pore or crack) to quantify this stress intensity factor for an opening (Mode I) defect:

$$K_I \cong Y\sigma_0\sqrt{\pi\sqrt{area}}$$

where K_I is the stress intensity factor; σ_0 (N/m) is the stress; $area$ (m²) refers to the area of the defect (pore or crack) on the fracture surface; and Y is a shape factor, which equals 0.65 and 0.5 for surface and internal defects, respectively. Paris law along with the stress intensity factor has been extensively used to predict the fatigue life of materials with a large pore size [44, 48, 49]. However, it has been observed that the Paris law does not apply to cracks with a size smaller than a few grains [52]. This is due to the interactions of small pores with microstructural features [18, 44, 45, 53]. The role of the small pore population on fatigue behavior is still unclear due to the competition with other microstructures such as primary phase and intermetallics. Researchers are advised not to neglect the small pore size population as it may lead overestimation of the fatigue life. It has also been pointed out that the conventional 2-D metallographic analysis of pore size may not be sufficient for fatigue life prediction [23-26, 49], as cracks prefer to initiate from the largest cross section of the pores. Therefore, a 3-D analysis is needed to consider the stereological effects and the irregular shape of the pores.

3.2 Pore nucleation

3.2.1 Microporosity nucleation in aluminum alloy castings

Conventionally, pore nucleation in aluminum alloy castings refers to precipitation of clusters of gas molecules that are thermodynamically stable and can initiate pore growth

[54-56] . Precipitation occurs when either the hydrogen content exceeds the solubility of hydrogen in the melt at the local pressure or the local pressure drops to below the vapor pressure of the liquid metal. Nucleation of microporosity remains a challenge owing to the difficulty in making direct experimental observations. To date information on pore nucleation is obtained indirectly through observations of pore growth in *in-situ* experiments [57-64].

To study the kinetics of pore nucleation and growth, Lee *et al.* observed the solidification process of Al-Cu and Al-Si alloys with an X-ray temperature gradient stage (XTGS) technique [57-59, 63]. In these studies, real time micro-focal radiography was used to monitor the growth of each pore under controlled solidification conditions. The detection limit of the XTGS apparatus was insufficient to resolve the nucleation of porosity; therefore, the nucleation temperature was estimated by extrapolation of the pore size to zero. Figure 3.3 shows the effect of altering the solidification velocity on (a) the nucleation temperature and (b) growth rates of the pores in an Al7Si alloy [57]. The dashed lines in Figure 3.3(b) show the experimental radiographic traces of several pores for three different solidification velocities. According to the observations, the pores nucleated continuously over a range of temperature throughout the solidification process. This work lead to the introduction of a Gaussian function of the following form as a means of describing the nucleation kinetics [58]:

$$\frac{dn_p}{dT} = \frac{n_{max}}{T_\sigma \sqrt{2\pi}} \exp\left(-\frac{(T - T_N)^2}{2T_\sigma^2}\right) \quad \text{Equation 3.1}$$

where n_{max} (mm^{-3}) is the maximum number of nuclei, T_σ ($^\circ\text{C}$) and T_N ($^\circ\text{C}$) are the deviation and the mean of the Gaussian temperature distribution function. These parameters were argued to be a function of cooling rate and determined by fitting with

experimental results. In another work [63], Lee and Hunt modeled the stochastic nature of pore nucleation by converting the nucleation temperature in the Gaussian function to hydrogen supersaturation, which was defined as the ratio of local hydrogen concentration to the solubility of hydrogen in the liquid: $\frac{C_l}{S_H} = SS_n$, where C_l (mol/m³) is the hydrogen concentration in the bulk liquid, S_H (mol/m³) is the hydrogen solubility limit and SS_n is the hydrogen supersaturation. The hydrogen supersaturation at the point of nucleation was calculated from the nucleation temperature and solid fraction based on the lever rule. It was found that micropores nucleate when the hydrogen supersaturation reached a level around 2.0 with a standard deviation of 0.5.

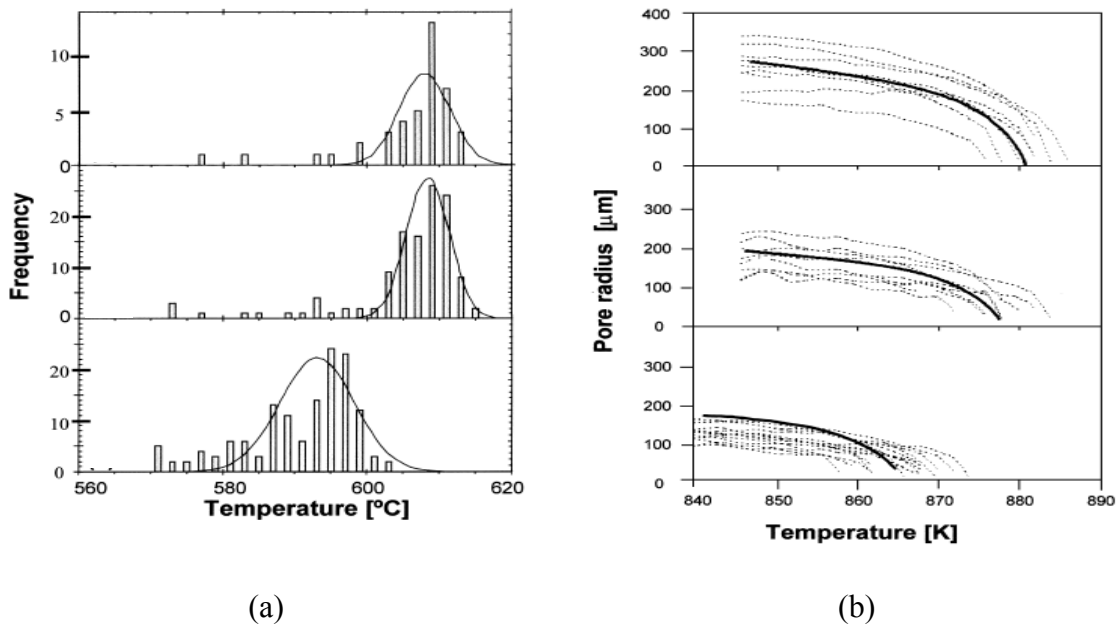


Figure 3.3: Effect of altering the solidification velocity (low, medium and high from top to bottom in the graphs) on (a) nucleation temperature and (b) growth rates of the pores in Al-7wt%Si alloy [57].

More recently, Arnberg and Mathiesen conducted another *in-situ* study of directional solidification of aluminum copper alloy by X-ray tomography using synchrotron radiation in combination with a low-noise fast-readout camera, which provided spatial resolutions down to 1.5 μm and temporal resolutions down to 0.15 s [61]. This high resolution allowed clear and more simultaneous observation of porosity initiation. Based on the observations in this work, Felberbaum pointed out that microporosity was observed to initiate from a tiny groove [64]. As illustrated in [64], Figure 3.4 is a time sequence showing formation of one single pore during solidification of the Al-30wt%Cu alloy. Solidification in this sample is parallel with gravity and the columnar dendrites grow downward in these images. Figure 3.4 (a) shows that the pore bubble originated by a meniscus groove filled with gas. The bubble then floats to the root of a dendrite and expands due to pressure drop that occurs in the mushy zone. The trace of the floating bubble is shown in Figure 3.4 (b). In Figure 3.4 (c), the pore is stabilized between the dendrite arms and continued to grow as shown in Figure 3.4 (d).

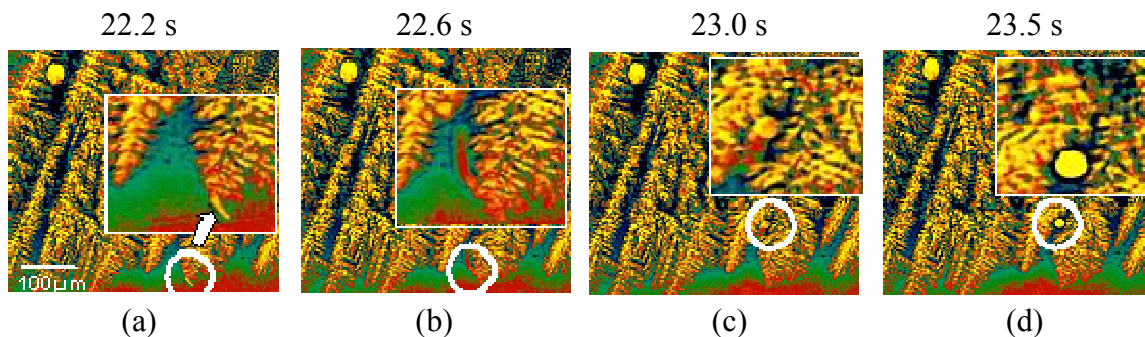


Figure 3.4: Sequence of X-ray radiographs showing the formation of gas porosity in a directionally solidified Al-30wt%Cu alloy [61].

3.2.2 Homogenous and heterogeneous nucleation theories

In classical nucleation theories, the driving force for nucleation is the thermal fluctuation that provides the energy required to overcome the nucleation energy barrier in the system. During the nucleation of a solid within a liquid phase, the change of system energy associated with nucleation includes a decrease of bulk free energy and an increase in energy related to the formation of a liquid/solid interface [65].

Similarly, the work required for homogeneous nucleation of a pore in the liquid can be expressed as [14, 56]:

$$\Delta G = -\frac{4}{3}\pi r^3 \Delta p + 4\pi r^2 \gamma \quad \text{Equation 3.2}$$

where Δp (N/m²) is the pressure change when the void is formed in the liquid, r (m) is the radius of the void, and γ (N/m) is the surface tension of the interface between the gas and liquid phases. Plotting the change of the system energy as a function of radius (Figure 3.5), it is shown that growth of the pore induces a decrease of free energy when the pore radius exceeds

$$r_c = 2\gamma / \Delta p. \quad \text{Equation 3.3}$$

Therefore, the corresponding $\Delta G_{max} = 16\pi\gamma^3/3\Delta p^2$ is the energy barrier needed to be overcome for the pore nucleation.

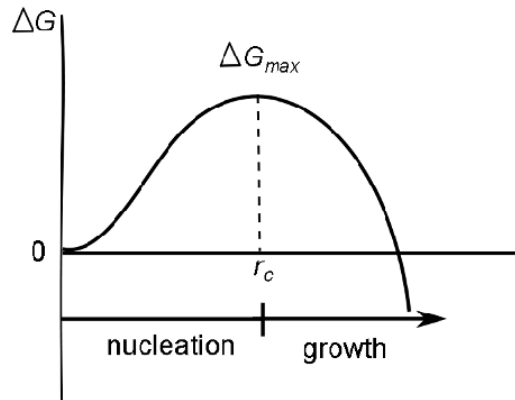


Figure 3.5: Variation of the system free energy with radius of the potential pore.

It has been pointed out by Fisher [14, 56] that vapor bubbles formed spontaneously from the energy fluctuations will not be stable until the pressure in the bubbles exceeds the equilibrium pressure of the reaction gas (based on the reaction equation). Applying the rate theory in thermodynamics, the rate of formation of bubbles was derived as a function of the fracture pressure of liquid. It was calculated that the critical pressure difference required (Δp) for homogeneous bubble nucleation in liquid aluminum can be as high as 31,000 atm. Campbell later estimated this pressure by assuming r_c in Equation 3.3 as the atomic radius. It was found that the Laplace-Young pressure difference in and outside the bubble is 30,000 atm [14]. Therefore, homogeneous nucleation of pores in liquid metals under a normal atmospheric pressure is extremely difficult.

The conventional heterogeneous nucleation theory for pore formation suggests that solid oxide inclusions in the melt provide nucleation sites, which reduce the energy barrier required for pore nucleation [33, 54, 66]. In this case, γ in Equation 3.2 and Equation 3.3 is the difference in surface tension between the liquid/substrate interface and the gas/substrate interface. The shape of a nucleated bubble on the substrate is related

to the contact angle, θ , which depends on the balance of surface tension forces at the junction where the solid, liquid and gas phases meet. Figure 3.6 (a) to (c) show the configurations of a gas pore nucleated on the surface of a solid substrate.

Fisher calculated the pressure difference for heterogeneous nucleation [56] and found that nucleation is easier by a factor of

$$S(\theta) = \Delta p_{heter} / \Delta p_{homo} = 1.12 \left\{ (2 - \cos \theta)(1 + \cos \theta)^2 / 4 \right\}^{1/2} \quad \text{Equation 3.4}$$

Also the energy barrier for nucleation reduces to

$$\Delta G_{max} \cdot (2 - \cos \theta)(1 + \cos \theta)^2 / 4 \quad \text{Equation 3.5}$$

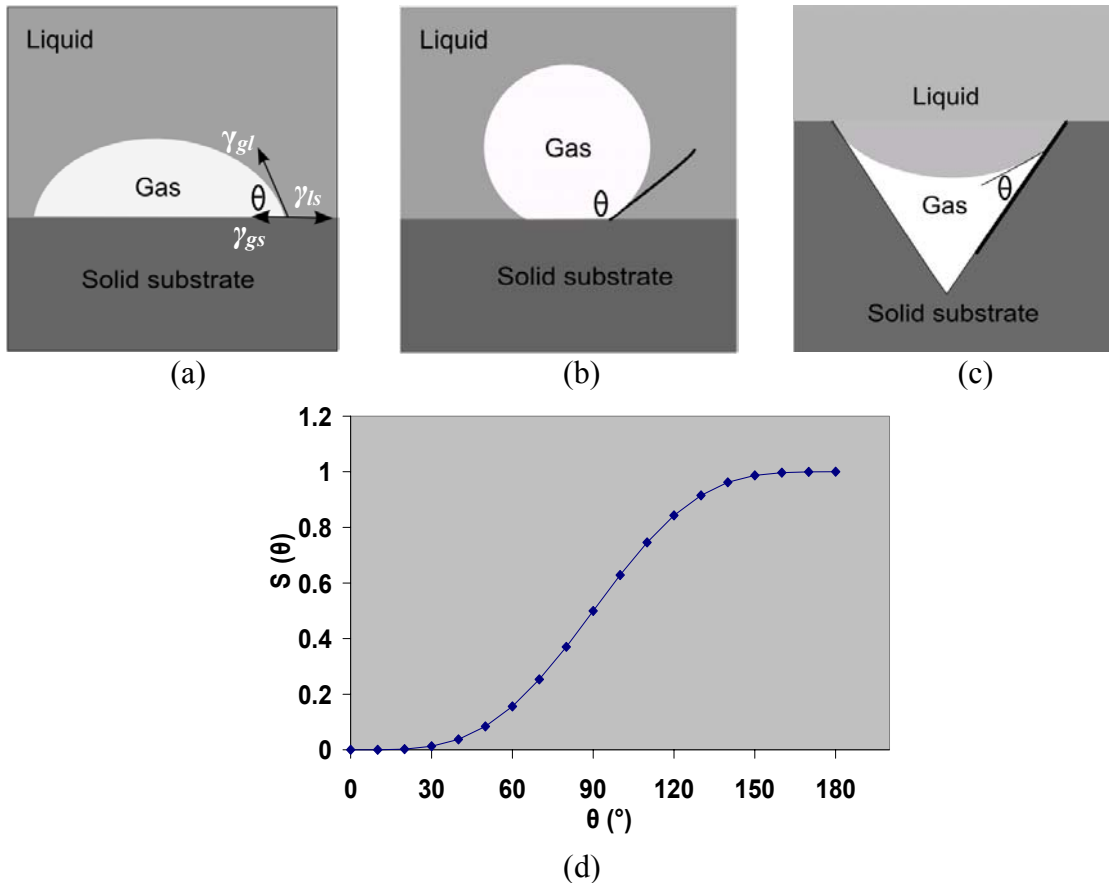


Figure 3.6: Schematic of (a)-(c) heterogeneous nucleation of a gas pore on a solid substrate; (d) $S(\theta) = (2 - \cos \theta)(1 + \cos \theta)^2 / 4$ as a function of contact angle.

Figure 3.6 (d) plots $S(\theta)$, which characterizes the ease of heterogeneous nucleation when the contact angle θ varies from 0° to 180° . It is shown that nucleation requires lower nucleation energy and smaller pressure difference at smaller θ . θ equal to 180° corresponds to the case of homogeneous nucleation. Also, with a small θ , as illustrated in Figure 3.6 (a), the radius of curvature of the cavity is much larger than the radius of a sphere (Figure 3.6 (b)) that contains the same volume. Therefore the pressure difference that should be overcome can be reduced based on Equation 3.3. With a small contact angle, the radius of curvature associated with a hemispherical cap on a solid substrate can be in the order of micrometers. In this case, the pressure difference estimated from Equation 3.3 is 10 to 100 atm, indicating heterogeneous nucleation is more realistic and dominant due to the presence of heterogeneous nucleation sites.

3.2.3 Bi-film entrainment theory

More recently, Campbell pointed out heterogeneous nucleation still seems highly improbable due to the restriction on the minimum contact angle attainable between the liquid/pore interface and the solid substrate, which is observed as close to 20° in practice [14]. Applying Equation 3.4, with a contact angle 20° the pressure difference required for heterogeneous nucleation is still high (5% of Δp_{homo}). He proposed a nucleation-free mechanism for porosity formation [38-40] based on a continuous solid oxide film present on the surface of liquid aluminum. Due to the free-surface turbulence during the pouring and casting process, these oxide films often become entrained and folded into the melt. The dry sides of folded oxide films cannot form bonds and are usually referred to as 'bi-films'. These bi-films form gas cavities by entrapping air within the folded films. These gas cavities can be considered as preexisting pores in the melt. Pore growth can occur by

the unfurling of the bi-films followed by hydrogen diffusion or a pressure drop due to insufficient liquid feeding. In this theory, there is actually no nucleation process involved. The bi-films are the initiator and the hydrogen or the reduced pressure is the contributor to the porosity formation process. The existence of bi-films was revealed by the reduced pressure test (RPT) in Fox and Dispinar's work [39, 40, 67]. It was observed that the bi-films can unfurl and expand into 'streak-like' cavities under reduced pressure as shown in Figure 3.7.

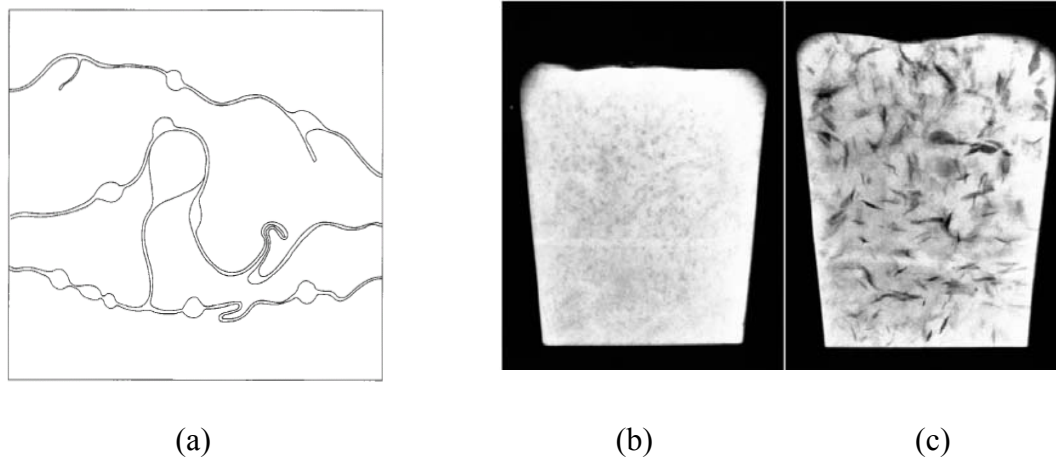


Figure 3.7: (a) Schematic illustration of bi-films with their trapped air bubbles. (b) (c) Comparison of x-ray radiographs taken at same time after pouring from same melt of Al-7Si-0.4Mg alloy subjected to solidification under pressure (b) 1 atmosphere, showing diffuse images of furled bi-films; and (c) 0.01 atmosphere showing unfurled bi-films [67].

Another experiment which supports this theory was conducted by monitoring the volume of an air bubble at a constant temperature in a liquid aluminum melt using real-time X-ray microradiography [68]. It was observed that at hydrogen contents below 0.3 cc/100g-Al the volume of the air bubble was reduced, as oxygen contained in the bubble reacted with the liquid aluminum. When the hydrogen content was increased to 0.3 cc/100g-Al, the bubble expanded as hydrogen in the melt passed into the bubble.

Therefore, air bubbles introduced into an aluminum melt could expand as the result of diffusion of hydrogen into their interior atmosphere when sufficient hydrogen supersaturation is achieved. It was concluded that the bi-films in aluminum alloy castings would behave similarly and thus suggest they would act as initiation sites for hydrogen gas porosity in castings during solidification.

Zhao [69] and Felberbaum [64] performed similar vertical 1D solidification experiments with Al-Cu alloys. The ingots were melted directly in a heated crucible that was water cooled with a copper chill. No liquid metal pouring processes were involved in these experiments, but near spherical gas pores that suggest early nucleation were still found. The authors concluded that the bi-film theory may not be universal. It is important only when the liquid feeding and/or the filtration systems are not properly designed.

It should be noted that there is no conventional nucleation process in this bi-film theory. Nevertheless, the term nucleation is used throughout the thesis when referring to the dependence of pore initiation on oxide films. Here nucleation is generally used as ‘pore initiation’ instead of the conventional ‘atomic precipitation’ process, to include the to-be-proved bi-film mechanism proposed by Campbell.

3.3 Pore growth

As discussed in 3.1, the formation of microporosity in an aluminum casting is generally caused by a combination of a drop in the local pressure due to restricted flow at high fraction solids and an increase in the concentration of hydrogen in the liquid due to a reduction in solubility of hydrogen in the solid, which lead to the conditions of

“nucleation” being achieved. Beyond this point evolution in the size of the pore is dominated by pore growth kinetics.

3.3.1 Equilibrium conditions

The equilibrium conditions at the pore liquid interface require explanation to better illustrate the pore growth mechanisms. Considering a spherical pore in the bulk of a liquid as shown in Figure 3.8, two conditions must be met to maintain its equilibrium. The first one is the mechanical equilibrium, which requires that the internal pressure force within the pore should be balanced with all the other forces applied on it, i.e.,

$$p_g = p_{local} + \frac{2\gamma}{r} \quad \text{Equation 3.6}$$

in which p_{local} (Pa) is the local pressure of the liquid, γ (N/m) is the surface tension of the pore liquid interface, r (m) is the pore radius. The second condition is that the hydrogen activities within the pore and in the liquid at the interface are in equilibrium. At the pore liquid interface, the reaction $[H] \Leftrightarrow \frac{1}{2}H_2$ takes place. When in equilibrium, the relationship between the hydrogen concentration at the liquid/pore interface and the gas pressure in the pore may be expressed as follows [66, 70]:

$$C_{lp} = K_L \sqrt{p_g} \quad \text{Equation 3.7}$$

where C_{lp} (mol/m³) is the hydrogen concentration at the liquid/pore interface and K_L (mol/m³/atm^{1/2}) is the equilibrium constant. Combining Equation 3.6 and Equation 3.7, the relationship of C_{lp} as a function of pore radius can be established as

$$C_{lp} = \sqrt{p_{local} + \frac{2\gamma}{r}} \quad \text{Equation 3.8}$$

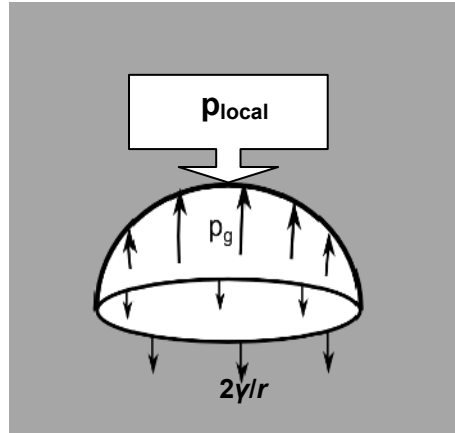


Figure 3.8: Schematic of all pressures applied on an isolated pore in equilibrium in the bulk liquid.

3.3.2 Pressure-drop controlled growth

To get an understanding of the pore growth controlled by pressure drop, the term “mushy zone” should firstly be explained. The mushy zone is a region of mixed solid and liquid phases formed during the solidification of an alloy. Under equilibrium solidification conditions this region is bounded by the liquidus at the upper end in temperature and by the solidus at the lower end [71]. In this region, the fraction solid varies between 0 at the liquidus and 1 at the solidus. The permeability also decreases with increasing fraction solid and in the limit can reach zero at the fraction solid close to one. The effect of the local pressure drop on porosity formation proposed in one study is shown in Figure 3.9 with a schematic view of the columnar mushy zone of a directionally solidified ingot [72]. Solidification proceeds from left to right in Figure 3.9 (a) and liquid is drawn into the developing structure in the opposite direction also shown in the Figure 3.9 (a). Figure 3.9 (b) illustrates the local pressure drop associated with liquid feeding in the mushy zone. This pressure drop leads to the decrease of internal pressure in the pore as shown in Equation 3.6. The reduced internal pressure drives the pore to grow as

indicated by the ideal gas law. Combined with a reduction in temperature this pressure drop also leads to a decrease in the solubility limit of dissolved gases in the liquid phase (Figure 3.9(c)) and a lower equilibrium hydrogen concentration at the pore/liquid interface as indicated in Equation 3.8. This effect further promotes pore formation related to hydrogen transport as explained in the next section.

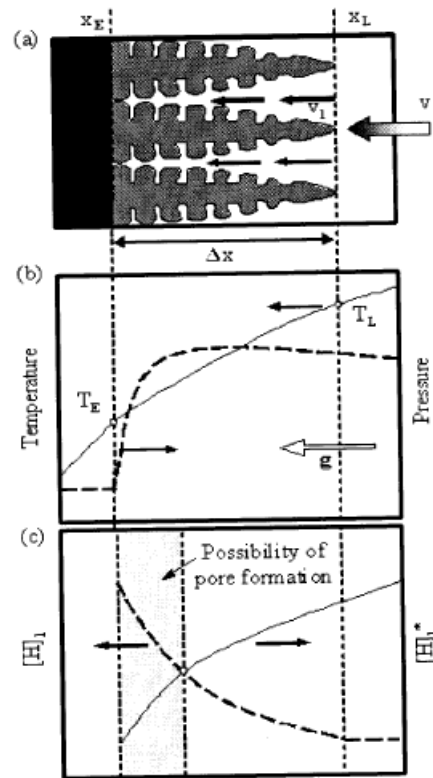


Figure 3.9: Schematic representation of: (a) a 1D columnar mushy zone; (b) temperature and pressure profiles (gravity g is towards left); (c) effective gas concentration $[H]_l$ and gas solubility limit $[H]_*$ in the liquid [72].

3.3.3 Diffusion controlled growth

Diffusion controlled pore growth happens when the hydrogen concentration exceeds C_{lp} in Equation 3.8. In the hydrogen supersaturated melt, the dissolved atomic hydrogen should diffuse from the melt to the pores due to the low hydrogen potential of the pores.

The driving force for this diffusion is the concentration gradient around the pore, as shown in Figure 3.10.

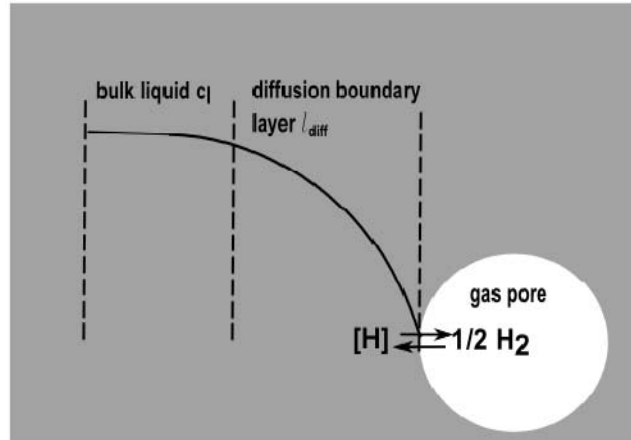


Figure 3.10: Schematic showing the hydrogen concentration profile at a hydrogen diffusion boundary layer around a growing pore.

Based on analytical solutions to the diffusion equations [63, 73], the criterion to determine whether or not a stable concentration gradient can be established and drive pore growth is $l_p \geq \lambda \sqrt{D_H \Delta t}$, where l_p (m) is the average distance between the pores, λ is a coefficient obtained by solving the diffusion equations, D_H (m^2/s) is the hydrogen diffusion coefficient in the liquid phase and Δt (s) is the solidification time. Therefore, diffusion is more likely to be a limiting factor for pore growth in a case where the density of pores is low (large l_p) and the solidification time is short (small Δt).

3.3.4 The role of impingement on pore growth

The impingement between the pore and solid phase starts when the pore grows to a size that sits in contact with the solid grains. When pore/solid impingement occurs the effective diffusion surface area between the pore and the liquid phase is reduced. This phenomenon has an important impact on pore growth. The effect is highly dependent on

the development of the solid microstructure. It has been shown that the effect of grain radius on pore evolution can be significant [57], e.g., for the smaller grain in an Al-7wt%Si alloy with TiB₂ grain refiner added, the pore growth stops at an earlier stage due to impingement with the solid grains during solidification. When the grain radius is larger, the effect of solute layer impingement from adjacent pores is the dominant influence in slowing down the pore growth rate. As a result, the pores do not impinge upon the grains.

Most empirically-based microstructure evolution models adopt some form of impingement factor to account for the attenuation in growth that occurs at high fractions of the developing phase. The most well-known of these is the one proposed by Kolmogorov [74], Johnson-Mehl [75] and Avrami [76] that when applied to solidification has the form $q = 1 - f_s$, where q is the impingement factor and f_s is the solid fraction. In the other work, Speich and Fisher [77] used an empirical relationship $q = k_a f_s (1 - f_s)$, where k_a is a fitting parameter determined by experimental data. Similar to these solidification models, an impingement factor can also be used to determine the pore-liquid interfacial area. It accounts for the fact that the fraction of the pore liquid interfacial area decreases as the pore liquid interface is covered by solid phase due to the development of the solid structure. In Carlson *et al.*'s work [78], the form used for the impingement factor is $q = (1 - f_s)^m$, where m is a fitting parameter determined with the empirical data.

3.4 Factors affecting microporosity formation

3.4.1 Initial hydrogen concentration

The effect of hydrogen content on pore formation has been well established [57, 60, 79-86]. It has been reported that high initial hydrogen content increases the final porosity

fraction, since the melt becomes supersaturated earlier. The pores start to form in the early stage of solidification and grow to larger sizes [57, 85, 86]. Also increased hydrogen content results in a higher concentration gradient around the pores (Figure 3.10) so that the diffusion controlled pore growth is enhanced.

Degassing of aluminum alloy melts is therefore necessary to reduce gas porosity in the castings. Two degassing techniques are widely used in the foundry industry: 1) flux degassing; and 2) rotary degassing. The basic principle of these two degassing techniques is illustrated in Figure 3.11[87]. Fine gas bubbles are introduced into the molten aluminum by either the reaction of fluxes with the melt (Figure 3.11 (a)) or passing a chemically inert gas through the melt using a rotating impeller (Figure 3.11 (b)). Hydrogen diffuses into these gas bubbles because the partial pressure of hydrogen in the bubble is lower than the surrounding melt. Therefore, these small bubbles are able to absorb hydrogen and then release it into the atmosphere when they reach the surface of the melt due to their buoyancy. Besides removing undesirable hydrogen, degassing is also capable of removing some solid inclusions such as oxide films, which are within the melt providing a quiescent melt surface is maintained [88-90]. These inclusion particles tend to be attached to the bubbles due to surface tension effects. Along with the bubbles they are then floated to the surface of the melt where they can be removed as dross.

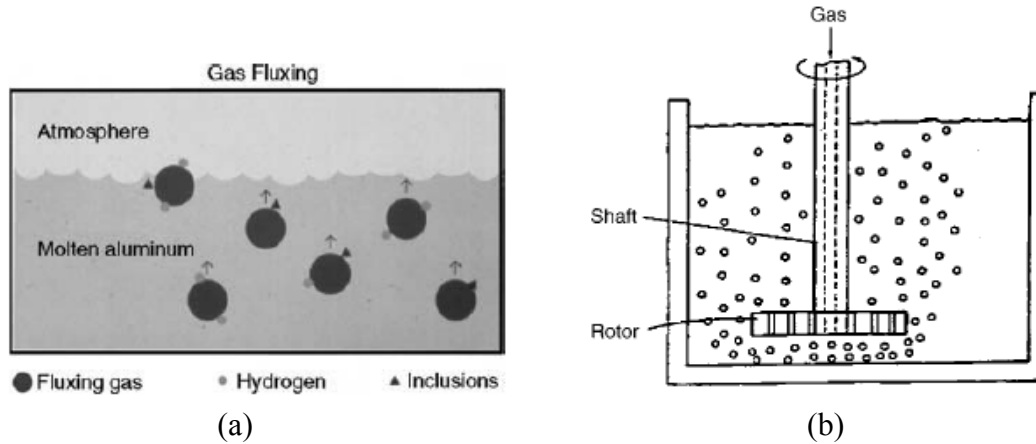


Figure 3.11: Schematic of (a) gas fluxing and (b) rotary degassing in molten aluminum [87].

Determination of hydrogen content in the casting melt is critical in industrial and scientific applications. Measurement of dissolved hydrogen in molten aluminum can be classified into three broad categories: the semi-quantitative methods (e.g., Volcestar), quantitative laboratory methods (e.g., hot extraction and LECO) and Closed Loop Recirculation methods (e.g., ALSCAN and Telegas). Details about these techniques have been well described in Reference [91].

3.4.2 Cooling conditions

The cooling rate can have multiple effects on microporosity formation. For hydrogen-induced porosity, increasing the cooling rate reduces porosity formation. This is because a higher cooling rate results in smaller dendrite arm spacings and a finer solid microstructure, which will increase pore/solid impingement and thus reduce the effective diffusion interface area [57, 60, 78, 91]. An increase in the cooling rate also reduces the time over which the diffusion of hydrogen into the pores can occur resulting in a further reduction in pore size [34, 37, 79, 83, 92]. In addition, there is often a higher temperature gradient associated with increased cooling rates which results in a short mushy zone. As a result, liquid feeding is easier and shrinkage porosity is reduced. However, one possible

opposing tendency is that, this effect may be overcome by the reduced permeability due to the finer solid microstructure and hence a larger relative pressure drop at high solid fractions [93-95].

3.4.3 Inclusion content

The cleanliness of the melt is of great importance in achieving high quality castings. For aluminum alloy castings, the most common and detrimental inclusions have been shown to be oxide films. In addition to acting as a defect in their own right, oxide films also promote microporosity formation by facilitating pore initiation [14, 32-40, 96]. This has been discussed in Section 2.2. The techniques to remove inclusions from the molten aluminum include fluxing treatment, filtration and electromagnetic separation [97]. The cleanliness of molten aluminum alloys can be assessed with various methods, as summarized in Table 3.1 [98].

Table 3.1: Summary of quantitative impurity analysis techniques[98].

Method	Sample weight	Sample area (m ²)	Type of impurities
Chemical analysis			
Emission spectroscopy	10-3 g	-	Li, B, Na and heavier elements
Hot extraction	5 g	-	Hydrogen
Combustion analysis	2 g	-	Carbon
Neutron Activation	17 g	-	Oxygen
Gas chromatography	0.5 g	-	Al ₄ C ₃ and CaC ₂
Volumetric analysis			
Centrifuging of melt	100 g	0.001	Carbides, borides and oxides
Filtration Techniques	500 - 2000 g	0.01 - 0.05	Inclusions > 30 μm
Non-destructive techniques			
Ultrasonic Techniques	2 - 20 kg/min	-	Inclusions > 100 μm
Methods based on Coulter's principle	10 - 100 g	-	Inclusions > 1 μm

3.4.4 Alloy composition

The alloy composition may affect microporosity formation in different ways. For example, the eutectic temperature and the shrinkage characteristics of the alloy may be altered [99-101]. The porosity level may decrease with higher eutectic fractions if the channels between the primary dendrites become more open and feeding becomes easier when the eutectic fraction is increased [102-105]. In addition to altering the feeding characteristics of the alloy, the alloying elements may affect the hydrogen solubility in aluminum [106-110]. The initial hydrogen content of the melt and the hydrogen saturation limit may vary with alloy compositions. Likewise different aluminum alloys have different affinities to oxygen [35, 105, 109-117], thus the amount of oxide inclusions introduced into the melt may be affected. As a result, the nucleation of pores can be promoted or delayed. Also, the addition of some alloying elements (e.g., Sr and Na) changes the surface tension between the pore and molten metal [118, 119]. This affects the nucleation process by changing the nucleation energy barrier (Equation 3.2) and the critical pressure difference (Equation 3.3). Also the pore growth is affected due to the curvature effect according to Equation 3.6 and Equation 3.8. Finally, grain refiners added to alloys reduce the grain size. This has an impact on the pore/solid impingement, which affects the growth of gas-induced pores. It also alters the distribution of pockets of isolated liquid that affects shrinkage pores. It has been reported that grain refiners reduces the volume fraction of pores and leads to a greater number of small discrete pores than an unmodified alloy [43, 46, 83, 89, 120-123].

3.4.5 Ambient pressure

The ambient pressure P_a (Pa) affects porosity formation by changing the internal pressure in the pores (Equation 3.6) and the hydrogen potential at the pore/liquid interface (Equation 3.8). Decreasing this ambient pressure increases porosity formation and vice versa. One application using this principle is the reduce pressure test (RPT), which is used to evaluate the hydrogen content in molten aluminum alloys [91]. In a RPT, the ambient pressure is reduced to exaggerate porosity formation. These oversized pores make the casting samples porous and thus significantly change their density. Since the level of porosity fraction is associated with the initial hydrogen content in the melt, measurement of the density of the porous sample gives a qualitative indication of the hydrogen contents in the casting melt.

3.5 Microporosity analysis

Evaluation of microporosity can be qualitative or quantitative depending on the desired accuracy in the application. In foundry applications, evaluation of microporosity is usually qualitative or semi-quantitative. Examples are ultrasonic and eddy current inspections [124]. In academic research, accurate quantification and characterization of pores are usually necessary in order to investigate the physical mechanisms of microporosity formation in castings.

3.5.1 Optical microscopic analysis

Conventionally, porosity analysis is performed using an optical microscope. Samples are usually sectioned and prepared for metallographic examination using the standard grinding and polishing procedures [125]. After the metallographic examination on the

cross section of the sample is performed, image analysis is undertaken to quantify the porosity and/or characterize the pore morphology. The advantage of optical microscopic analysis is its low cost, although preparing samples can be time consuming. The limitation of optical microscopic analysis is that it only gives 2-D information such as area fraction of porosity and surface morphology. This is not sufficient when the 3-D morphology, the volume fraction and the size distribution of the pores are required [26, 92]. As shown in Figure 3.12, a pore with complex morphology is poorly represented with 2-D analysis on a sectioned area. A group of discrete pores viewed on a sectioned area examined by metallographic analysis may truly represent one single tortuous shrinkage pore [126].

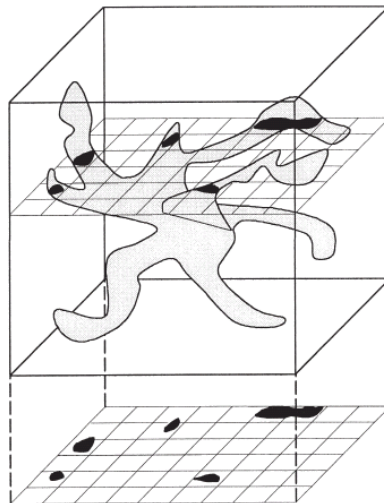


Figure 3.12: Schematic image of a shrinkage pore and the resulting two-dimensional image when sectioned [126].

3.5.2 X-ray microtomography (XMT) analysis

Using XMT analysis pores can be characterised in 3-D. The basic principle is that an X-ray beam propagates through a sample and the transmitted beam is recorded on a

detector. The sample is usually rotated in order to produce a series of 2-D radiographs. A filtered back-projection algorithm [127] is then often applied to reconstruct the 3-D image of the sample from these radiographs. During XMT scanning, two types of contrasts are produced depending on whether the absorption mode or the phase contrast mode, is used. In the absorption mode, the contrast is given by the atomic numbers of the elements and the density. The transmissivity can be calculated with Beer-Lambert law [128]. In the phase contrast mode, the sample is farther from the detector in comparison to when using absorption mode. The contrast is due to different phase retardation of the beam after propagation through different sides of an interface [129]. This contrast is efficient for edge detection especially when absorption mode produces a weak contrast. For example, separation of primary and eutectic structure of Al-Si alloys is difficult in the absorption contrast mode due to the close atomic number between aluminum and silicon. The phase contrast mode thus provides an alternative approach for microstructure characterization. The reader is referred to [130] for more details about XMT analysis technique.

Microporosity analysis with the XMT technique overcomes the limitations of 2-D metallographic techniques by characterizing 3-D morphology of the pores. Chaijaruwanich *et al.* examined the evolution of porosity during hot rolling [131] and homogenization [132] processes in a direct chill cast Al-Mg alloy using both 2-D metallography and 3-D XMT analysis. It was found that metallographic analysis lead to the incorrect hypothesis that classic inter-pore coarsening occurred because the observations showed that the maximum pore size and percentage porosity increased and number density decreased during rolling. XMT observations disproved this hypothesis

and showed that there is no change in these quantities only a change of pore morphology. The fact is that intra-pore Ostwald ripening occurred resulting in the originally tortuous pores spheroidising.

Besides giving accurate 3-D information of the actual pores, XMT provides details of the solid microstructure and thus captures the constitutive features of pores along with other phases formed during solidification. Felberbaum [64] analyzed pores in Al-Cu alloy samples using high resolution X-ray tomography to validate and improve an impingement model that approximated the curvature restriction of the pores due to growing solid network [133]. It was shown that the impingement model must be a function of the volume fraction of the primary phase and the secondary dendrite arm spacing. In another work, based on the XMT observations of the interface between porosity and solid phase, Atwood and Lee *et al.* [60, 86] developed a combined cellular automata (CA) and finite-difference (FD) model to predict the full dendritic structure of the primary phase and the complex three-dimensional shapes of the pores.

Furthermore, X-ray micro-tomography has been used to perform in-situ observations of pore formation events. With digital video sequences of the XMT images the increase in size of each pore as a function of time or temperature can be tracked and analyzed [57-59, 63]. It also has been used to observe the formation of porosity by internal damage during semi-solid deformation and to study the mechanisms of hot tear formation in aluminum alloys [134-136].

3.5.3 Scanning electron microscopic (SEM) analysis

A scanning electron microscope with an embedded energy dispersive X-ray analyzer (EDX or EDS) has been used to capture very localized features of pores in order to study

the origin of their formation. Kakas [137] examined the inner surface of pores with SEM/EDX analysis to study porosity formation in the thinnest section of an Al-Si-Cu alloy piston. Based on the higher concentration of solutes Cu, Mg, Ni and Fe that suggests the location of solidification of last solute-rich liquid, it was concluded that the pores were formed due to insufficient feeding during the last stages of solidification. In Liu's work [138], SEM/EDX analyses were used to study how strontium oxides were responsible for the porosity formation observed in Sr-modified Al-Si alloys. SEM micrographs showed pores were frequently associated with strontium oxides that appeared as white AlSrO particles inside a pore. The morphology of the pores was determined by the dispersed particle or thick film form of the oxides. Although restrictions exist due to the limitations on surface analysis and limit of spatial resolution of this technique, there is no doubt that SEM/EDX analysis has provided valuable insights into the structure and nature of porosity in aluminum alloys.

3.6 Modelling of microporosity formation

The modeling of microporosity can be categorized into four model types: criterion function models, interdendritic flow-shrinkage models, hydrogen diffusion models, and cellular automata models.

3.6.1 Criterion functions

Criterion functions predict microporosity formation with empirical equations based on local solidification conditions such as cooling rate, solidus velocity and thermal gradients. The most well-known function that has been developed is the Niyama function[139]. It predicts difficult-to-feed regions where shrinkage pores are most likely

to form. It is determined by the ratio of the thermal gradient, $G(^{\circ}\text{C}/\text{m})$, to the cooling rate, $R(^{\circ}\text{C}/\text{s})$, i.e., $\frac{G}{\sqrt{R}} > \text{constant}$, where the constant is dependent on the casting alloy. The Niyama criterion has been applied to many different aluminum alloys. It has been reported that most shrinkage porosity can be enclosed by a contour of $\frac{G}{\sqrt{R}} = 1$ $^{\circ}\text{C}^{1/2}\text{min}^{1/2}/\text{cm}$ [140]. Besides Niyama functions, many other criteria functions have also been proposed [141-148]. However, criterion functions ignore the effect of gas diffusion, thus have the limitations of only predicting the shrinkage porosity. Most criteria can only be applied to castings with difficult-to-feed regions and castings with low hydrogen content.

3.6.2 Interdendritic flow shrinkage models

Since the 1960s, many researchers have focused on shrinkage driven pore growth, developing models that range from exact mathematical solutions to approximate asymptotic analytical solutions [41]. The initial work centered on defining solutions for the governing equations of the fluid flow through the mushy zone. These models were based on assumptions including a constant thermal gradient or a constant solidification velocity. These assumptions resulted in an unrealistic constant liquid feeding velocity, which prevents application of the models to complex geometry encountered in many industrial castings. In 1985, Kubo and Pehlke [149] first developed a model which solved liquid feeding in the mushy zone by Darcy's Law, which is a general equation governing the fluid flow through a porous media. The expression used in their work is:

$$\begin{aligned} u &= -\frac{K}{\mu f_l} \frac{\partial p}{\partial x} \\ v &= -\frac{K}{\mu f_l} \frac{\partial p}{\partial y} - \frac{K \rho g}{\mu f_l} \end{aligned} \quad \text{Equation 3.9}$$

where u (m/s) and v (m/s) are velocity in x and y direction (y is in the direction of gravity), p (Pa) is the metal pressure, f_l is the liquid fraction, K (m²) is the permeability of the porous medium, μ (Pa·s) is the dynamic viscosity, ρ (kg/m³) is the density of the melt, and g (m²/s) is the gravitational acceleration.

Once the evolution of solid fraction is known, Darcy's equation (Equation 3.9) is substituted into the continuity equation based on the mass balance of the volume element:

$$\left(\frac{\rho_s}{\rho_l} - 1 \right) \frac{\partial f_l}{\partial t} - \frac{\partial f_l u}{\partial x} - \frac{\partial f_l v}{\partial y} + \frac{\partial f_p}{\partial t} = 0 \quad \text{Equation 3.10}$$

where f_p is the fraction of porosity. Therefore, the fraction porosity can be related with pressure drop due to Darcy flow, by combining Equation 3.9 and Equation 3.10. If no pores were formed the pressure field was solved and then assessed to define whether sufficient supersaturation had occurred for pore nucleation according to the instant nucleation criteria [55]. After pores were formed, the gas pressure inside the pore p_g was obtained by the mechanical equilibrium condition for the pores. Once the gas pressure in the pore is known, the ideal gas law and conservation equation for gas content can be applied to calculate the volume porosity as follows:

$$[H_0] = (1 - f_l)[H_s] + f_l[H_l] + \alpha_H \frac{p_g f_p}{T} \quad \text{Equation 3.11}$$

where $[H_0]$ (mol/m³) is the initial hydrogen concentration, $[H_s]$ (mol/m³) and $[H_l]$ (mol/m³) are hydrogen concentration in the solid and liquid phases, and α_H (J/mol/K) is the gas constant. Models of porosity growth based on Darcy's law have been developed and incorporated in many commercial finite element codes [72, 150-152]. The pressure driven growth of pores has been extensively studied since the 1980s. They are generally

considered more applicable than the criterion functions. However, the interdendritic flow models have shown weaknesses in being unable to predict the stochastic feature of pore size during solidification [57]. This is due to the pores being assumed to be spherical with a uniform radius in the interdendritic flow models. Only the porosity fraction and average pore radius can be obtained by solving Equation 3.11.

3.6.3 Diffusion controlled pore growth models

A diffusion controlled pore growth model was not developed until the late 1990s. Lee *et al.* [63] first concluded that for small mushy zones (e.g. < 20 mm for aluminum-copper alloys), porosity growth is dominated by hydrogen diffusion. They calculated the maximum pressure drop based on the Darcy equation to determine the significance of pressure drop due to Darcy flow on the pore growth. The result showed that the largest pressure drop was less than 0.8% of the atmosphere pressure, too small to have a significant effect upon the pore radius. Furthermore, the expected dependence of the pore size on solidification rate, due to restricted feeding, was direct (i.e., the greater the solidification rate the larger the pore size as discussed in 3.4.2) rather than the inverse as observed in the experiments. Based on this conclusion, models simulating the diffusion limited pore growth were developed and applied to different aluminum alloys [57-60, 62, 63, 86].

In these diffusion controlled growth models, the pores were assumed to be distributed in a regular array within the liquid. The diffusion region around a pore was approximated as a sphere and the hydrogen rejected from the solid increased the background liquid concentration uniformly. Fick's second law was applied and a spherical coordinate system was used to solve for the hydrogen concentration field in the liquid. A time

dependent source term was used to represent the hydrogen rejection due to solidification. Atwood *et al.* [51] used a diffusion model for a representative average pore assuming all pores nucleated at the same time. The results showed good agreement to experimental observations undertaken with Al-7wt%Si alloy. Although fluid flow was not included in the models, both the average pore size and the growth of the pores were well predicted.

It was also proposed that this diffusion model could consider the continuous pore nucleation feature to predict the final size of each detected pore [58, 63]. In the continuous nucleation model pores nucleate at experimentally determined undercooling [58] or supersaturations [63] according to the X-ray temperature gradient stage (XTGS) observations. The growth rate of the nucleated pores can be calculated by solving the diffusion equations; therefore, the final size of the pores can be predicted at the end of solidification.

3.6.4 Integrated macro-scale interdendritic flow and micro-scale diffusion controlled growth models

The above diffusion models were based on the XTGS observations, which indicated that the pressure drop caused by shrinkage is negligibly small for Al-7Cu alloys. However, when the shrinkage effect is significant, the fluid flow and the pressure drop due to restricted liquid feeding should be solved as well. Most recently, Carlson *et al.* developed a model in which gas species transport in the melt was coupled with continuity equations solving for the feeding flow and pressure field [78]. The fluid flow and pressure field were calculated by solving the continuity equation and volume averaged momentum equation. The effect of finite-rate gas diffusion was modeled using a volume-averaging approach. Following the same volume averaging principles used by Ni and

Beckermann [153], a gas species conservation equation for the pore phase was used to solve for the evolution of porosity fraction. The average pore radius was a function of the porosity fraction and the measured number density of the pores. Because the pressure field and feeding flow calculations were included, this study modeled both shrinkage related and gas related porosity. The results showed good agreement between the predicted and previously measured pore volume in directionally solidified, unmodified A356 alloys.

In a similar approach, Backer proposed an algorithm that combined the governing equations in the conventional interdendritic flow and hydrogen diffusion models [151]. A finite element model having a characteristic mesh spacing of 5 mm was used to allow an economical use of computational resources. The model was calibrated against literature data of maximum pore length and volume fraction for binary Al-7wt%Si alloys, and subsequently applied to a chill plate test casting in A356 alloy and to an engine block in 319 alloy. The limitation of the model was addressed by the author that the algorithm did not consider the effects of process variables on pore nucleation kinetics, and the effect of grain size and shape on pore morphology.

More recently, Felicelli used a multicomponent solidification program to calculate macrosegregation and transportation during the solidification, coupled with a microscale hydrogen diffusion pore growth model in aluminum and magnesium alloys [154]. The criterion for the formation of pores is based on the equilibrium conditions between the pores and the alloy and on the transport of a pseudo-solute that represents the inclusions or impurities dissolved in the alloy. The porosity model requires two parameters, the initial pore size and the concentration of inclusions. These two parameters can be linked

to measured data. It was shown that the simulations with A356 with the same set of parameters were able to reproduce the experimental data with reasonable agreement for different castings with varying levels of hydrogen content.

It should be noted that the nucleation sites in these models were considered as being activated simultaneously and their total number was a constant input parameter in the model. Therefore, the stochastic nature of pore nucleation was not included.

3.6.5 Cellular automata (CA) model

A CA modeling approach can be used to simulate porosity formation using the theoretical bases of both the interdendritic flow-shrinkage and diffusion controlled pore growth model. It is usually listed separately due to its unique technique that simulates nucleation and growth of both pores and solid grains. The CA model consists of a regular grid of cells. Three types of cells are present in the domain, corresponding to solid, liquid and gas phases. The location of their nuclei is distributed randomly in the domain. The nucleation of solid grains is a function of local undercooling based on the heterogeneous nucleation theory. The growth of individual grains and dendrites is modeled using growth rates either analytically prescribed [155] or predicted from solute concentration balances[86]. As for microporosity, the temperature at which pores are nucleated depends upon the degree of local supersaturation of hydrogen as shown in previous experimental observations [57, 63]. The CA models to date describe pore growth via a hydrogen diffusion equation as in the diffusion controlled growth model.

While the results from CA have been promising, they require an extremely refined mesh size. Where interdendritic flow models can use mesh dimensions in the scale of millimeters, CA requires mesh dimensions in the scale of micrometer. As a result, CA is

generally applied to casting submodels that use thermal and fluid flow data predicted from a macroscale model. It is not considered practical in industrial applications where computational efficiency is a critical requirement.

4 X-ray Micro-tomographic (XMT) Characterization of Microporosity in A356 Aluminum Alloy Castings¹

This chapter presents the study of the effect of hydrogen content and the solidification conditions (cooling rate, temperature gradient and degassing time) on the volume fraction and size distribution of microporosity in directionally solidified aluminum alloy A356. Characterization via both conventional metallography and X-ray microtomography (XMT) was performed. The purpose of conducting both types of analyses was to explore limitations in both techniques. In the case of the metallographic surface-based approach, there are known limitations in the extent that it can be used to accurately determine the pore volume fraction and pore morphology as described in Section 3.5.1. In the case of the X-ray-based method, the intent was to explore the ability of the equipment available to characterize the porosity at the small end of the size distribution. The results from this study will be used in Chapter 5 to validate the model developed to predict pore formation in A356 alloys.

4.1 Experimental methods

4.1.1 Casting procedures

Ingots of aluminum alloy A356 of the nominal composition indicated in Table 4.1 were melted in a commercial reverberatory furnace, poured into a ladle, and degassed with argon using a commercial rotary degassing unit at the Canadian Autoparts Toyota

¹ A version of this chapter has been published as: Omid Lashkari, Lu Yao, Steve Cockcroft, Daan Maijer, “X-Ray Microtomographic Characterization of Porosity in Aluminum Alloy A356”, Metallurgical and Materials Transactions A: Volume 40, Issue 4 (2009), Page 991.

Inc. (CAPTIN) casting facility located in Delta, BC, Canada. The degassing times were 0.5, 1.0 and 2.0 minutes, yielding melts of high, medium and low initial hydrogen content. Following degassing, liquid metal was manually poured at 700 °C (~85 °C superheat) into a fireclay mould with a water-cooled copper chill located at the bottom. The mould was at an initial temperature of 25 °C. A schematic of the mould assembly and configuration is shown in Figure 4.1. The mould was insulated on the sides and designed to directionally solidify the casting from the bottom to the top, thereby providing a range of solidification conditions and avoiding macroporosity formation. Five K-type thermocouples were positioned within the mould at 5, 15, 35, 55, and 70 mm from the chill to measure the evolution of temperature with time, as shown in Figure 4.1. The data from the thermocouples were recorded at a rate of 2 Hz. The mould configuration yielded tapered cylindrical samples weighing ~630 g that were ~75 mm in height with a diameter of 50 mm at the base (chill) and ~70 mm at the top.

The hydrogen content was analyzed using a LECO ¹ RH-402 analyzer at Alcoa Primary Metals Division Laboratory (Frederick, MD). The technique is reported to yield results accurate to within 0.01 cc/ 100g-Al. The technique involves remelting a 100 g sample of the as-cast material and yields a bulk hydrogen content in each sample. Table 4.2 shows the results for the various degassing times in both cc/100g-Al, the commonly used industrial unit, and ppm.

Table 4.1: Nominal chemical analysis of the aluminum alloy A356 (wt%)

Si	Mg	Fe (max)	Cu (max)	Ni (max)	Ti	Al
6.9-7.1	0.32-0.35	0.1	0.002	0.001	0.12-0.13	Bal.

¹ LECO is a trademark of LECO Corporation, St. Joseph, MI.

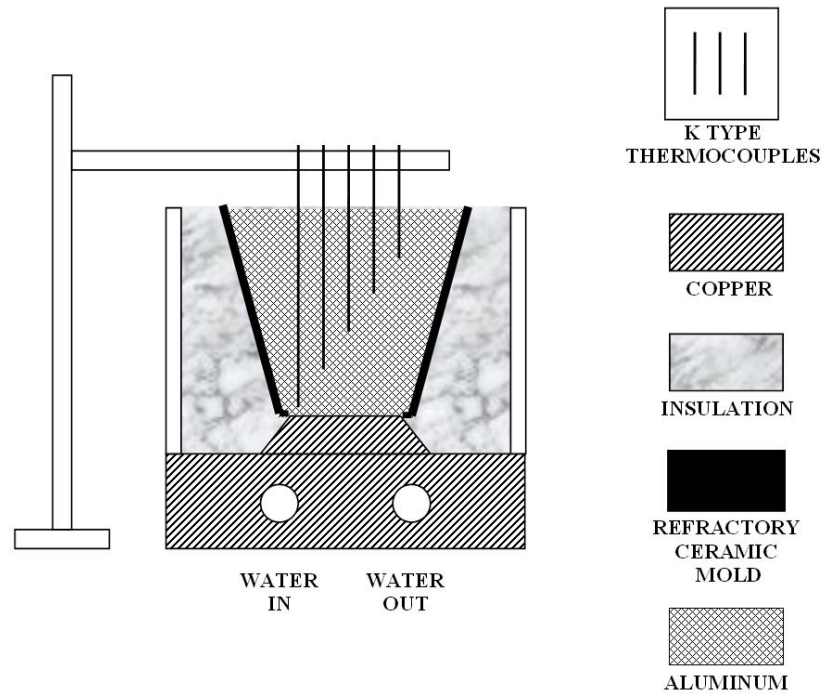


Figure 4.1: Schematic of the mold configuration and the thermocouple positions.

Table 4.2: Hydrogen content as a function of degassing time

Degassing Time (min)	H content cc/100g-Al [ppm]
0.5	0.28 [0.32]
1.0	0.18 [0.20]
2.0	0.10 [0.11]

4.1.2 3-D XMT analysis

In this work, the absorption mode was used to obtain contrast between porosity and aluminum alloy based on Beer-Lambert law [68], which states the transmitted X-ray intensity is related to the absorption coefficient of the material and the path that the

photons travel through the sample: $I = I_0 \exp(-\mu x)$, where I is the transmitted X-ray intensity, I_0 is the intensity of the source X-ray, x is the distance the X-ray travels through the sample, and μ is defined as the linear attenuation coefficient, which is a parameter dependent on the density and the atomic number of the material.

To conduct the X-ray tomographic analysis, a cylindrical sample of 4.5 mm in diameter and 70 mm in length was machined from near the centre line of the cast samples. The analysis was conducted with a medical micro-CT unit, SCANCO μ CT 35TM, at the Hip Health Research Institute in Vancouver, BC, Canada. The SCANCO μ CT 35TM unit is a high-resolution desktop cone beam scanner equipped with a micro-focus white light X-ray source and a 2048 x 256 element detector. The spatial resolution is 3.5 μ m and was achieved by adjusting the acceleration voltage to maximum 76 kv (to adjust X-ray intensity) and a beam current of 160 μ A (to adjust the X-ray spot size). The 2D images were recorded on the detector while the sample rotated along its base line: the integration time was 800 ms with 1000 projections during 180° rotation. These 2D images were reconstructed into 3D based on the Feldkamp algorithm[156, 157]. A scan was performed at each height corresponding to the thermocouple locations. Each scan included 462 slices, corresponding to a length of 1.617 mm and a volume of 25.7 mm³. A three-dimensional image was generated from a series of two-dimensional X-ray images using the softwares ImageJTM and AMIRATM.

4.1.3 2-D optical analysis

To facilitate the optical microscopy (OM) analysis of porosity, the cast samples were cut in half normal to the base plane. One half was milled flat, polished down to 0.1 μ m with procedures shown in Table 4.3 and etched using 0.5% HF solution.

Table 4.3: Procedures for preparation of metallographic samples

Procedure	Abrasives	Lubricant	Duration
Coarse grinding	SiC grinding paper: 120, 400, 600, 800,1000 grit progressively	Water	10 minutes each grit
Fine polish	Polish cloth + diamond suspension: 6 μm and 1 μm	Red polish lubricant oil	10 minutes each scale
Final polish	Polish cloth + colloidal silica: 0.1 μm	Red polish lubricant oil	5 minutes

A Nikon ¹ EPIPHOT 300 microscope, equipped with a QImaging² micropublisher digital camera, and CLEMEX³ image analysis software were used to measure and characterize the fraction and size distribution of the porosity on the polished face at five different heights corresponding to the thermocouple locations. The analysis at each height consisted of 36 analysis fields with a total area of 172.8 mm². The area percentage (pct) and equivalent circular diameter (μm) of the pores were quantified. The microstructure of the as cast samples was also examined, and photos were taken at 50 times magnification, which is reported to yield a $\sim 0.29 \mu\text{m}$ resolution.

4.2 Results and discussions

4.2.1 Solidification conditions

The cooling curves for the experimental castings are shown in Figure 4.2. Within each sample a wide range of solidification conditions were achieved. The data from the 70 mm thermocouple (slowest cooling rate) clearly show the thermal arrests associated with primary $\alpha\text{-Al}$ formation at $\sim 615 \text{ }^\circ\text{C}$ and the main eutectic transformation at $\sim 565 \text{ }^\circ\text{C}$. Both

¹ Nikon is the trademark of NIKON Corporation, Tokyo, Japan.

² QImaging is the trademark of Qimaging Corporation, Surrey, BC, Canada.

³ CLEMEX is the trademark of Clemex Technologies Inc., Longueuil, QC, Canada.

transformations have been identified on the figure. The thermal arrests gradually become less pronounced with increasing cooling rate as would be expected.

Figure 4.3 shows the variation in cooling rate as a function of distance from the chill, which was calculated as the average over the solidification temperature range, i.e., the temperature decrease between liquidus and solidus divided by the time duration for solidification. The data show a decrease in the cooling rate from approximately 4 °C/s to 10 °C/s at the bottom of the casting adjacent to the copper chill to approximately 0.35 °C/s at the top of the casting. Note that for the two locations close to the top of the casting, the variation of cooling rate is not as obvious as it is at the bottom. This may be as a result of heat transfer to the surroundings at the top surface of the casting and its earlier solidification than the melt beneath.

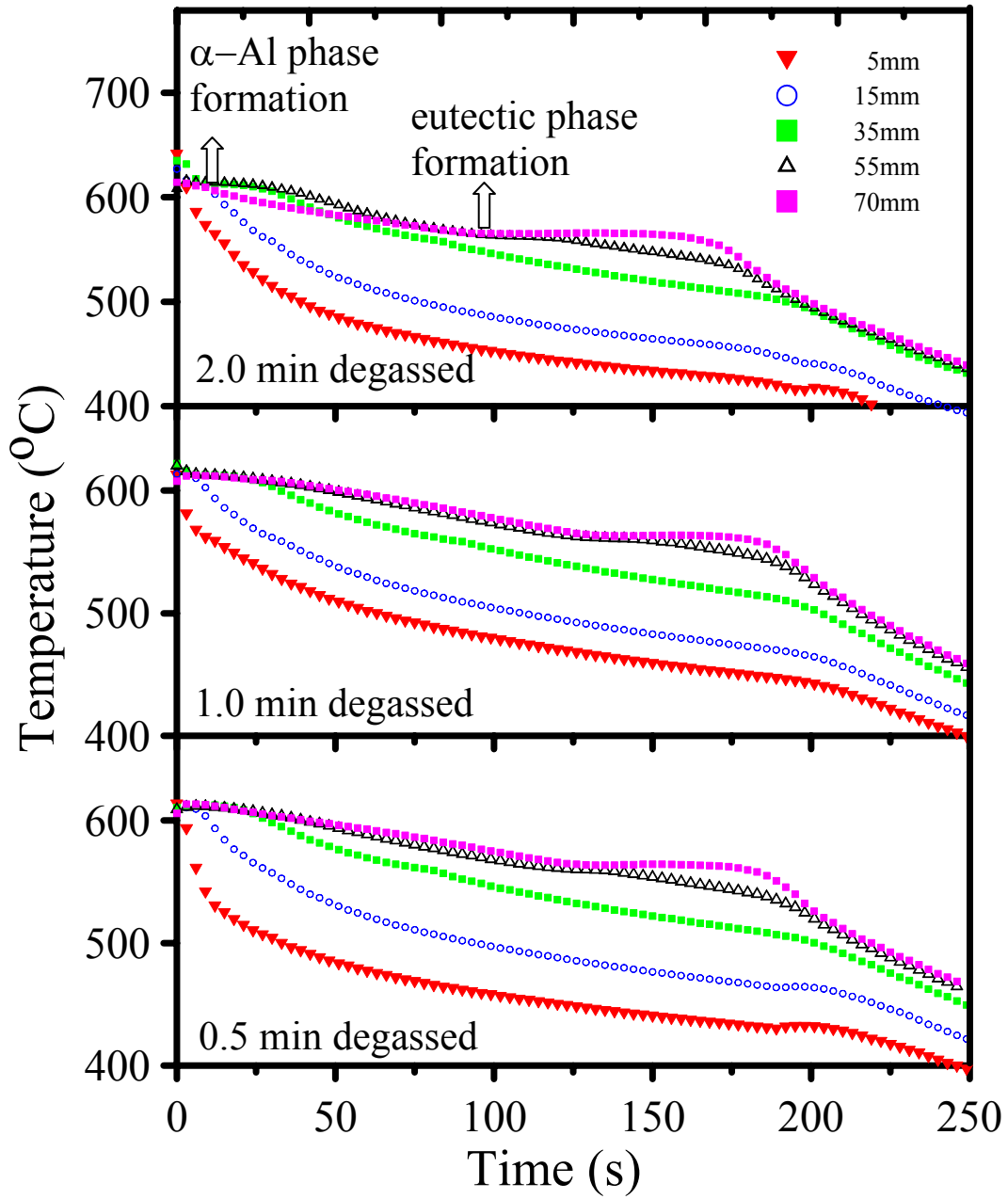


Figure 4.2: Cooling curves at different distances from the chill in the 0.5, 1.0 and 2.0 min degassed samples.

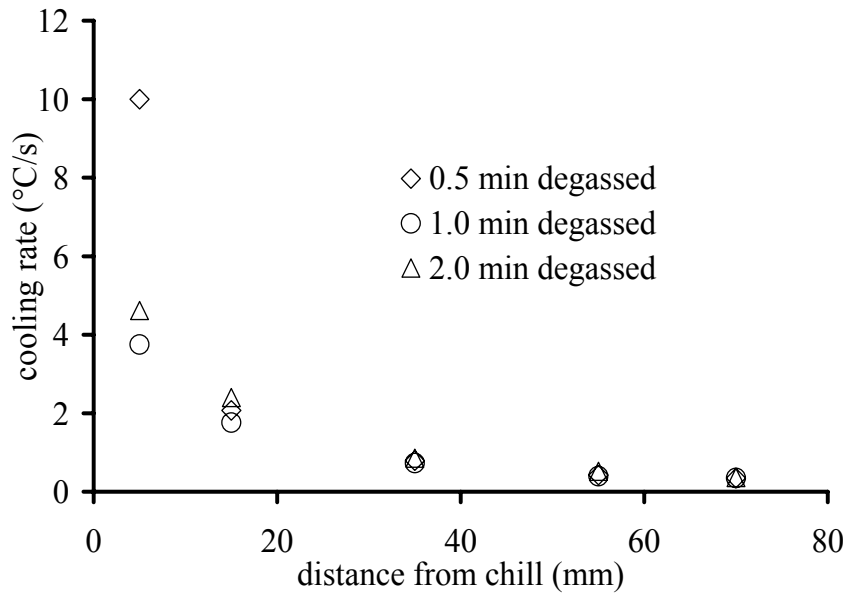


Figure 4.3: Cooling rates during solidification as a function of distance from the chill.

4.2.2 Assessment of errors in XMT analysis

The errors and uncertainties in the XMT analysis are from determination of grayscale, minimum detectable pore size and the sample size used in the measurement.

Figure 4.4(a) shows a typical two-dimensional (2-D) image of a single XMT data slice. The pores within the image appear as a dark shade of gray. A section of the image containing a large pore has been magnified. In this particular alloy, the solidification microstructure is not revealed, because there is not a significant attenuation difference between the primary α -Al phase and the eutectic phases.

The process of extracting microstructural information (pores or different phases) from X-ray microtomographic and OM data is not straightforward. The process hinges on determining the threshold grayscale values that delineates features. Features are extracted by splitting the image based on the grayscale threshold, one portion to metal and the other to porosity. If there is phase contrast in the metal, it would be possible to extract different

phases by choosing the appropriate threshold values. This process is made difficult at the boundaries of features, where a pixel represents both void and metal. The tools available within the image analysis package and the judgment and skill of the operator are also factors. Using Figure 4.4(a) as an example, its grayscale value vs pixel number density is plotted as Figure 4.4(b), where the grayscale values range from 0 to 255. By adjusting the grayscale judiciously, the operator is able to effectively separate the real voids (pores) from the matrix. To illustrate this process, the image presented in Figure 4.4(c) was obtained by setting the grayscale threshold to 238. There are numerous dots that appear in the image that are not porosity. Reducing the grayscale threshold to 218 results in Figure 4.4(d), which is believed to be near the optimum value for this image. Reducing the grayscale threshold to 198 results in Figure 4.4(e), the obvious loss of porosity can be seen. The error associated with the determination of grayscale is found to be approximately 10% for pore volume fraction.

In order to interpret the X-ray tomographic data, the minimum detectable feature size must be considered. In the current study, the maximum resolution of the machine is claimed to be $3.5 \mu\text{m}$, and therefore, 1 voxel is $3.5 \times 3.5 \times 3.5 \mu\text{m}^3$ in size. In order to reduce the risk of error in the size and number, all the pores with volumes less than 27 $(3 \times 3 \times 3)$ voxel³, $\sim 6.5 \mu\text{m}$ radius, have been excluded in the three-dimensional (3-D) image analysis results.

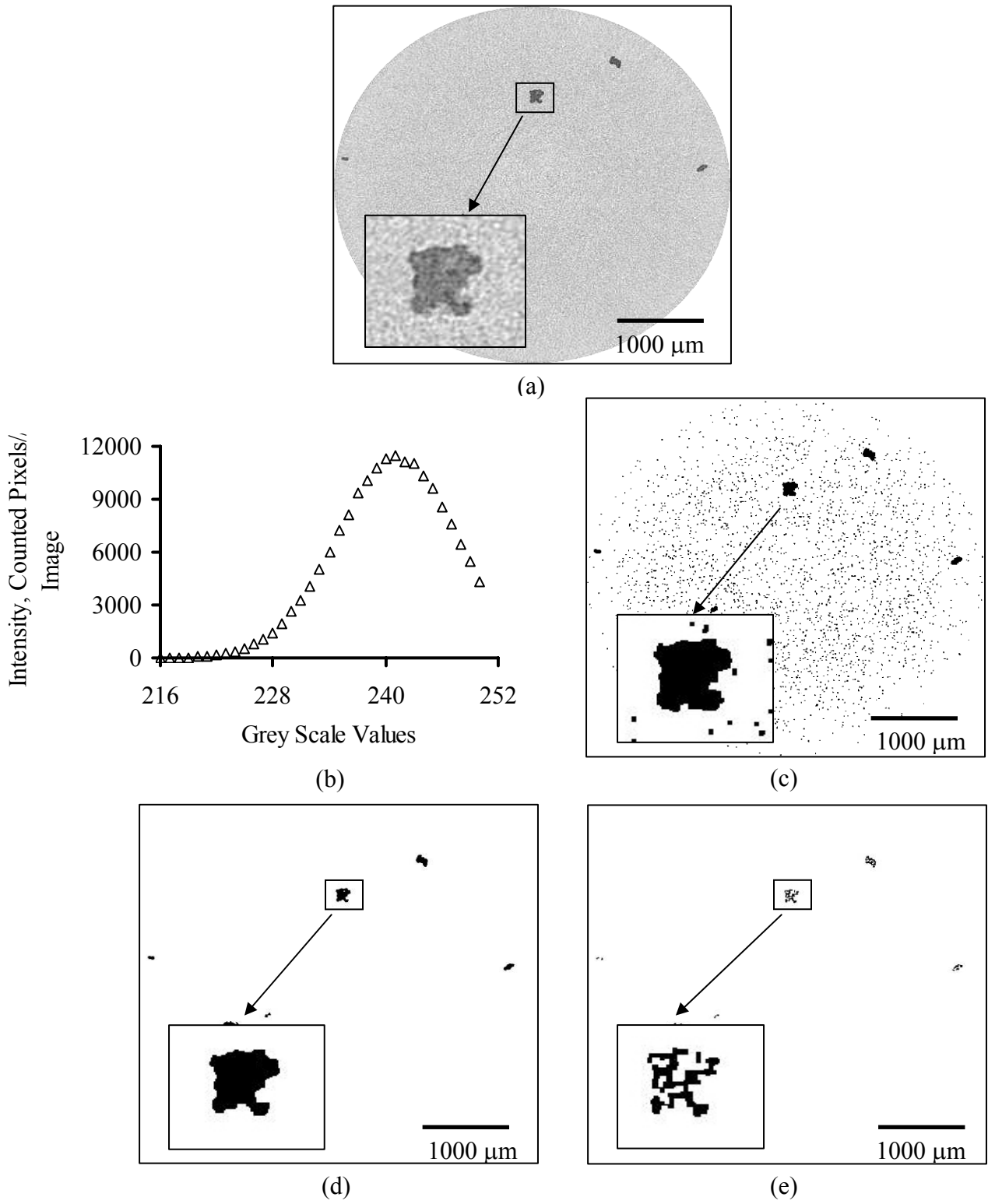


Figure 4.4: (a) Sample X-ray tomographic image of the cast metal and porosity, (b) typical color intensity versus grayscale values for a X-ray tomography image, (c) Porosity, assuming grayscale threshold of 238, (d) Porosity, assuming greyscale threshold of 218, and (e) Porosity, assuming greyscale threshold of 198.

One possible source of uncertainty in the XMT analysis is sample size. In general, the uncertainty in the quantification of the volume fraction and pore size distribution decreases as the sample size increases. The 3-D XMT data at each vertical location is comprised of 462 2-D slices that are assembled to produce the 3-D data set, corresponding to a total volume of 25.7 mm^3 and a total number of 156 pores. To assess the effect of sample size on the measurement, sub-volumes of 6.5 mm^3 , 12.9 mm^3 and 19.3 mm^3 were selected from the total volume. The pore volume fraction was calculated based on each sub-volume and compared with that calculated based on the total volume. Figure 4.5 shows the volume fraction as a function of the sub-volume size that was analysed. It is shown that the volume fraction obtained from a sub-volume becomes closer to the volume fraction obtained from the total volume as the sample size increases. At a volume of 12.9 mm^3 the deviation is 8.4% and decreases to 1.0% as the volume increases to 19.3 mm^3 .

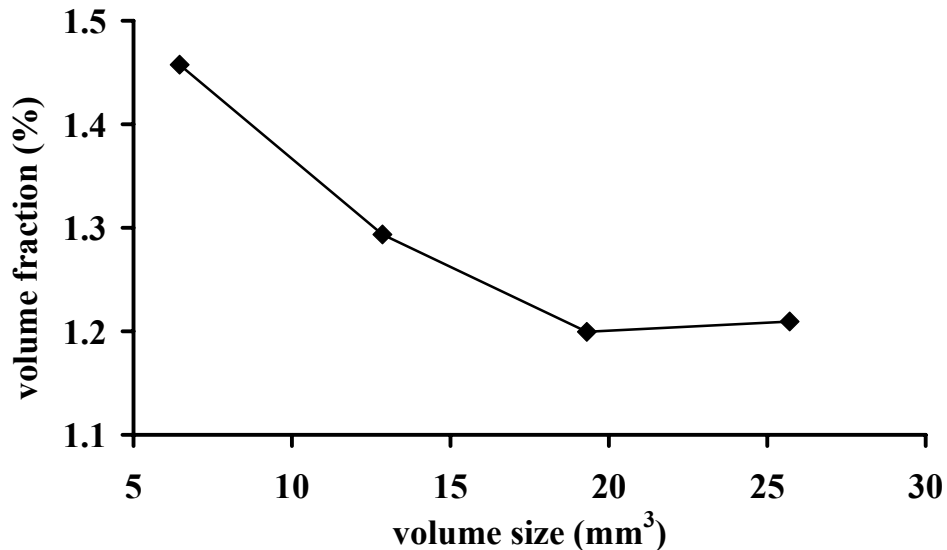


Figure 4.5: Variation of measured pore volume fraction with sample sizes in the 3-D XMT analysis.

Figure 4.6 shows the pore size distributions in a volume of (a) 25.7 mm^3 and (b) 12.9 mm^3 . It is shown that pore size shows similar distribution in these two volumes, indicating the pore size distribution is independent from volume size above 12.8 mm^3 . Therefore, a volume of 25.7 mm^3 in this study is sufficient to obtain a reliable pore size distribution.

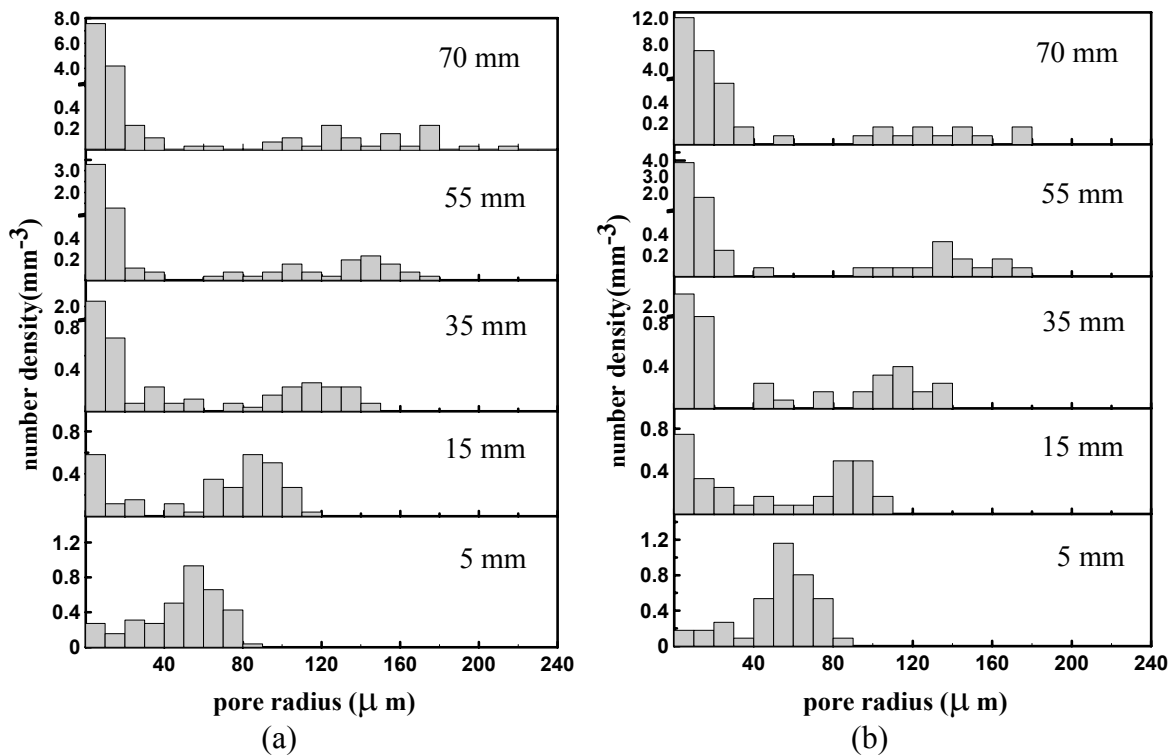


Figure 4.6: Pore size distributions in a volume of (a) 25.7 mm^3 and (b) 12.9 mm^3 from the XMT analysis.

4.2.3 Comparison between XMT and OM analysis

Figure 4.7 shows the volume fraction of porosity determined by 3-D XMT analysis and the average area fraction determined from 2-D OM analysis at different distances from the chill in the 0.5-min degassed sample. The 3-D XMT data at each vertical location is comprised of a large number (462) of 2-D slices that are assembled to produce the 3-D data set. The 2-D XMT slices can be processed individually to obtain area fraction porosity data for each slice, which can in turn be compared to the 2-D OM derived data and the 3-D XMT data. Figure 4.7 compares these 3-D and 2-D derived data for porosity fraction. The error bars in the graph represent the standard deviation of area fraction processed individually from the total 462 2-D slices. As can be seen from the figure, all three methods yield the same trend in behaviour, i.e., a general increase in

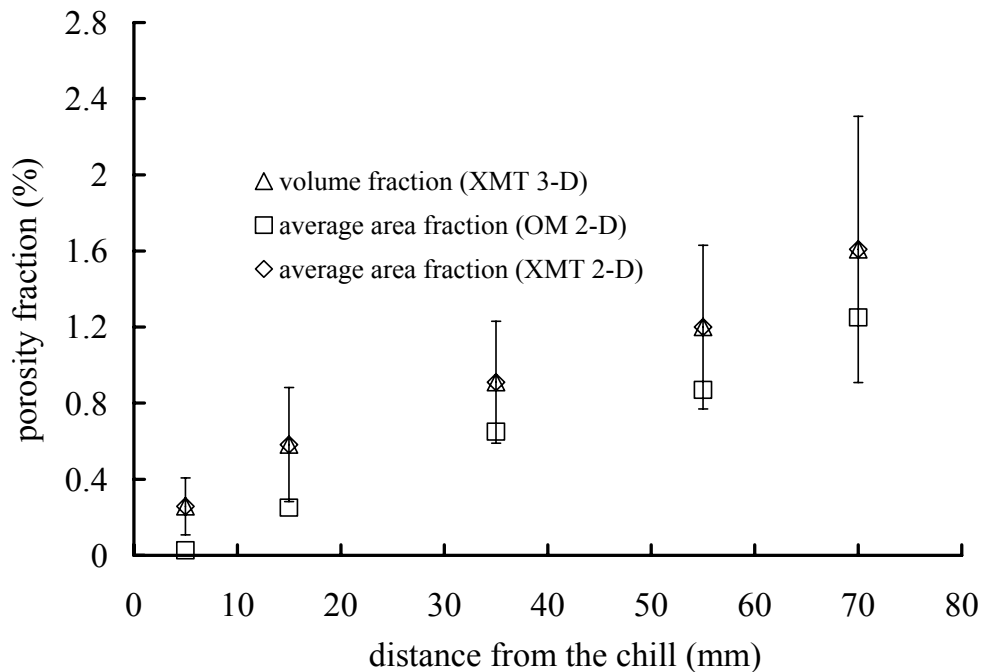


Figure 4.7: Variation of porosity fraction as a function of distance from the chill for the 0.5-min degassed sample.

either area fraction or volume fraction of porosity with increasing distance from the chill. The average area fraction determined from the 2-D XMT slices agrees exactly with the volume fraction predicted from the 3-D XMT data, which would be expected. The error bars associated with the averaged 2-D XMT data represent the standard deviation in the data. The 2-D OM derived data largely fall within the standard deviation band derived from the 2-D XMT data. The two notable exceptions arise in the data nearest to the chill. The reason for this is unclear and could relate to the small pore size in this region and the potential for some of the smaller pores to be lost due to the mechanical polishing process (pores were filled by material smeared by the abrasive action of the diamond particles) used to prepare the OM samples. It is also interesting to note that the standard deviation increases with increasing distance from the chill, which presumably relates to the presence of larger pores and the increase in variability that is associated with a 2-D plane intersecting a large tortuous pore at a random location.

Figure 4.8(a) presents a size distribution analysis performed on the XMT data. The x -axis is the radius of an equivalent spherical pore containing the same volume. The y -axis is the number density (mm^{-3}) within the corresponding size range or bin. Each bin has been set to a width of $10\ \mu\text{m}$. The results indicate a range of equivalent pore radii at each height from 5 to 70 mm from the chill. At 5 mm from the chill, the size of pores ranges from 6.5 to $90\ \mu\text{m}$; at 15 mm, from 6.5 to $120\ \mu\text{m}$; at 35 mm, from 6.5 to $150\ \mu\text{m}$; at 55 mm, from 6.5 to $180\ \mu\text{m}$; and at 70 mm, from 6.5 to $220\ \mu\text{m}$. Thus, there is a trend to increasing maximum pore size with increasing distance from the chill. As is shown at all

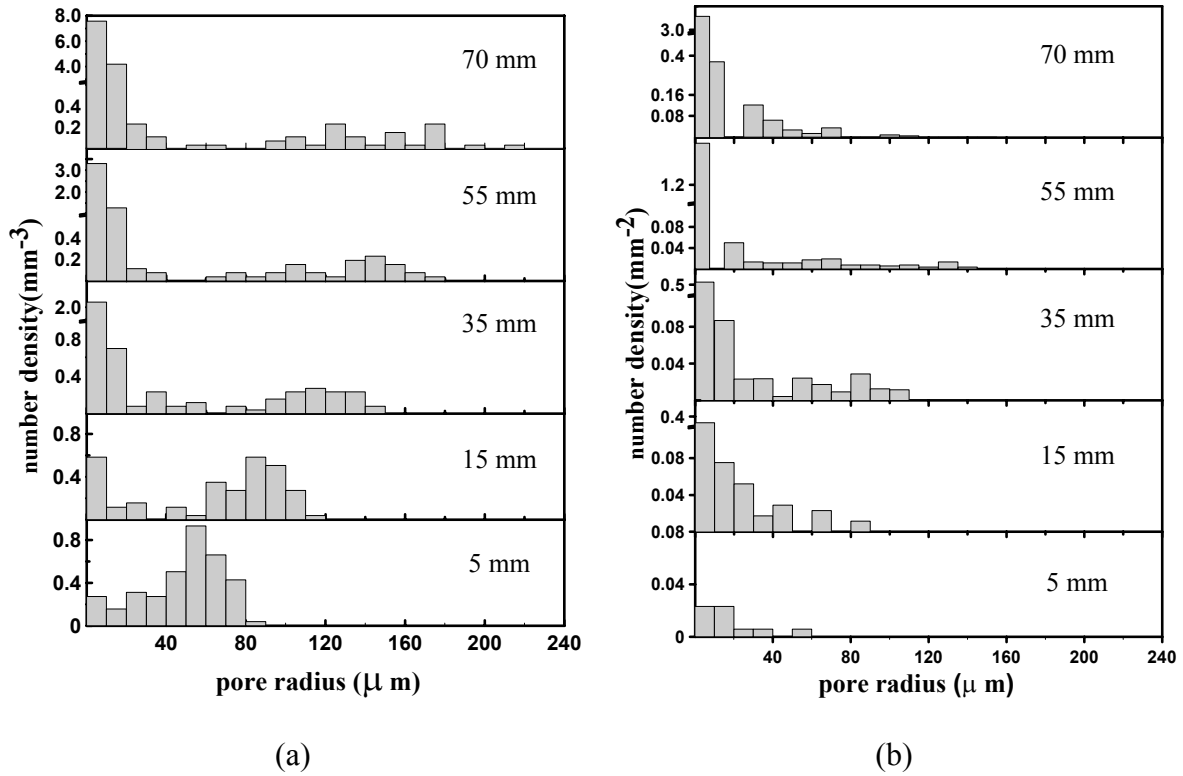


Figure 4.8: The pore size distribution for the 0.5-min degassed sample based on (a) the radius of a spherical pore occupying the same volume from 3-D XMT measurement and (b) a circular pore occupying the same area from 2-D OM measurement.

heights except 5 mm from chill, the data reveals a bimodal distribution of pores, with one population of large pores and a second population of small pores with few of an intermediate size present. The population of larger pores gradually shifts to larger equivalent radii with increasing distance from the chill. Moreover, the number of pores within the two smaller bin sizes, 0 to 10 μm and 10 to 20 μm , gradually increases with increasing distance from the chill. Since the pores with radii less than 6.5 μm were excluded from the final analysis due to resolution issues, this would appear to be a real result and not an artifact of the analysis method. There may well be many smaller pores present below the resolution limit of the current analysis.

The observation of a bimodal distribution is consistent with a two-stage porosity formation mechanism proposed by Zhu *et al.* [23], in which the large population is primarily driven by hydrogen exceeding the solubility limit of the gas in the liquid during the early stages of solidification, and the second smaller sized population is linked to the sudden drop of local pressure caused by a lack of liquid feeding at the end of solidification. This sudden pressure drop results in a second round of pore formation at the end of mass feeding. The lack of this population in the material adjacent to chill may be a result of the fine grain size and inability to resolve the very small pores that would form in this region during the last stages of solidification.

Figure 4.8(b) shows the equivalent size distribution analysis obtained from OM analysis of the 0.5-min degassed sample. A comparison to the results from the XMT analysis (Figure 4.8(a)) clearly shows several differences between the two sets of data. First, the OM analysis produces a consistently lower number density across the entire range of equivalent pore radius. Second, there is a significant reduction in the number of the larger pores found using the OM technique. As a result, the OM data do not reveal a bimodal distribution of pores. The results of a comparison between the XMT and OM techniques for measuring the pore volume fraction and size distribution have clearly identified the shortcomings of the optical-based method and point to the need to conduct a large number of 2-D OM analyses to obtain an accurate representation of these quantities. Moreover, it would appear that in fine-grain structures there may also be a systematic bias introduced in the number of small pores by mechanical polishing. Unfortunately, both methods do not currently lend themselves to routine industrial application. They remain limited to the analysis of small sections only, requiring

destruction of the component for sample preparation. Furthermore, there is a significant amount of time needed to complete the analysis. Of the two, the XMT method involves the least amount of work and has the shortest turnaround. Further advances in the instrumentation and software will improve this in the future.

4.2.4 Effect of cooling rates and hydrogen content on porosity fraction

Figure 4.9 shows the volume fraction of pores as a function of distance from the chill for the samples with varying hydrogen content as determined from the XMT analysis and Figure 4.10 re-plots the same data as a function of cooling rate. The error bars represent the deviation in the measurement associated with determination of grayscale threshold used to distinguish the pores from matrix in the XMT analysis, as discussed in 4.2.2.

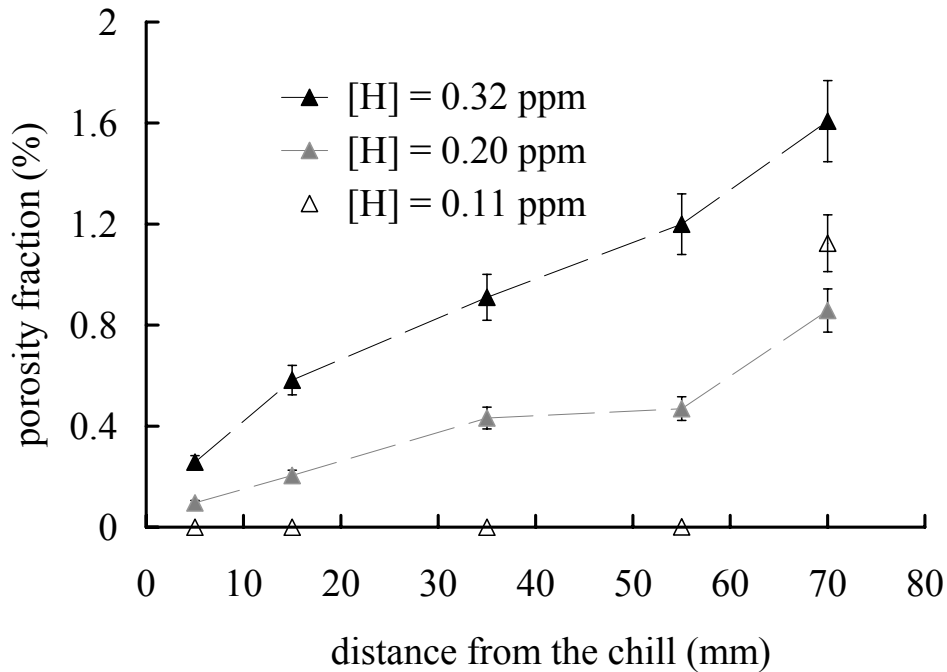


Figure 4.9: Porosity fraction at different distances from the chill at high, medium and low hydrogen contents.

Comparison of the 0.5-min, 1.0-min and 2.0-min degassed samples shows that the fraction of porosity increases with increasing hydrogen content (decreasing degas time). In addition, as can be seen the porosity fraction generally increases as cooling rate decreases; however, there are a couple of exceptions to this behavior. One exception is that there is no variation observed in the 2.0-min sample between 5 and 55 mm from the chill as there is no measurable volume fraction porosity. This behavior is presumably due to the fact that the initial hydrogen content ($[H] = 0.11\text{ppm}$) in the 2.0-min sample is too low to reach supersaturation resulting no nucleation and growth of pores. The other exception is that in all three samples, the volume fraction increases dramatically at 70 mm location, where there is little change in the cooling rate. This can be explained by the different solidification conditions existing near the top of the casting. Since the casting is subject to some loss of heat at the top, the top surface of the casting freezes over prior to the complete solidification of the casting. When this happens, the liquid beneath the top surface is encapsulated and the local pressure drops due to cut-off from liquid feeding and the atmosphere. This pressure drop results in a decrease of pressure inside the pores and drives the pore growth in a manner that decouples the pore volume fraction from both hydrogen content and cooling rate, as discussed in 3.3.2.

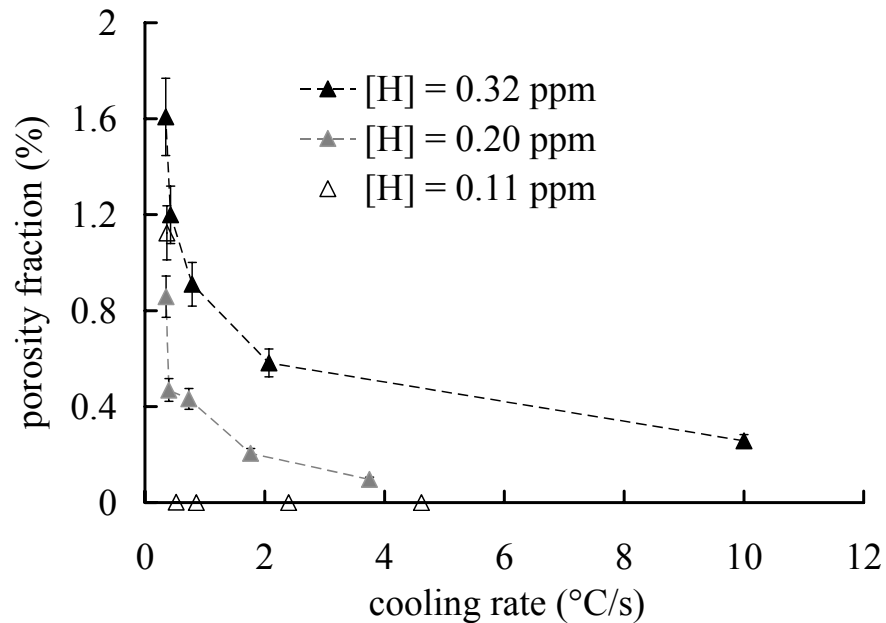
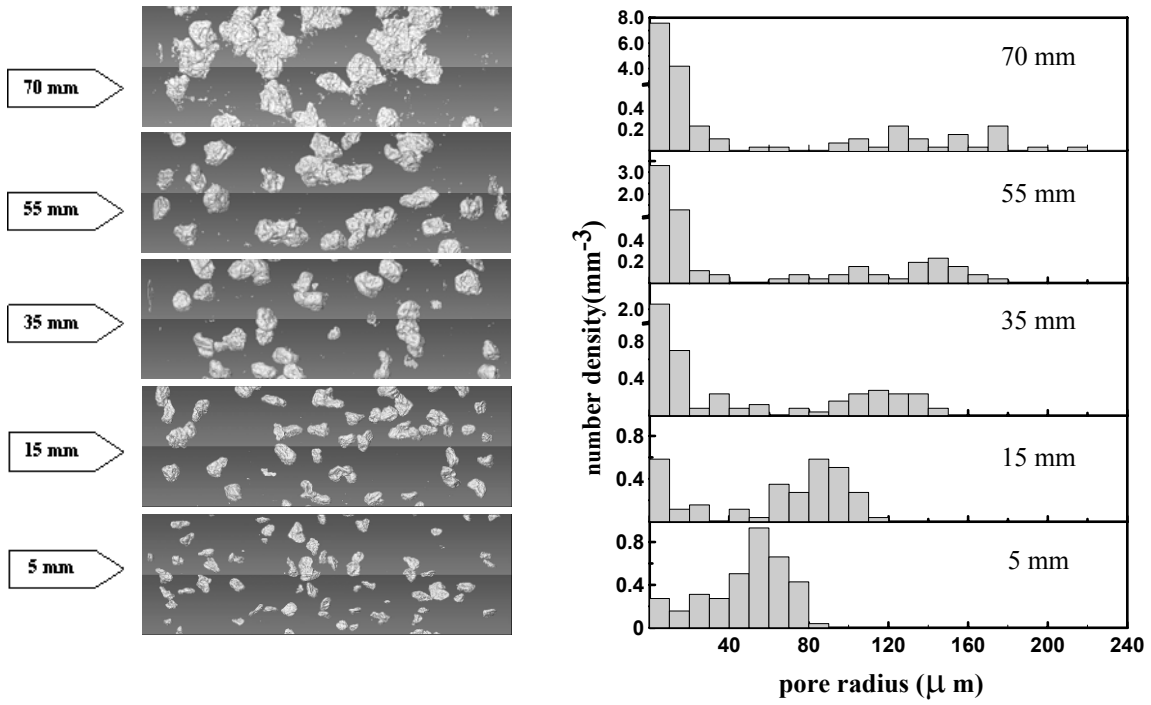


Figure 4.10: Porosity fraction as a function of cooling rate at high, medium and low hydrogen contents.

4.2.5 Effect of cooling rates and hydrogen content on pore size distribution

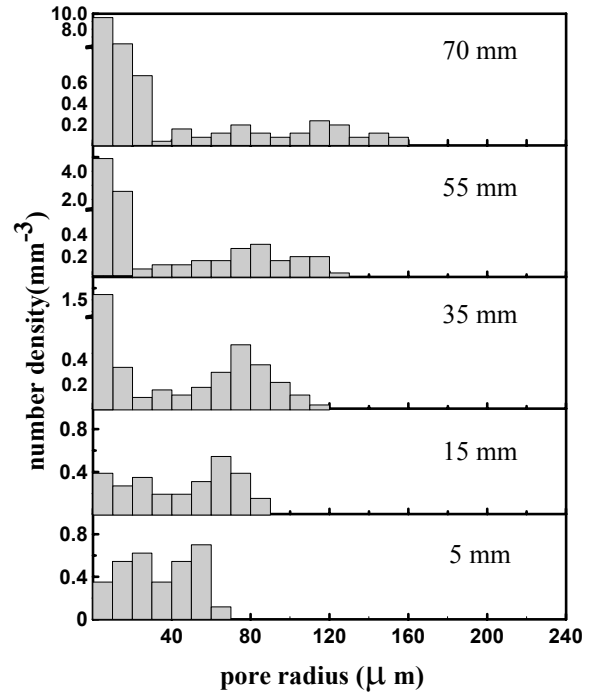
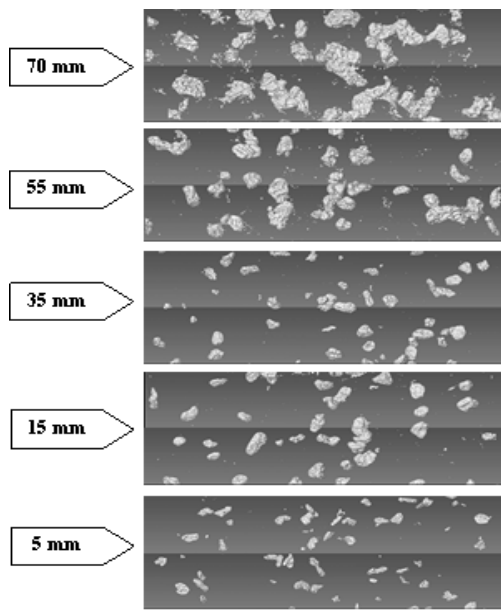
Figure 4.11 to Figure 4.13 show the pore size distribution from XMT measurement. In each figure, the series of images labelled as (a) represent a 2-D rendering of the actual 3-D porosity at different distances from the chill. Each scan represents 1.617 mm in sample height and therefore there are significant regions between each scan that have not been rendered. It is clearly shown that the pore size increases from bottom to top as cooling rate decreases. At the top of the casting, many of the larger pores have very complex and tortuous shapes indicating that during growth they impinged on the developing structure and in some cases may have formed as a result of the coalescence of one or more adjacent pores.



(a)

(b)

Figure 4.11: (a) 3-D rendering of the pores and (b) pore size distribution at different height in the 0.5-min degassed sample with an initial hydrogen content 0.32 ppm.



(a)

(b)

Figure 4.12: (a) 3-D rendering of the pores and (b) pore size distribution at different height in the 1.0-min degassed sample with an initial hydrogen content 0.20 ppm.

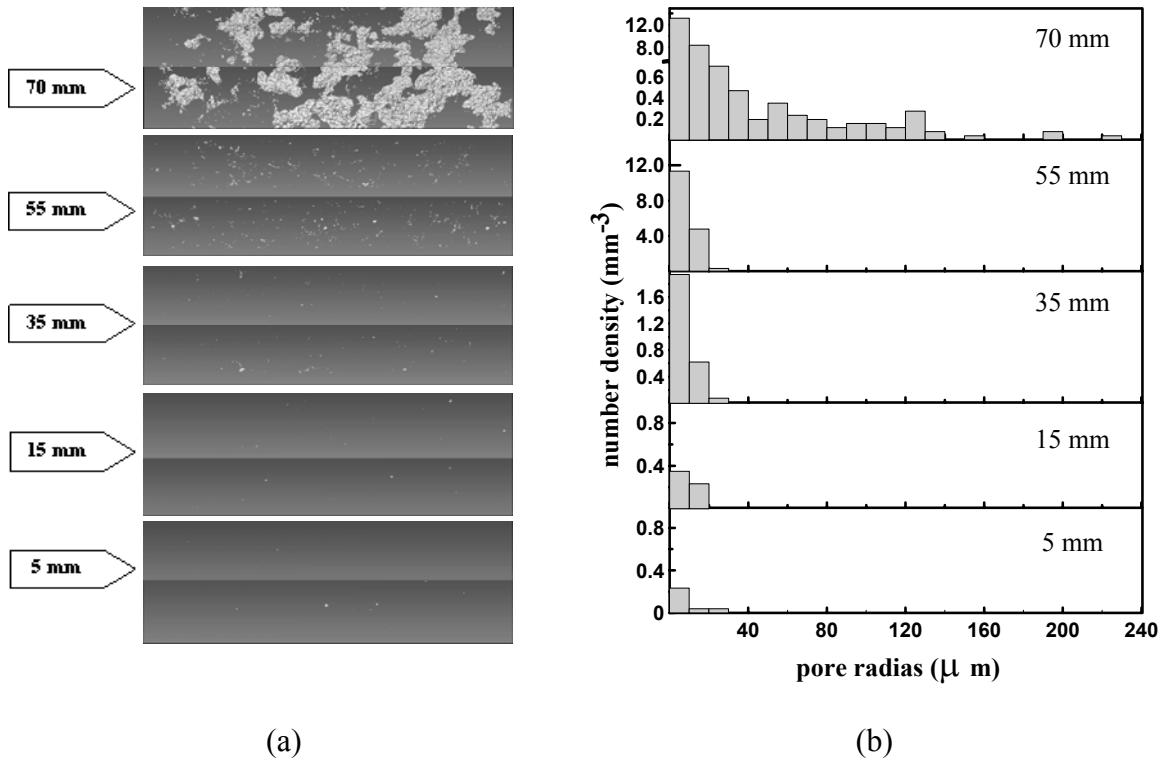


Figure 4.13: (a) 3-D rendering of the pores and (b) pore size distribution at different height in the 2.0-min degassed sample with an initial hydrogen content 0.11 ppm.

The effect of degassing time can be seen by comparing Figure 4.11 to Figure 4.13. There is a clear trend to smaller pore radii when the initial hydrogen content is reduced from 0.32 ppm to 0.11 ppm. At 0.11 ppm, only the small pores (below 40 μm in radius) in the bimodal distribution were observed at locations up to a height of 55 mm from the bottom. This indicates that hydrogen contributes to the formation of the distribution of the larger pores within the bimodal distribution. However, at the top of the castings large portion of porosity with torus geometry is present. The maximum pore size and porosity fraction are comparable with samples of higher hydrogen content. Therefore, they are less likely to form due to hydrogen. This confirms the previous hypothesis, that they are

formed from shrinkage of isolated liquid pockets when mass feeding stops due to the loss of directional solidification at the top surface.

4.3 Summary and conclusions

The initial hydrogen content and cooling rate of aluminum A356 alloy were found to have a strong impact on the volume fraction and size distribution of porosity under the experimental conditions examined. Comparison of 2-D optical image analysis and 3-D XMT analysis reveals that both are able to measure the trend in variation of porosity with distance from the chill. The OM-based analysis will, in general, result in a quantitative measurement and can lead to estimations that are too high or low. The 3-D analysis of the size distribution of porosity found in the 0.5-min and 1.0-min degassed sample revealed a bimodal distribution of pores at all of the heights examined except 5 mm from the chill. The bimodal distribution contained a population of pores of large equivalent radii and a second population of small radii, with few found in the intermediate size range.

The increase of pore size and volume fraction with initial hydrogen content and the spherical shape of the pores suggest microporosity in these castings is hydrogen induced. The increase of pore size and volume fraction with decreasing cooling rate is consistent with more time available for hydrogen to diffuse from liquid into the pores so that they grow on average to a large size. The results from this chapter will be used in Chapter 5 to validate the model developed to predict hydrogen microporosity formation in A356 alloys.

5 Development of a Numerical Model for Prediction of Microporosity Formation in Aluminum Alloy Castings

The objective of this chapter is to develop a model capable of predicting the pore size distribution in A356 aluminum alloy castings. This requires the simulation of both the nucleation and growth kinetics of the pores during solidification. In this work, an empirically determined equation is used to describe the nucleation site distribution as a function of hydrogen supersaturation in the liquid phase. Instead of tracking nucleation and growth of individual pores as in previous studies [62, 63], this study uses a binning method to track the growth of a group of pores that have nucleated within a given range in supersaturation. This method efficiently reduces the computational expense of the simulation, especially for castings of large geometry. Due to the difficulty of directly observing pore nucleation, the veracity of the equation related to the kinetics of pore nucleation is assessed based on the final pore population. All simulations are compared to experimental data from XMT analysis, as discussed in Chapter 4. The results show that the model predictions for porosity fraction and for the large pore size population fit the experimentally derived data satisfactorily, indicating the potential value of applying this model in a practical setting.

5.1 Features of the microporosity model

The microporosity model uses a small sub-element with uniform temperature and pressure taken from within the domain of a larger thermal-fluid model of the casting

process under analysis (Figure 5.1). It consists of solid, liquid and gas phases. Within the element the mass of hydrogen is conserved, i.e., transfer of hydrogen in and out of the element by diffusion or advection is neglected. The evolution of solid fraction is obtained from experimental data published in previous work [158]. The effect of cooling rate on the evolution of solid fraction is considered to be small over the range of cooling conditions experienced in this work.

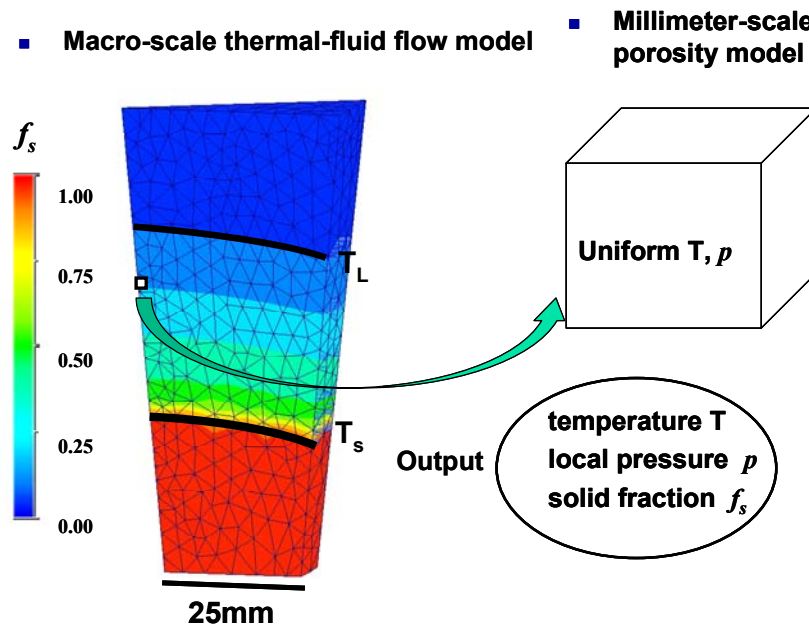


Figure 5.1: Schematic illustrating coupling of macro-scale thermal-fluid flow model with the millimeter-scale porosity model.

5.1.1 Thermal-fluid flow model

The transient solution of temperature and pressure within the larger domain (needed to provide the input to the sub-domain model) were obtained using a single-phase coupled thermal-fluid flow model with the Computational Fluid Dynamics (CFD) package Ansys-CFX, version 12.0. The thermal-fluid flow model was applied to a 3D domain with

symmetric boundary conditions as shown in Figure 5.1. The evolution of temperature during solidification was obtained by solving the equation of conservation of energy:

$$\frac{\partial \bar{\rho} C'_p T}{\partial t} + \nabla \cdot (\bar{\rho} C'_p u T) = \nabla \cdot (k \nabla T) \quad \text{Equation 5.1}$$

where T (K) is the temperature, u (m/s) is the velocity of the liquid phase and k (W/m/K) is the thermal conductivity .

In Equation 5.1, C'_p is the effective specific heat and is given by the following expression:

$$C'_p = C_p - \frac{\partial f_s}{\partial T} L_m \quad \text{Equation 5.2}$$

where C_p (J/kg/K) is the specific heat and L_m (J/kg) is the latent heat. Also, $\bar{\rho} = f_s \rho_s + f_l \rho_l$ (kg/m³) and is the density of solid-liquid mixture, f_s and f_l are volume fraction of solid and liquid phase, ρ_s and ρ_l are density of solid and liquid A356 alloy.

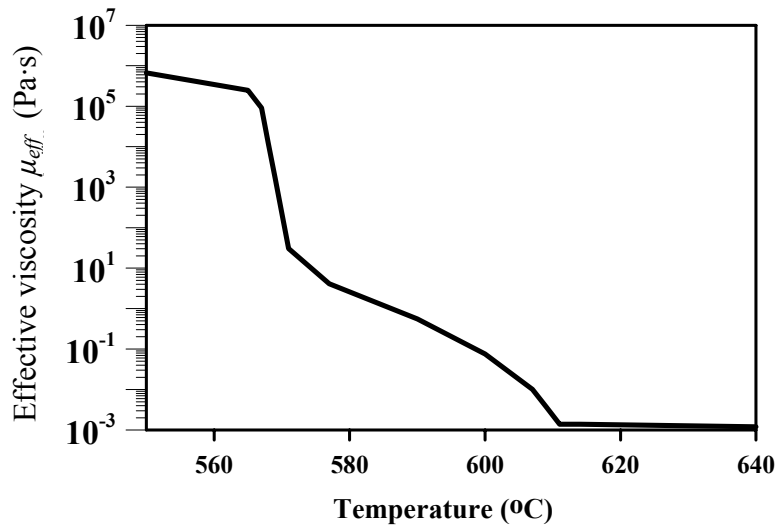
The key boundary conditions lie at the casting/chill and casting/mould interfaces and are of the Cauchy type. At the casting/chill and casting/mould interfaces the heat transfer coefficient is high at the beginning of the casting process and decreases as a gap is formed due to volume shrinkage of the casting during solidification. Through a process of comparison between the model predictions and the measured thermocouple data, the heat transfer coefficients at the cast/mold and cast/chill were gradually refined by trial-and-error to arrive at an optimal set of parameters that yielded the best fit to the empirical data.

To calculate the second term on the LHS of Equation 5.1 and to determine the pressure fields, the equations of conservation of mass and momentum were solved. As CFX only deals with fluid dynamics and does not distinguish solid and liquid phases, a continuum approach was used to solve the velocity and pressure fields within the

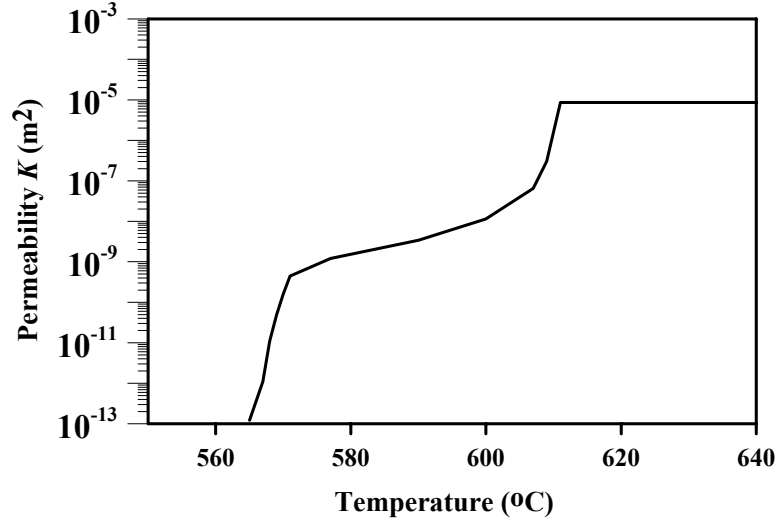
computational domain in the single-phase model. The same governing equation is used for solid, mushy and liquid zones - i.e. the solid-liquid zone is treated as one material with properties that change as a function of temperature to simulate behavior of the solid and liquid mixture. To account for the pressure drop associated with the flow of liquid in interdendritic channels, a source term is added to the RHS of the full Navier-Stokes equation. See the third term in

$$\frac{\partial \bar{\rho} u}{\partial t} + \nabla \cdot (\bar{\rho} u \times u) = -\nabla p + \nabla \cdot (\mu_{eff} \nabla u) - \frac{\mu_l}{K} u + \bar{\rho} g \quad \text{Equation 5.3}$$

where μ_l (Pa·s) is the viscosity of liquid. In Equation 5.3 μ_{eff} (Pa·s) is the effective viscosity of solid-liquid mixture [159] and K (m²) is the isotropic permeability calculated based on the modified Carman-Kozeny relation [152]. μ_{eff} and K are both functions of temperature as plotted in Figure 5.2. At temperatures between liquidus and solidus μ_{eff} is increased and K is decreased to gradually limit flow as solid fraction approaches 1. At temperature below solidus, μ_{eff} and K are set to completely suppress solid flow.



(a)



(b)

Figure 5.2: (a) Effective viscosity μ_{eff} [159] and (b) permeability K [152] as functions of temperature.

The solution of the momentum equation is accompanied by the solution of the continuity equation:

$$\frac{\partial \bar{\rho}}{\partial t} + \nabla \cdot (\rho_l u) = 0 \quad \text{Equation 5.4}$$

where ρ_l (kg/m³) is the density of liquid. The first term on the LHS of Equation 5.4 provides the driving force for the shrinkage compensation, which drives feeding through the mushy zone.

Table 5.1: Physical parameters in the thermal-fluid flow and microporosity model

Parameter	Physical property	Reference
k (W/m/K)	thermal conductivity	[160]
C_p (J/kg/K)	specific heat	[160]
D_H (m ² /s)	hydrogen diffusion coefficient in the liquid	[57]
K (m ²)	permeability	[152]
μ_{eff} (Pa·s)	effective viscosity	[159]
K_L (mol/m ³ /atm ^{1/2})	equilibrium constant in $[H] \leftrightarrow \frac{1}{2}H_2$	[106]
k	distribution coefficient of hydrogen (0.057)	[152]
ρ_l (kg/m ³)	density of liquid A356 alloy (2540 kg/m ³)	[152]
ρ_s (kg/m ³)	density of solid A356 alloy (2685 kg/m ³)	[152]
γ (N/m)	surface tension of A356 melt (0.79 N/m)	[152]
L_m (J/kg)	latent heat	[158]

5.1.2 Equilibrium condition

In this work, simulation of the pore formation is based upon the assumption that hydrogen activities within the pore and at the liquid/pore interface are in equilibrium, this requires the following relationship between the hydrogen concentration at the liquid/pore interface and the pore radius to hold [66, 70]:

$$C_{lp} = K_L \sqrt{p_a + p_h + \Delta p_d + \frac{2\gamma}{r_p}} \quad \text{Equation 5.5}$$

where C_{lp} (mol/m³) is the hydrogen concentration at the liquid/pore interface, K_L (mol/m³/atm^{1/2}) is the equilibrium constant for hydrogen solubility calculated based on composition of liquid A356 alloy, which is given as a function of temperature [106], p_a (Pa) is the atmospheric pressure, p_h (Pa) is the pressure of the metallic head described by ρgh , where ρ (kg/m³) is the density of the melt and h (m) is the distance from the top surface of the liquid metal, γ (N/m) is the surface tension of liquid aluminum and r_p (m) is pore radius. Δp_d (Pa) is the pressure drop due to Darcy flow within the mushy zone calculated from the thermal fluid flow model.

5.1.3 Pore nucleation

In this model, nucleation occurs continuously once the hydrogen concentration in the liquid reaches the critical value C_e , which is determined by the function:

$$C_e = K_L \sqrt{p_a + p_h + \Delta p_d} \quad \text{Equation 5.6}$$

The supersaturation, ss (mol/m^3), is the difference between the concentration of hydrogen in the liquid C_l (mol/m^3) and the critical hydrogen concentration, i.e.,

$$ss = C_l - C_e, \quad \text{Equation 5.7}$$

Previous work by Lee *et al.* on *in situ* observations of microporosity formation in an Al-7wt%Si melt undergoing directional solidification showed pores nucleating continuously over a range of temperatures throughout the solidification process [57, 59]. Furthermore, it was suggested that the increment in the number of nuclei formed with respect to a change in temperature could be described by a Gaussian function in temperature. Subsequent modeling work [63] found that the temperature dependency, for the alloy examined, corresponded to a supersaturation of hydrogen of 2.0 with a standard deviation of 0.5, where the supersaturation of hydrogen is defined as the ratio of the local hydrogen concentration to the solubility of hydrogen in the liquid. The mathematical formulation of a nucleation site distribution as a function of supersaturation was not given. The reader is referred to [63] for details about this model.

In the present study, the distribution of the heterogeneous nucleation sites for pore formation is simulated by introducing a Gaussian function based on the hydrogen supersaturation in the liquid phase:

$$\frac{dN_{nuc}}{dss} = \frac{A}{\sqrt{2\pi}\sigma} \exp\left(-\frac{(ss - ss_0)^2}{2\sigma^2}\right) \quad \text{Equation 5.8}$$

where N_{nuc} (mm^{-3}) is the number density of the nucleated pores, A (mm^{-3}), σ (mol/m^3) and ss_0 (mol/m^3) are adjustable parameters determined by fitting to the experimental results of pore volume fraction and size distribution. It should be noted that these three parameters, A , σ and ss_0 , represent a quantification of the pore nucleation kinetics. A is the total number of available nucleation sites provided by the inclusions in the melt. Hence it is possible to relate nucleation of the pores with metal cleanliness, which is an important factor in the foundry industry. ss_0 is the average hydrogen supersaturation required for pore nucleation and indicates the nucleation potency, i.e., how difficult it is for a gas cavity to form on solid substrates (oxide film defects) and is a measure of the mean thermodynamic driving force required to form a gas cavity in the melt. For example, the presence of solid inclusions that are not readily wetted by the melt - i.e. that serve as good heterogeneous nucleation sites for porosity within the melt- would reduce this number. σ is the standard deviation of the Gaussian distribution function. In the conventional heterogeneous nucleation theory (see 3.2.2), it represents the variability in the properties that affect nucleation potency such as geometry or composition of the solid substrates. In the bi-film entrainment theory (see 3.2.3) it represents the variability in hydrogen activity in the air trapped in the oxide films. Equation 5.8 is an improvement compared to the previous temperature based Gaussian distribution, as it provides a nucleation site distribution that only relates to the properties of the melt instead of depend on a series of casting conditions such as the initial hydrogen content and cooling rate.

The concentration of hydrogen in the liquid C_l can be calculated from mass conservation of hydrogen in the liquid as follows:

$$\Delta f_s \cdot C_l(1-k) \cdot V = \Delta(f_l \cdot C_l \cdot V) + \Delta \sum_i \left(\frac{N_{nuc} P_g V_g}{RT} \right)_i, \quad \text{Equation 5.9}$$

where V (m³) is the volume of the element, T (K) is temperature and R (J/mol/K) is the ideal gas constant and k is the distribution coefficient of hydrogen. In Equation 5.9, the left hand side is the amount of hydrogen released from the solid due to an increase in the solid fraction. This expression follows from the well known Scheil equation. The first term of right hand side is the increase of hydrogen in the liquid. The second term represents the amount of hydrogen inside the pore, after a pore has nucleated. N_{nuc} is obtained from integrating Equation 5.8 with an increment of hydrogen supersaturation. The sum is taken over all the temperature steps (indicated by i) at which pores nucleate.

5.1.4 Hydrogen diffusion controlled pore growth

Figure 5.3 shows the concentration profile in the vicinity of a growing pore and its surrounding diffusion boundary layer. The hydrogen rejected from the solid phase increases the concentration in the bulk liquid uniformly. This model assumes a linear concentration gradient approximation, as proposed earlier for simulating the diffusion-limited phase transformations [73]. The mass transfer rate of hydrogen through the boundary layer is then determined by the following relation [78, 161]:

$$\frac{dm_H}{dt} = \frac{D_l \cdot 4\pi r_p^2 \cdot \varphi \cdot (C_l - C_{lp})}{l_{diff}} \quad \text{Equation 5.10}$$

where m_H (mol) is the number of moles of hydrogen diffusing through the boundary layer, D_l (m²/s) is diffusivity of hydrogen in the liquid A356 alloy, r_p (m) is the radius of the growing pore, l_{diff} (m) is the thickness of the diffusion boundary layer approximated as the pore radius. The assumption that l_{diff} can be taken as r_p is based on analytical result for

the thickness of a quasi-steady species boundary layer around a sphere [78, 162]. This analysis assumes only diffusive transport and a semi-infinite domain. ϕ is an impingement factor, taken as $(1-f_s)^m$, f_s is the solid fraction and m is a parameter to be determined by fitting the predictions of the model with experimental data. The impingement factor accounts for the reduction of pore/liquid interface area as the solid fraction increases during solidification [20]. It considers the non-spherical nature of the pores and also the physical impingement of the pores on the solid microstructure with no explicit separation of the two effects. The hydrogen concentration at the liquid/pore interface C_{lp} can be calculated from Equation 5.5. The volume change of the pore can be obtained by the following equation according to the ideal gas law:

$$\Delta m_H = \left(\frac{p_g V_g}{R_g T}\right)^{t+\Delta t} - \left(\frac{p_g V_g}{R_g T}\right)^t \quad \text{Equation 5.11}$$

where,

$$p_g = p_a + p_h + \Delta p_d + \frac{2\gamma}{r_p}, \quad V_g = \frac{4}{3}\pi r_p^3 \quad \text{Equation 5.12}$$

$t(s)$ is the current time and $\Delta t(s)$ is time step size, 0.5s in the program. Therefore, by solving Equation 5.10 to Equation 5.12, the evolution of the pore radius with temperature is calculated. Combining with Equation 5.8, the porosity size distribution at the end of solidification can be predicted.

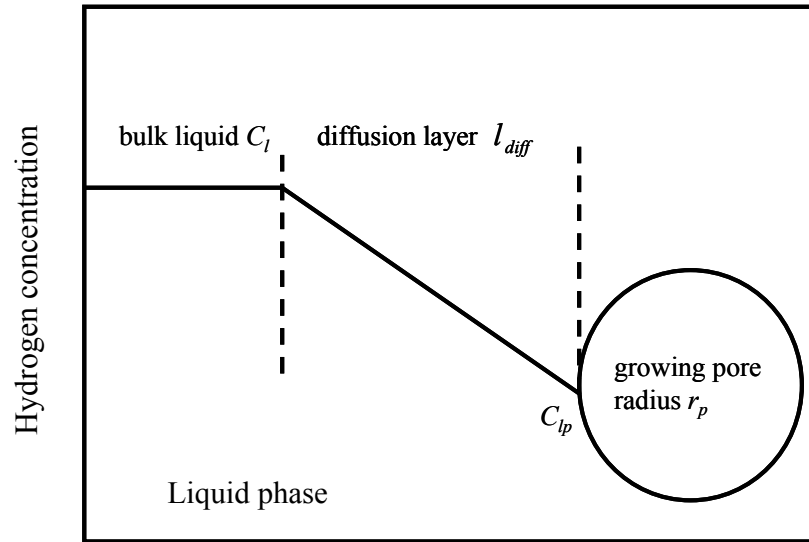


Figure 5.3: Schematic of a hydrogen diffusion boundary layer around a growing pore where the linear gradient approximation is applied.

5.1.5 Solution technique

A FORTRAN program has been developed to perform the calculations in the model. The temperature and pressure fields during the casting process are generated from a macro-scale thermal-fluid flow model with the Computational Fluid Dynamics (CFD) package Ansys-CFX, version 12.0. The timestep size used in the program is 0.02 second with 5 iterations in the coefficient loop. The output from the thermal-fluid flow model is input into the porosity model to predict the evolution of hydrogen concentration and porosity formation in a representative elementary volume of the material (typically in order of magnitude of mm^3 in scale), as shown in Figure 5.1. There is one-way coupling between the two models, i.e., the temperature and pressure fields are fed into the microporosity model. The influence of microporosity formation on thermal and fluid flow is assumed to be negligible under the conditions studied in this work. At each time step, the solid fraction f_s ($0 \leq f_s \leq 0.99$) in each element is determined first so that the liquid fraction and hydrogen concentration within the liquid can be obtained by Scheil equation.

Once the hydrogen concentration in the liquid exceeds the solubility limit, Equation 5.8 is integrated to get the number of nuclei that activated during the corresponding temperature increment. The pore radius is determined by solving Equation 5.11 using the Newton-Raphson method. Then the hydrogen concentration in the liquid is updated according to Equation 5.9. This concentration is then used in the next iteration to determine the hydrogen supersaturation in the liquid and thus the nucleation site distribution in Equation 5.8. Finally, the size of the pores and their number density at each temperature step can be calculated.

5.1.6 Novelty of the model

In previous work [58], the nucleation site distribution of the pores was formulated as Gaussian function of temperature. It was found that this temperature-dependent nucleation function varies under different cooling rates and therefore does not uniquely represent the property (e.g., composition and cleanliness) of the alloy material. In this work, the nucleation site distribution is for the first time formulated explicitly as a function of hydrogen supersaturation. By doing this, castings from the same melt can have a unique nucleation site distribution. This is because the effect of cooling rate on pore nucleation is linked directly to the hydrogen concentration. Once the pores have nucleated, the amount of hydrogen available to nucleate more pores is affected by two phenomena – release of hydrogen from solid to liquid phase due to solidification, and pore growth kinetics. The first is only temperature dependent and the second is strongly cooling rate dependent. These effects are considered by solving Equation 5.8, Equation 5.9 and Equation 5.10.

To improve the efficiency of the porosity model, the algorithm adopts an approach in which all of the nuclei that form within a user-specified increment in supersaturation, ΔS_{input} , are binned and treated as a group or population of nuclei, which will grow with a common radius. In this way, the Newton-Raphson solution steps, which consume the most computation time, are performed less frequently and thus the computational efficiency of the program is greatly improved. The size distribution is then given by accumulating the output pore population located within each size range that is specified according to the XMT analysis. Sensitivity analysis of the model to ΔS_{input} has been performed to determine an optimal ΔS_{input} , which ensures the highest computational efficiency and maintains accuracy.

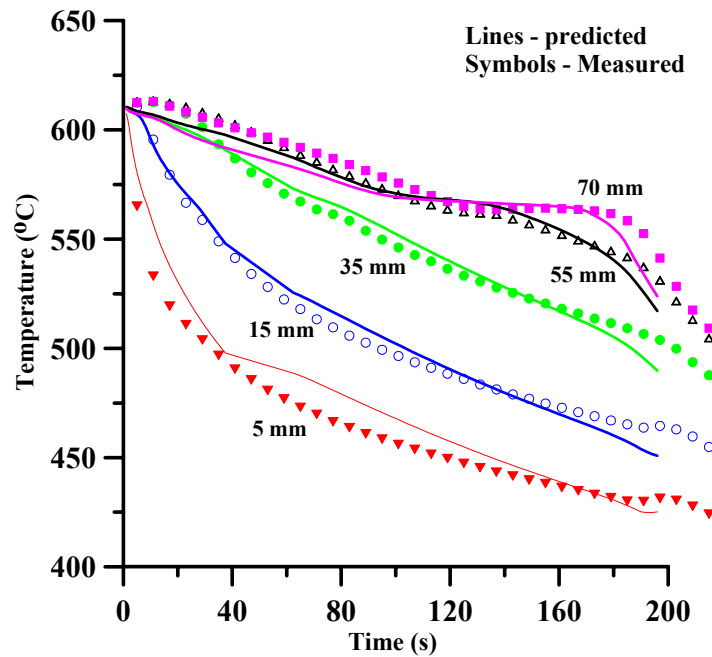
5.2 Results and discussions

In order to validate the microporosity model, the model predictions have been compared to thermal and porosity data obtained experimentally from the A356 tapered cylindrical castings as described in Chapter 4.

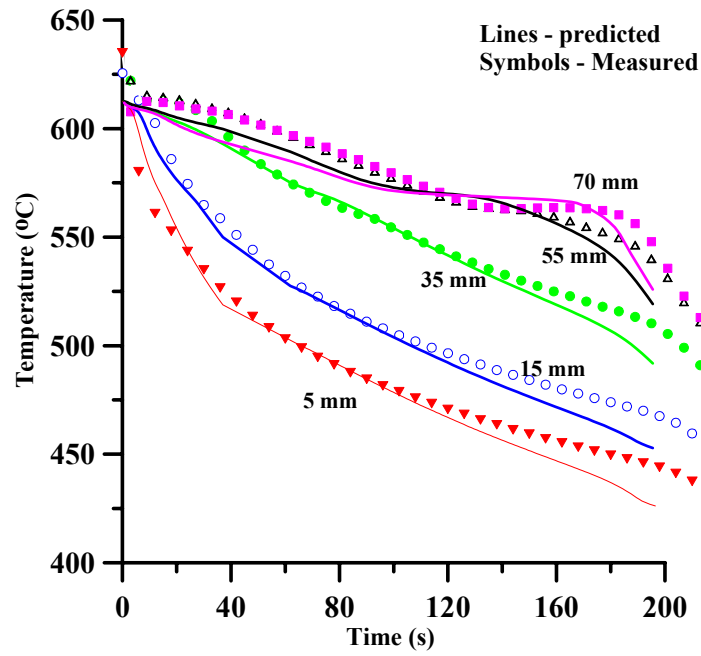
5.2.1 Validation of the thermal model

The thermal fluid-flow model was run to simulate solidification of the entire casting. The computation time was 5 hours with $2 \times 2.33\text{GHz}$ Intel Xeon quad-core CPU and 4.00GB RAM. Figure 5.4 shows the comparison between predicted and measured cooling curves for the five locations within the castings. As shown in this figure, through the process of aligning the thermal model to the thermocouple data and extracting various interfacial heat transfer coefficients, a satisfactory agreement is obtained. The discontinuity of the cooling curves at 5 mm from the chill is due to the formation of gap at the interface between the casting and chill at 37 s. The heat transfer coefficient drops

when the gap is formed, as shown in Figure 5.5. It is shown that for both samples, the solidification time increases from the bottom of the castings toward the top. The numerical solution of the mass and momentum conservation equations in the mushy zone provides a prediction of feeding behavior and hence the pressure drop. The local variation in pressure and temperature were then used to investigate the nucleation and growth behavior of hydrogen induced microporosity. The results showed that under the current experimental casting conditions the maximum pressure drop at all five locations is less than 10% of atmosphere pressure and thus has only a minor effect on microporosity formation. It is also shown that the average velocity of the liquid is in the scale of 10^{-5} m/s, adding to the veracity of the earlier assumption that the transfer of hydrogen due to advection is sufficiently small.



(a)



(b)

Figure 5.4: Comparison between the measured and predicted cooling curves at different distances from the chill for (a) 0.5-min degassed and (b) 1.0-min degassed samples.

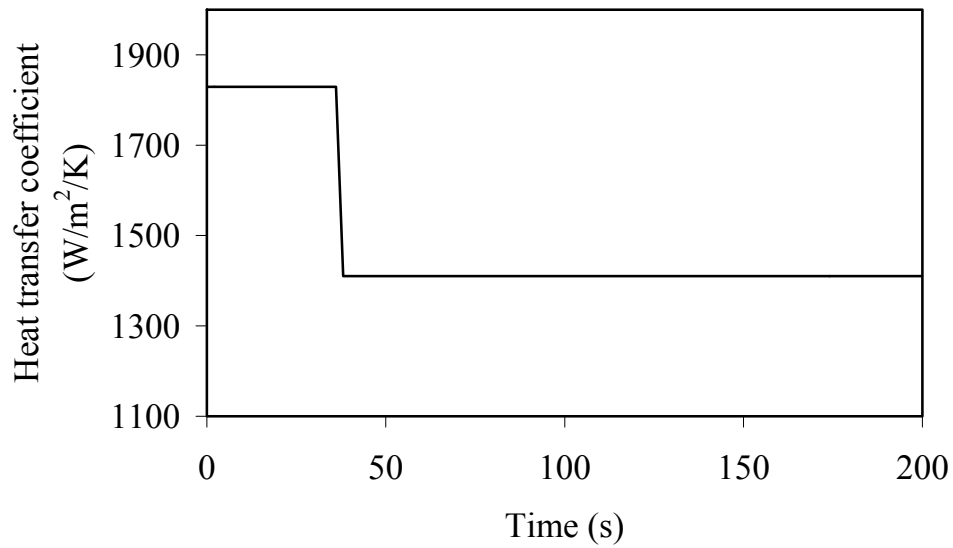


Figure 5.5: Heat transfer coefficient determined by fitting to the measured cooling curves using a trial-and-error approach.

5.2.2 Pore volume fraction

The model was run to simulate pore formation at each location in the 0.5-min and 1.0-min degassed samples. The 2.0-min degassed sample was not included, as it did not have a measurable volume fraction to be fitted by the porosity model. Once the macro-scale thermal-fluid computation was completed, the average computation time for the porosity model at each location required an additional ~100s for a PC with 2×2.13GHz CPU and 1.00GB RAM.

Figure 5.6 shows the XMT measurements and model predictions of pore volume fraction in the 0.5-min and 1.0-min degassed samples as a function of distance from the chill. As can be seen the volume fraction decreases with decreasing hydrogen content and increases, within a given casting, with decreasing cooling rate (increasing distance from the chill). In comparison to the measurements, the model correctly predicts both trends and is also quantitatively accurate in its predictions, apart from at the 70 mm location. It should be noted that at 70mm from the chill, which is near the top surface of the casting, there is a loss of liquid available to feed volumetric shrinkage due to the freezing over the top surface prior to complete solidification; therefore, the model would tend to under predict porosity formation unless shrinkage porosity is taken into account. To improve the fit at this location, the local pressure drop associated with formation of isolated liquid pockets and the pull in of the top surface would need to be calculated, which is beyond the scope of the current work.

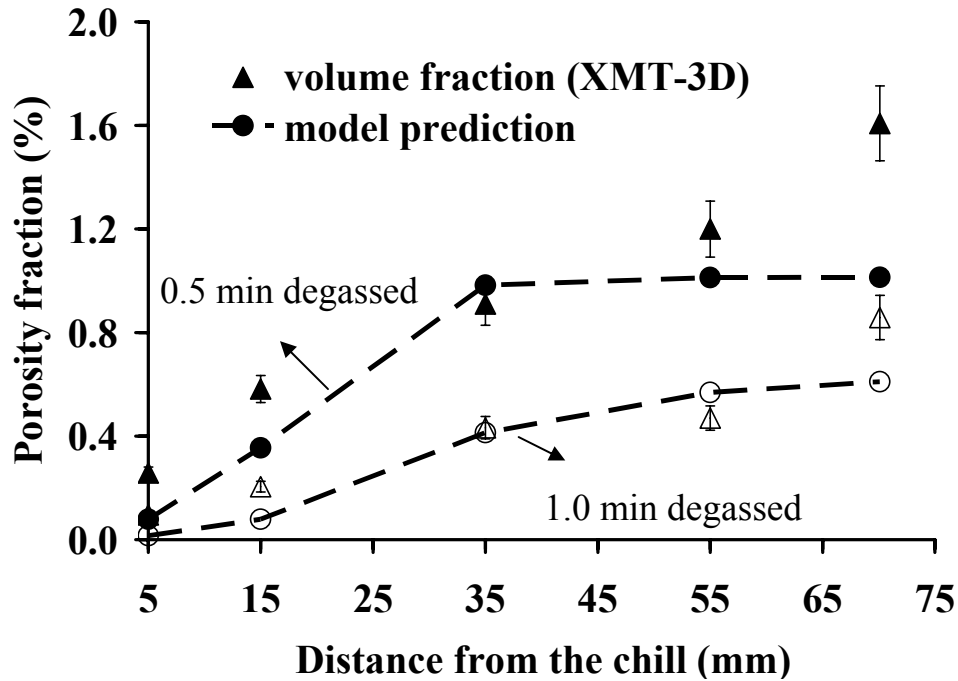


Figure 5.6: Comparison between predicted and measured variation in porosity fraction as a function of distance from the chill in the 0.5-min and 1.0-min degassed samples.

5.2.3 Pore size distribution

Figure 5.7 and Figure 5.8 show the corresponding size distribution analysis binned in 10 μm increments from the XMT analysis together with the predictions from the pore nucleation and growth model (the XMT data appear as the shaded bars and the model results as the open bars). Focusing first on the XMT data, a comparison between the two figures shows that the pore size decreases as the hydrogen content is reduced from 0.32 ppm (0.5-min degas time) to 0.20 ppm (1.0-min degas time) at a given distance from the chill. The hydrogen content was measured using a LECO RH-402 analyzer at Alcoa Primary Metals Division Laboratory (Frederick, MD) as described in Chapter 4. The results show that within a given casting, as the distance from the chill increases there is a shift to larger pores. It is worth noting that the binned XMT shows a fair degree of

variation in the number density between adjacent bins. This behavior is likely related to some degree to the relatively small volume scanned in the analysis, but also reflects the stochastic nature of the nucleation process. Note also that the pores with a size less than 20 μm have not been plotted (the small size range end of the bimodal distribution), as the pore nucleation and growth model does not account for the pressure drop and pore formation associated with liquid encapsulation at high solid fraction.

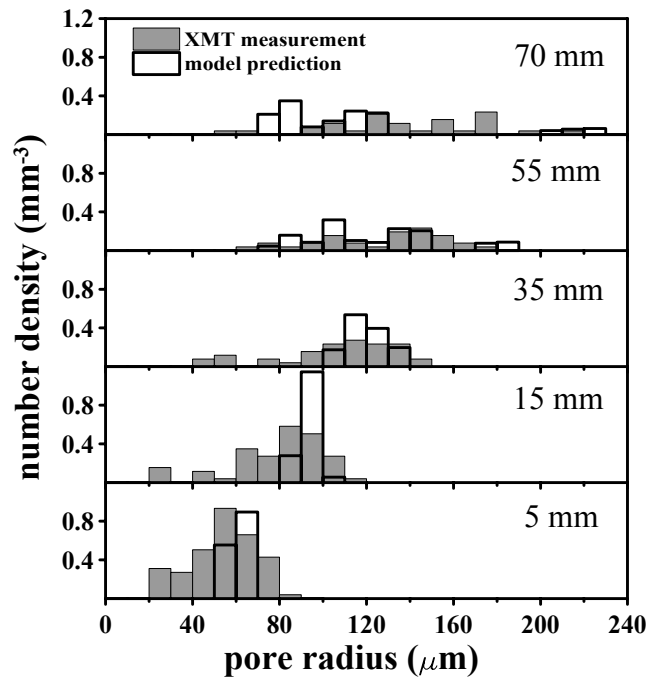


Figure 5.7: Comparison between measured and predicted pore size distribution at different distances from the chill in the 0.5-min degassed sample.

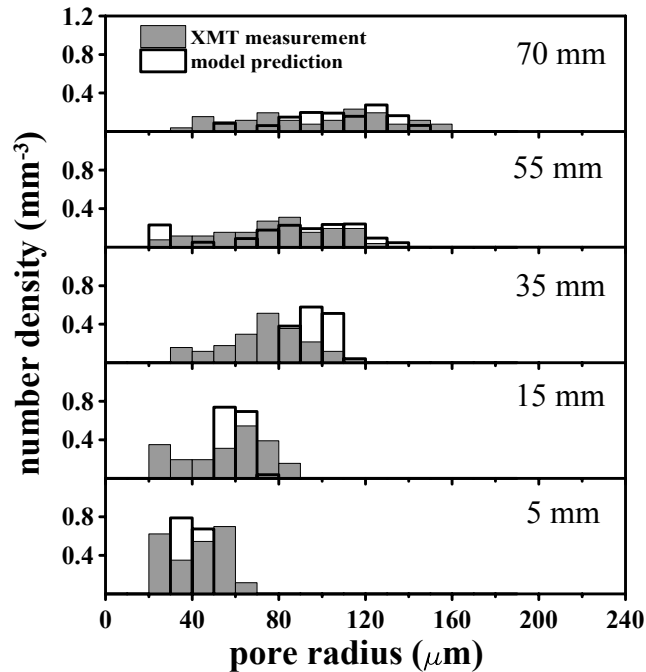


Figure 5.8: Comparison between measured and predicted pore size distribution at different distances from the chill in the 1.0-min degassed sample.

Turning to the model results (open bars), it can be seen that the model is able to accurately predict the correct trend in the measured data - e.g. there is a shift to smaller pores with increasing degassing time (decreasing hydrogen content) at a given height in the casting and with increasing distance from the chill (decreasing cooling rate). In terms of the effect of hydrogen content, decreasing the hydrogen content results in the critical supersaturation for pore nucleation being achieved at a larger fraction solid and therefore there is a smaller amount of time available for pore growth to occur. In terms of the effect of cooling rate, the trend to a smaller number density of large pores with decreasing cooling rate stems from the fact that there is a longer time period for mass transfer of hydrogen to occur (to the growing pores). Therefore, the nuclei formed via Equation 5.8 grow larger.

5.2.4 Determination of the fitting parameters

There are four parameters in the model that are determined by fitting with experimental results: A , σ and ss_0 in the nucleation kinetics equation (Equation 5.8), and m in the relationship quantifying the impingement factor φ . A trial and error approach was applied for each casting to arrive at a set of nucleation parameters that gave the best fit for the entire casting. In the initial application of the model to investigate the effect of degassing time on pore nucleation and growth kinetics a simple trial and error analysis proved sufficient to achieve good agreement between the model predictions and the experimental data. In a subsequent application of the model to investigate the effect of oxide film generation on pore nucleation kinetics a more complicated two-stage fitting approach was adopted which is described in Chapter 6.

The fitting parameter m was assumed to vary with cooling rate or more precisely with the scale of the cast microstructure. The variation that gave the best fit is shown in Figure 5.9, together with photomicrographs for the corresponding microstructure. The variation in m is consistent with a reduction in impingement with decreasing cooling rate (increasing dendrite arm spacing).

Application of the model revealed that it was necessary to alter ss_0 and σ in the nucleation distribution for the two castings (different degas times). Figure 5.10 shows the corresponding variation in number of active nuclei as a function of hydrogen supersaturation for the two degassing times together with the corresponding rate equations. The results of fitting the model to the measured data indicated that higher supersaturations are required to nucleate pores when the degassing time is increased from 0.5 to 1.0 min and that the nucleation sites are activated over a broader range of hydrogen

supersaturation - i.e., it was necessary to increase the mean supersaturation, ss_0 , from 0.6 to 1.7 mol/m³ and the variance, σ , from 0.1 to 0.7 mol/m³. This effect is believed to be due to the ability of the rotary degassing process to remove oxide inclusions within the melt, which are potent nucleation sites for pore nucleation [35]. Previous work has shown that the degassing process is capable of removing (floating) oxide inclusions [89, 90, 97]. In contrast to the fitting parameters used in the expression for the nucleation kinetics, a single cooling rate dependent function for m (Figure 5.9) was suitable for both castings.

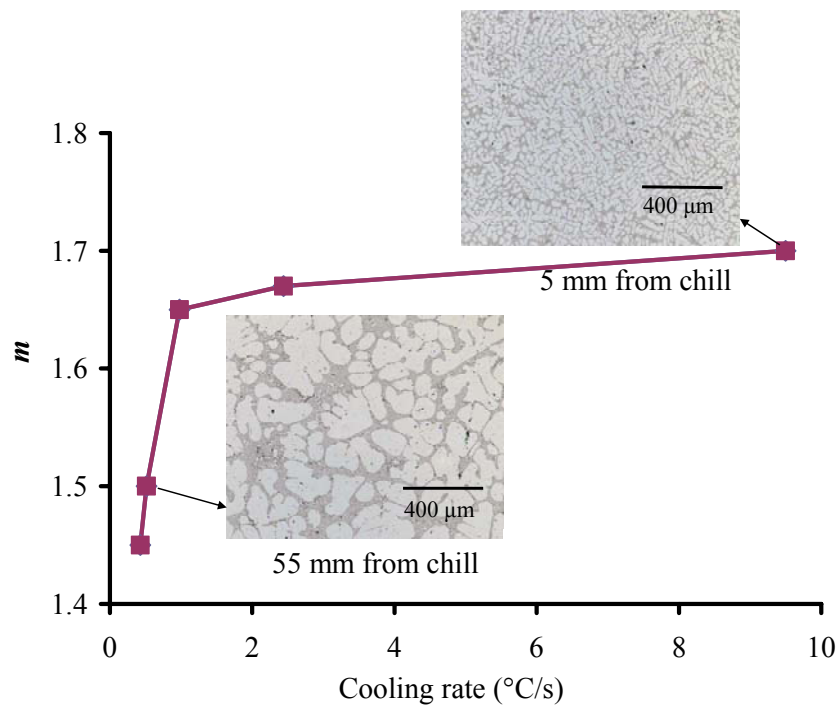


Figure 5.9: m in the impingement factor as a function of cooling rate derived by fitting the model predictions with experimental measurement.

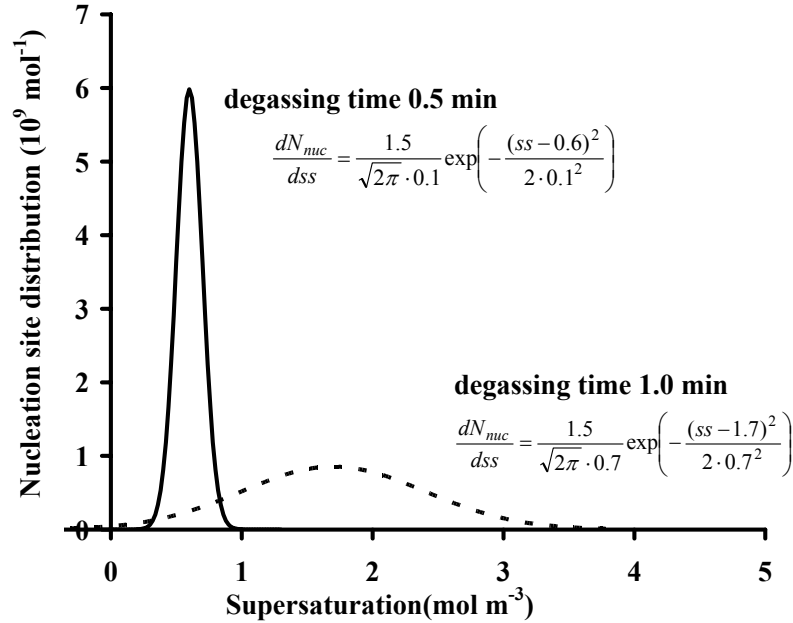


Figure 5.10: Pore nucleation site distribution at different degassing time derived by fitting the model predictions with experimental measurement.

5.3 Numerical model analysis

5.3.1 Sensitivity of the model to initial pore radius (r_0)

In this model, the initial pore radius r_0 determines the equilibrium hydrogen concentration (Equation 5.5) and the mass transfer rate of hydrogen (Equation 5.10) in the first iteration of the diffusion process. Due to a lack of direct experimental observations, most previously published work assumes an initial pore radius within the range of 1 to 10 μm for the nucleated pores [41]. In the current work, a value of 5 μm was assumed and was adopted as the base-case for the purpose of conducting the sensitivity analysis. The sensitivity analysis constituted varying the initial pore radii between 1 and 10 μm , and comparing the predictions with the results for the base-case. The model results (output) used for the comparison included: the volume fraction porosity, f_p ; the average pore radius, r_{avg} ; and the maximum pore radius, r_{max} . The results are plotted in

Figure 5.11 and summarized in Table 5.2 as a percentage change resulting from the prescribed perturbation of the input parameter.

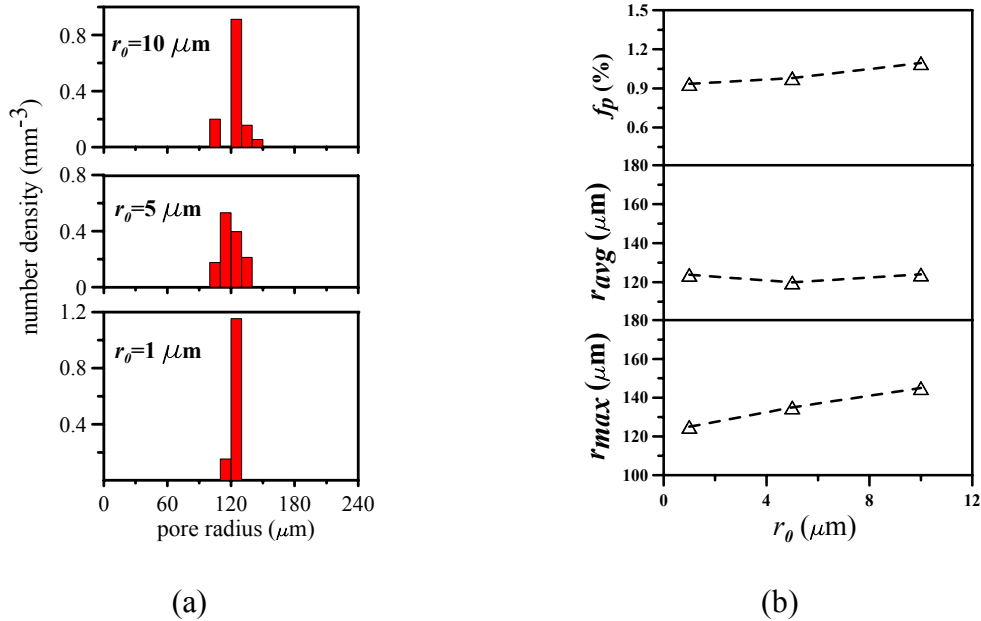


Figure 5.11: Sensitivity of (a) pore size distribution, (b) pore volume fraction, average and maximum pore radius to initial pore radius.

The results shown in Figure 5.11 indicate only a moderate sensitivity to this parameter. The trend shows an increase in the volume fraction porosity f_p and the maximum pore radius r_{max} , with increasing initial pore radius; whereas, there is no clear trend with respect to average pore radius, r_{avg} . Turning to the summary presented in Table 5.2, decreasing the initial pore radius from 5 to 1 μm results in a 4% decrease in f_p , 3% increase in r_{avg} and a 7% decrease in r_{max} . Increasing the pore radius from 5 to 10 μm results in a 12% increase in f_p , a 3% increase in r_{avg} and a 7% increase in r_{max} . Mechanistically, smaller pore radii require a higher hydrogen supersaturation to initiate hydrogen diffusion (Equation 5.5). This condition has a greater effect at the earlier stage of solidification when the concentration of hydrogen in the liquid C_l is small. Therefore,

those pores nucleated during the early stages of solidification, which end up as the large pores, are affected. Furthermore, as the large pores dominate the volume fraction of porosity, the effect on r_{max} and f_p is similar.

5.3.2 The sensitivity to A , ss_0 and σ

An analysis was also undertaken to characterize the sensitivity of the model predictions to the parameters A , ss_0 and σ used in the Gaussian nucleation site distribution function. For the base-case, values for the three parameters were: $A=1.5 \text{ mm}^{-3}$, $ss_0 = 0.6 \text{ mol/m}^3$ and $\sigma = 0.1 \text{ mol/m}^3$ (these values yielded a good fit to the experimental data in the 0.5-min degassed sample, 35 mm from the chill). Each analysis was performed by fixing two of the three parameters and adjusting the third. The assessment was on the basis of the three output parameters, f_p , r_{avg} and r_{max} previously used. The results are presented graphically in Figure 5.12 to Figure 5.14 and summarized numerically in Table 5.2.

Figure 5.12(a) shows the sensitivity of the pore size distribution to parameter A . It is shown that when A is increased from 0.75 to 2.25 mm^{-3} , the number density in each group is increased while the maximum pore size is not significantly affected. Turning to Figure 5.12(b), the trend for parameter A , which represents the maximum number of nuclei per unit volume in the melt, indicates an increase in f_p and a decrease in r_{avg} and r_{max} with increasing A . Clearly adding more nucleation sites per unit volume increases the volume fraction, but decreases the average and maximum radius of the pores. Quantitatively, as summarized in Table 5.2, reducing A from 1.5 mm^{-3} to 0.75 mm^{-3} results in a 31% decrease in the volume fraction porosity, a 13% increase in the average pore radius and a 7% increase in the maximum pore radius. Whereas, increasing A from

1.5 mm⁻³ to 2.25 mm⁻³ results in a 26% increase in the volume fraction porosity, a 5% decrease in the average pore radius and a 7% decrease in the maximum pore radius.

Table 5.2: Sensitivity of pore volume fraction f_p , average pore radius r_{avg} and maximum pore radius r_{max} to different parameters in the model.

Range Parameter	f_p		r_{avg}		r_{max}	
	lower	upper	lower	upper	lower	upper
r_0 (μm)	-4 %	12%	3%	3.41%	-7%	7%
A (mm^{-3})	-31%	26%	13%	-5.11%	7%	-7%
ss_0 (mol/m^3)	36%	-4%	11%	-1.27%	7%	-7%
σ (mol/m^3)	3%	8%	-1%	0.45%	-7%	22%
m	8%	-64%	6%	-28.82%	30%	-30%
γ (N/m)	22%	-3%	9%	-0.94%	7%	0%

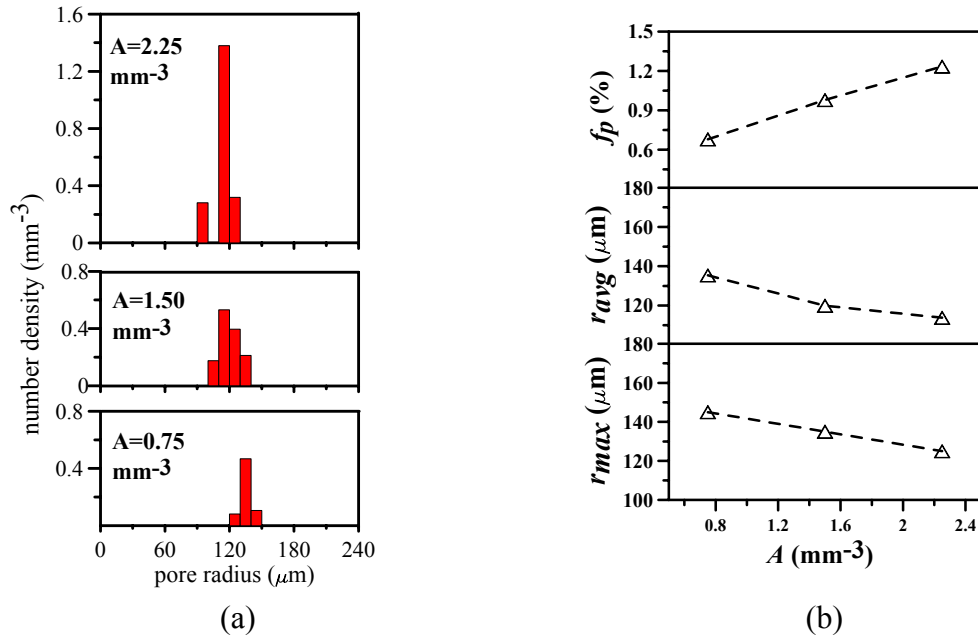


Figure 5.12: Sensitivity of (a) pore size distribution, (b) pore volume fraction, average and maximum pore radius to A .

For ss_0 , which represents the mean supersaturation required for pore nucleation, Figure 5.13(a) shows the sensitivity of the pore size distribution to ss_0 . With $ss_0=0.6 \text{ mol/m}^3$ as determined from fitting with experimental data, the pore size shows a near-normal distribution from 100 to 140 μm . When ss_0 is increased to 0.9 mol/m^3 , 2/3 of the pores end up in the 120 μm bin and the maximum pore size is 130 μm ; when ss_0 is reduced to 0.3 mol m^{-3} , 2/3 of the pores were in the bin of the maximum pore size, 150 μm . The results show that smaller ss_0 causes a slight increase in the pore size, especially the number density in the maximum bin. Figure 5.13(b) shows a trend to decreasing f_p , r_{avg} and r_{max} with increasing saturation. Clearly as the potency of the nucleation sites is decreased so are f_p , r_{avg} and r_{max} . Referring to Table 5.2, reducing ss_0 from 0.6 mol/m^3 to 0.3 mol/m^3 results in a 36% increase in the volume fraction porosity, a 11% increase in

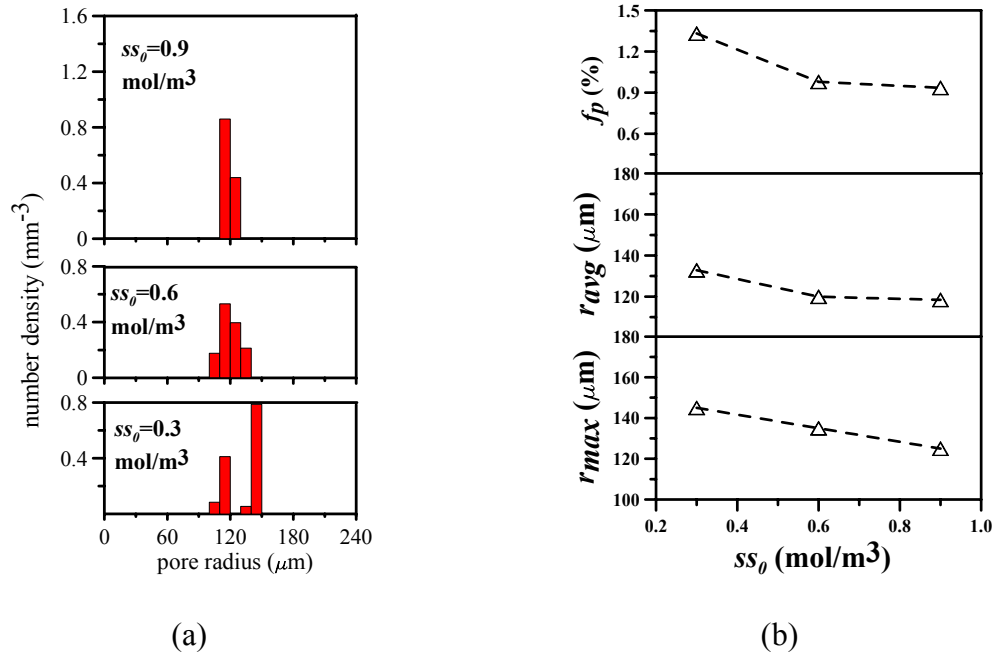


Figure 5.13: Sensitivity of (a) pore size distribution, (b) pore volume fraction, average and maximum pore radius to ss_0 .

the average pore radius and a 7% increase in the maximum pore radius. Whereas, increasing ss_0 from 0.6 mol/m^3 to 0.9 mol/m^3 results in a 4% decrease in the volume fraction porosity, a 1% decrease in the average pore radius and a 7% decrease in the maximum pore radius.

Figure 5.14(a) shows the sensitivity of the pore size distribution to σ , which represents the width of the nucleation site distribution. Compared with ss_0 , σ has a greater effect on pore size distribution. It determines the range of the bin sizes where the pores are distributed. When σ is 0.05 mol m^{-3} , the pores are located in only two bins, $120 \mu\text{m}$ and $130 \mu\text{m}$. When σ is increased to 0.15 the pores are distributed in bins from 110 to $170 \mu\text{m}$. Figure 5.14(b) shows little variation in f_p and r_{avg} , with σ , but a substantial increase in r_{max} with increasing range. Referring to Table 5.2, reducing σ from 0.10 mol/m^3 to 0.05 mol/m^3 results in a 7% decrease in the maximum pore radius. Whereas, increasing σ from 0.10 mol/m^3 to 0.15 mol/m^3 results in a 22% increase in the maximum pore radius.

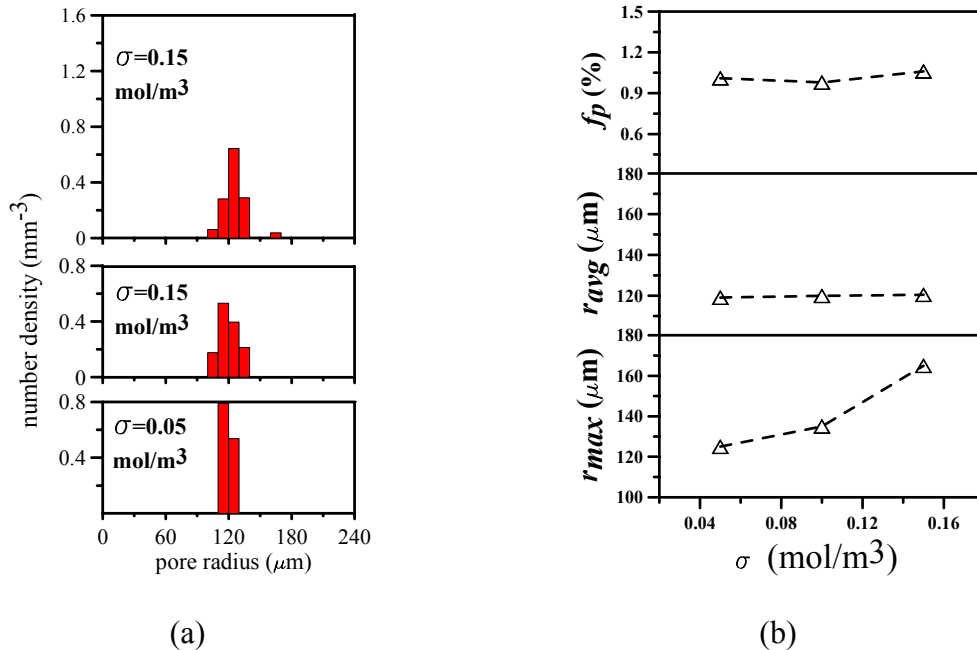


Figure 5.14: Sensitivity of (a) pore size distribution, (b) pore volume fraction, average and maximum pore radius to σ .

In summary, the number and potency of the heterogeneous nucleation population (as indicated by the values chosen for A and ss_0 , respectively) can have a large impact on the prediction of porosity in the current model (over a 20% increase in the predicted volume fraction associated with a 50% increase in A and a 50% decrease in ss_0). Additionally, large values of σ , allows for pore nucleation at low super-saturations leading to the formation of a few large pores, thus increasing r_{max} (over a 20% increase in the predicted maximum pore radius associated with a 50% increase in σ).

5.3.3 The sensitivity to m and γ

A sensitivity analysis was also undertaken to help characterize the importance of the impingement parameter m and the effect of surface tension term, γ , on microporosity formation. The results of these sensitivity analyses are shown graphically in Figure 5.15 and Figure 5.16 and are summarized numerically in Table 5.2.

Turning first to m , the exponential term on the impingement factor, increasing m in the expression for the impingement factor results in a greater degree of impingement (reduced mass transfer rate) at a given fraction solid as would be expected to occur with a finer microstructure (smaller secondary dendrite arm spacing). Figure 5.15(a) shows the sensitivity of pore size distribution to m in the impingement factor. It shows that when m is taken as 2.0, the pore size is binned within 80 and 100 μm ; when m is decreased to 1.0, the pore sizes are widely distributed from 30 to 180 μm . Figure 5.15(b) shows a trend to increasing f_p , r_{avg} and r_{max} with decreasing m . As seen in Table 5.2, all three model output parameters are strongly sensitive to m . For example decreasing m from 1.65 to 1.0 results in a 8% increase in the volume fraction porosity, a 6% increase in the average pore radius and a 30% increase in the maximum pore radius. Whereas, increasing m from 1.65 to 2.0

results in a 64% decrease in the volume fraction porosity, a 29% decrease in the average pore radius and a 30% decrease in the maximum pore radius.

Turning to the surface tension, three different surface tensions were used to examine its effect on porosity formation. The base-case surface tension was that of unmodified A356 alloy $\gamma_{A356} = 0.79$ N/m [119]; the other two were taken as 0.395 N/m and 1.185 N/m, respectively. The surface tension of Sr-modified A356 alloy $\gamma_{Sr-A356} = 0.64$ N/m is within this range.

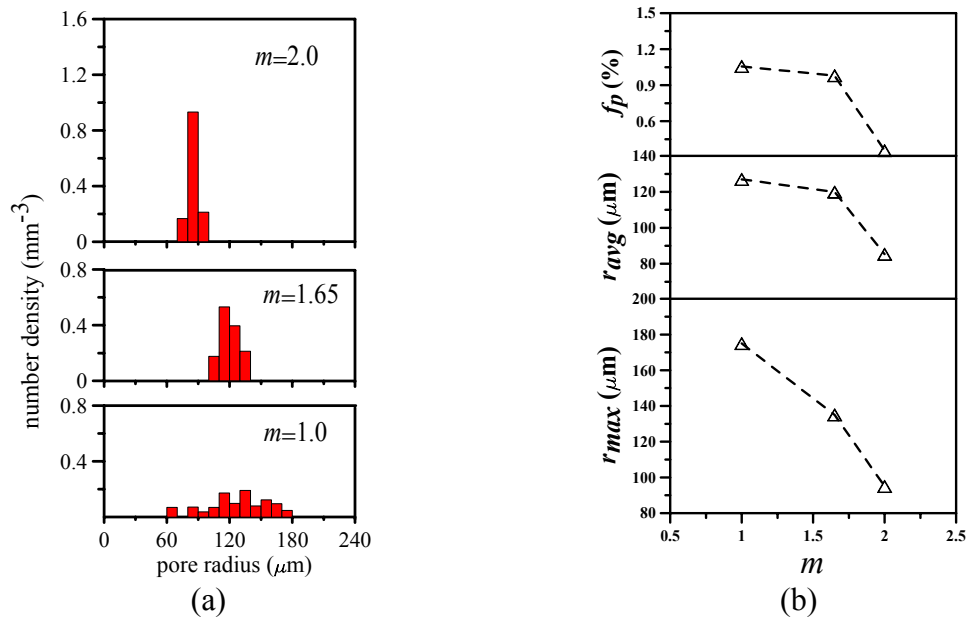


Figure 5.15: Sensitivity of (a) pore size distribution, (b) pore volume fraction, average and maximum pore radius to m .

Figure 5.16(b) shows that the trend is to decrease f_p , r_{avg} and r_{max} with increasing surface tension. As seen in Table 5.2, decreasing γ from 0.79 N/m to 0.395 N/m results in a 22% increase in the volume fraction porosity, a 9% increase in the average pore radius and a 7% increase in the maximum pore radius. Whereas, increasing γ from 0.79 N/m to

1.185 N/m results in a 3% decrease in the volume fraction porosity, a 1% decrease in the average pore radius and no change in the maximum pore radius.

In the context of the current model, the observed trend can be explained by considering the impact of surface tension on the hydrogen concentration at the interface which is related to the pore radius (and surface tension) via the Gibbs-Thomson curvature effect - refer to Equation 5.5. A smaller γ results in a lower equilibrium hydrogen concentration at the interface, which increases the hydrogen concentration gradient in the diffusion layer. The increased hydrogen concentration gradient provides a greater driving force for hydrogen diffusion and thus yields a higher pore growth rate. Second, from Equation 5.12 it can be deduced that a smaller γ results in a lower internal pressure within the pore so that a greater volume increment can be achieved for a given amount of hydrogen transported to the pore.

However, it should be noted that based on previous work the enhanced pore formation due to Sr modification [108] is not simply a result of decreased surface tension. As pointed out by Campbell *et al.*[163, 164], changes in hydrogen content, freezing range, nucleation potency, and oxidation rate are all possible factors that increase porosity formation in the modified alloys. One should also add changes to permeability, as it would impact on the variation in the local pressure with fraction solid.

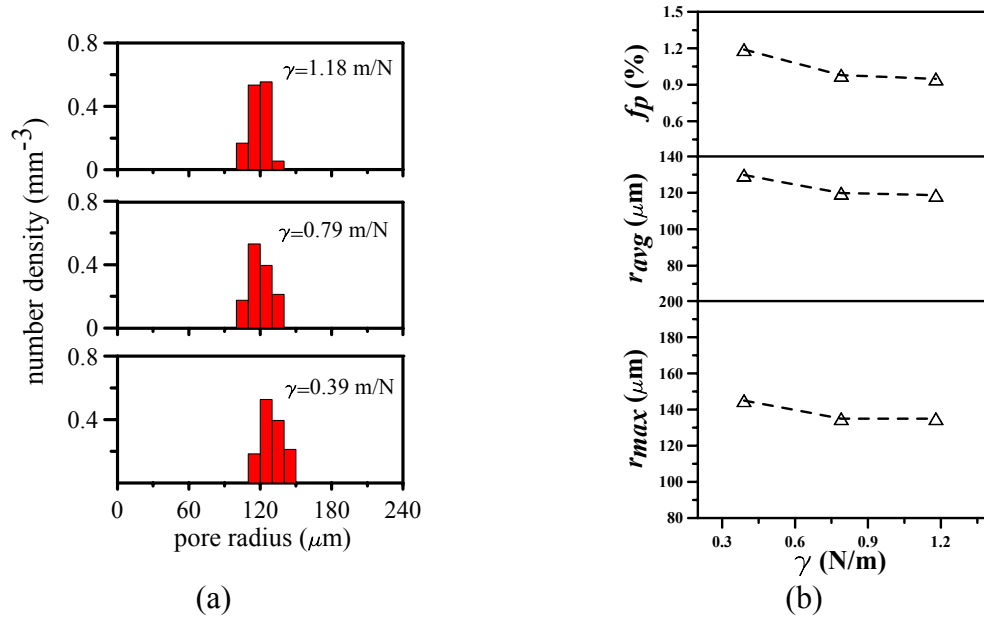


Figure 5.16: Sensitivity of (a) pore size distribution, (b) pore volume fraction, average and maximum pore radius to γ .

In summary, m in the impingement factor shows the largest impact on the prediction of porosity in the sensitivity analysis (over a 50% increase in the predicted volume fraction, over a 20% increase in the predicted average and maximum pore size associated with a 50% decrease in m). The sensitivity to surface tension is relatively small (a 22% increase in the predicted volume fraction associated with a 50% decrease in γ).

5.3.4 The effect of the cooling rate

Previous experimental work has reported that the porosity fraction increases as cooling rate decreases in aluminum alloy castings [34, 37, 57, 60, 79-86]. In the formulation of the model the effect of cooling rate is accounted for in two ways: first, a lower cooling rate results in a lower solidification rate and therefore more time for hydrogen to diffuse from the liquid into the pores so that they grow to a large size, as pointed out in [57, 78]; and second, the lower cooling rate produces a coarser solid microstructure, which delays

pore/solid impingement resulting in increase mass transfer and larger pores. In the context of the impingement factor, $\varphi=(1-f_s)^m$, a smaller m gives a larger impingement factor at a given solid fraction and thus increases the effective area of the pore-liquid interface promoting formation of larger pores in conjunction with coarser microstructures.

5.3.5 The effect of the initial hydrogen content

The initial hydrogen content is a crucial factor influencing microporosity formation. Increased hydrogen levels result in a higher hydrogen concentration in the liquid during solidification, so that the pore nucleation starts at an earlier stage (lower fraction solid). This effect is considered in the model within Equation 5.9. Also the higher hydrogen content in the bulk generates a higher hydrogen concentration gradient in the diffusion layer, and thus a greater hydrogen mass transfer rate from the liquid into the pore, as can be seen by inspecting Equation 5.10. Good agreement between the model predictions and XMT porosity analysis of the 0.5-min and 1.0-min degassed samples indicates that the model can accurately predict the effect of initial hydrogen content on porosity formation. It should be noted that the lower hydrogen content in this work is a result of longer degassing time, which is known to also affect the solid inclusions in the melt. According to model predictions, longer degassing time removed the potent nucleation sites and thus delayed pore nucleation. This effect further reduced porosity formation in addition to removal of hydrogen from the melt. Thus there is a dual effect of degassing: 1) the hydrogen content is reduced; and 2) the number of heterogeneous nucleation sites is reduced.

5.4 Summary and conclusions

A microporosity simulation model predicting both the porosity volume fraction and the pore size distribution has been developed. The heterogeneous nucleation site distribution has been simulated as a Gaussian function of hydrogen supersaturation in the melt and that once nucleated, pore growth is controlled by hydrogen diffusion. The model formulation uses a binning method to calculate and track the growth of groups (bins) of pores that have nucleated within a user specified range of supersaturation. The main inputs to the model are the evolution in temperature with time and the evolution of pressure with time at the point of interest in the casting. Both can be estimated using a conventional thermal-fluid continuum model that is run decoupled from the pore nucleation and growth model. The approach is computationally efficient and has the potential to be applied to an industrial casting.

Validation of the model was performed with data generated from an XMT analysis of two tapered cylinder castings that had been degassed to different extents. The experimental results show that the porosity volume fraction and pore size increase with initial hydrogen content and with decreasing cooling rate. It has been shown that the model satisfactorily predicts both the size distribution and the total volume fraction in these tapered cylinder castings. The model is sufficiently complex in its formulation that the role of various factors in pore formation can be examined. For example, analysis of the two castings revealed a dependence of the heterogeneous nucleation population on degassing time. Degassing acts to both reduce the hydrogen in solution available for pore nucleation and growth, but it also reduces the tendency to nucleate pores by removing oxide inclusions in the melt. An additional finding of the work is the strong dependence

of the pore growth kinetics on pore/solid impingement. The later being a function of scale of the microstructure, which in turn is dependent on cooling rate.

6 Factors Affecting Nucleation Kinetics of Microporosity Formation in A356 Aluminum Alloy Castings

Metal cleanliness is one of the most critical parameters affecting microporosity formation in aluminum alloy castings. It is generally acknowledged that oxide inclusions in the melt promote microporosity formation by facilitating pore nucleation. The main objective of this chapter is to study the effect of oxide content on microporosity formation in A356 aluminum alloy castings. The focus is on the oxide films formed during the pouring process as studies have shown that pouring results in the largest free surface area during a gravity casting process [165]. The approach involves estimating the pore nucleation site distribution by fitting the pore size distribution, which is predicted by the microporosity model developed in Chapter 5, to data obtained from a series of experimental castings in which the pouring conditions were varied. The results are discussed in terms of nucleation number (related with number of oxides) and nucleation potency (indicated by the supersaturation necessary for pore nucleation). In addition to oxide films, the effect of Sr modification on microporosity nucleation is also discussed.

6.1 Experimental method

In this study the microporosity formation under different casting conditions, which were selected to manipulate the tendency to form and entrain oxide films in small directionally cast A356 samples was investigated. Castings were prepared with and without the aid of argon gas shielding and with a varying pour surface area. Two alloy variants of A356 were tested in which the main difference was Sr content. Porous disc

filtration analysis (PoDFA) was used to assess the melt cleanliness and identify the inclusions in the castings. The porosity volume fraction and size distribution were measured using X-ray micro-tomography (XMT) analysis.

6.1.1 Casting procedures

A series of experimental castings of A356 alloy were directionally solidified in a tapered, cylindrical refractory ceramic mold against a water-cooled copper chill. A detailed description and schematic of the mould assembly and configuration can be found in Chapter 4. To ensure the cooling conditions for each casting were correctly simulated in the thermal fluid flow model, the evolution of temperature with time was measured with three K-type thermocouples positioned within the mold at 10, 30 and 50 mm from the chill, as shown in Figure 6.1. To assess the effect of the hydrogen content, Ransley samples were again casted, machined and analyzed using the LECO vacuum fusion technique, which can determine the hydrogen content to within 0.01 ppm (cc/100 g-Al). In order to vary the oxide film content, three pouring methods were applied: 1) Ar-shielded pouring to obtain a low oxide film content; 2) normal-pouring to yield a medium or base oxide film content; and 3) increased surface area pouring to obtain a high oxide film content. Two sets of castings were completed: the first was undertaken at a local foundry (LF) and the second was carried out at the University of British Columbia (UBC). The casting conditions for the four tests are summarized in Table 6.1.

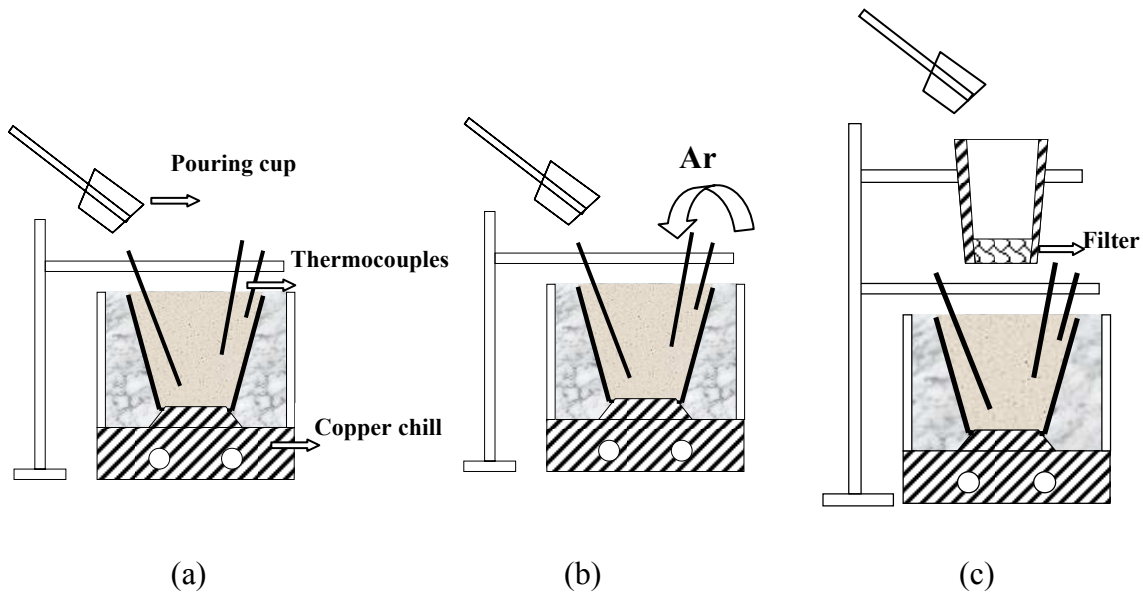


Figure 6.1: Schematic of the experiment setup for (a) normal pouring (NP), (b) Ar shielded pouring (ArP) and (c) high surface area pouring (HSAP) conditions.

Table 6.1: Description of casting conditions

Code Condition	LF-NP	LF-ArP	UBC-NP	UBC-HSAP
Metal sources	Alcoa	Alcoa	Alcan	Alcan
Ar shielding	No	Yes	No	No
Pour surface area	Normal	Normal	Normal	High

Effect of Ar shielding - Referring to Table 6.1, in the LF-NP test the melt was directly poured into the mould as shown in Figure 6.1(a) and in the LF-ArP test Ar gas was introduced into the mould cavity before and during pouring as shown in Figure 6.1(b) to reduce oxidation and thus the oxide film content within the melt (the pouring conditions were otherwise identical and therefore the tendency to entrain oxide films would be dependent only on their tendency to be generated during pouring). The A356 aluminum alloy used in this series of tests was heated and melted in a commercial reverberatory

furnace using ingots from Alcoa as the primary source for the melt stock with some addition of process scrap. Once melted, the alloy was poured into a ladle and Al-15wt% Sr alloy was added for modification. A boron nitride coated steel pouring cup was used to transfer the prepared melt from the ladle into the mould. The pour temperature was approximately 710 °C. The results from composition analysis are shown in Table 6.2 (LF).

Effect of high surface area pouring - In the UBC-NP test the melt was directly poured into the mould as shown in Figure 6.1(a) and in the UBC-HSAP test the melt was poured into a coarse 20 ppi reticulated foam filter installed above the mould (unsaturated filtration), as shown in Figure 6.1(c). The filter acted to break the melt into multiple streams thereby increasing the surface area of the liquid exposed to oxidation (there was likely some reduction in pour stream momentum associated with the filtered pouring that could reduce oxide film entrainment despite the increased tendency for their generation). In this second casting campaign, the melt feedstock was sourced from Rio Tinto Alcan. The melt was prepared in the Advanced Materials and Process Engineering Laboratory at UBC. The procedure involved melting 0.7 kg of A356 ingot in a graphite crucible using a lab-scale electric resistance furnace set at 800 °C. Once a steady state temperature was achieved, 0.5 g of Al-15wt%Sr alloy was added to the melt in an attempt to achieve 0.01wt% Sr, and the melt allowed a further 10 minutes for homogenization. The melt's surface was skimmed to remove the accumulated dross and then poured at ~750 °C. The chemical composition of the cast samples from this second campaign is shown in Table 2 (UBC).

Table 6.2: Chemical composition analysis for A356 aluminum alloy samples cast at local foundry (LF) and UBC (weight percentage)

	Si	Mg	Fe	Ti	Na	Sr	Ni	Cu	Al
LF	6.9800	0.3400	0.1500	0.1300	0.0027	0.0092	0.0070	0.0070	bal.
UBC	7.4900	0.3800	0.1000	0.1000	0.0007	0.0030	0.0000	0.0110	bal.

6.1.2 Inclusion analysis

To attempt to assess melt cleanliness, porous disc filtration analysis (PoDFA) samples were taken using identical pouring conditions to each test casting to measure the type and content of inclusions. The PoDFA trials were taken following the instructions [166] established by BOMEM Inc., Quebec, Canada – i.e. 1 kg of melt was poured into a crucible and forced to flow through a fine filter under pressure. During filtration, a cake of concentrated impurities and particulates from the melt built up on the filter. The residual metal, the inclusion cake and the filter formed the PoDFA sample which was analyzed using standard metallographic procedures by Arvida Research and Development Centre (ARDC) at Rio Tinto Alcan Limited, Jonquiere, Quebec, Canada. The types of inclusions present were identified using an optical and/or SEM microscope by comparison with documented images of example inclusions based on their morphological and chemical characteristics. The total area of each type of inclusion was measured using the grid method and divided by the total mass of the filtered melt to calculate the inclusion content. The results were given in the unit of mm^2/kg .

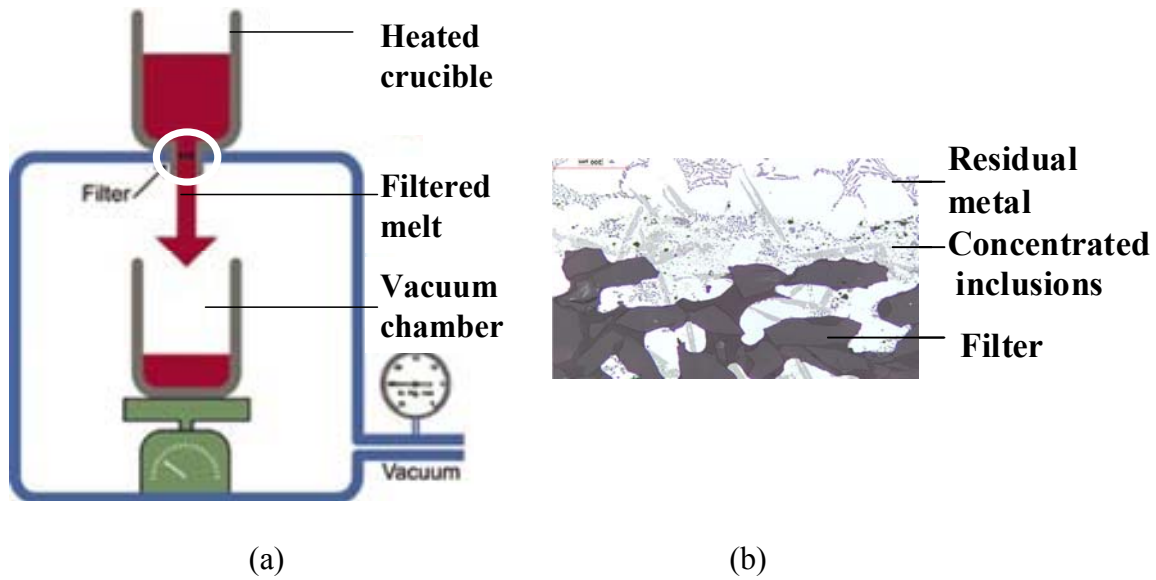


Figure 6.2: (a) Schematic showing the principle of the porous disc filtration apparatus (PoDFA) and (b) a PoDFA sample showing the layer of residual metal, the concentrated inclusions and the filter[166].

6.1.3 X-ray micro-tomography (XMT) analysis

The volume fraction and size distribution of the porosity in each casting were measured using 3-D X-ray micro-tomography (XMT), which was conducted on the TOMCAT beamline at the Swiss Light Source (SLS), Paul Scherrer-Institute, Villigen, Switzerland. The tomography data were acquired by applying a beam energy of 27 keV and a resolution of 3.7 μm . Three scans were performed on each casting sample at 10, 30 and 50 mm from the chill, corresponding to where the thermocouples were positioned. Each scan was comprised of 500 slices with a diameter of 3 mm and a volume of 13.1 mm^3 . Three-dimensional volumes of the pores were generated from these XMT data using the software ImageJTM and AMIRATM.

6.2 Fitting procedure

The pore nucleation and growth model developed in Chapter 5 was used to analyze the castings. As discussed previously, the model offers the potential to be able to quantify the dependence of nucleation kinetics on melt cleanliness/oxide content: the melt cleanliness may be inferred from the pore size distribution. One of the challenges in the bi-film theory proposed by Campbell has been that it is exceedingly difficult to observe, or measure by conventional means, oxide films directly owing to their exceedingly small scale [14, 38-40]. By obtaining the nucleation parameters under the different pouring conditions identified above, which are conducive to manipulate the tendency to form thin oxide films during pouring, it is possible to infer the effect of the melt oxide film content on pore nucleation kinetics. The comprehensive nature of the pore model takes into account the effect of the initial hydrogen content and the cooling rate leaving the dependence to be on the population of heterogeneous nucleation sites.

In terms of the three fitting parameters related to the nucleation kinetics, A is the total number of available nucleation sites, ss_0 is the mean hydrogen supersaturation required for pore nucleation and σ is the width of the nucleation site distribution. Taking for now a traditional approach to nucleation, ss_0 may be interpreted as the potency of the substrate (oxide) as a site for heterogeneous pore nucleation in the melt, which in turn may be related to the wettability of the substrate by the liquid. σ may be interpreted as the range in potency of the heterogeneous nucleation population.

To determine the optimum values for A , ss_0 and σ , a parameter R was defined to quantify the deviation of model prediction from experimental measurements. This parameter, representing an aggregate residual, was deemed necessary as there are various

quantities related to the pore size distribution that could potentially be employed to assess goodness-of-fit. Of the various quantities available, the integrated porosity volume fraction, f_p , maximum pore radius, r_{max} , the total number of pores in the maximum pore size bin, n_{rmax} and total number of pores, n_{total} were used. Both the XMT results and the results from the model are binned based on size range for plotting. Therefore, R is defined as the sum of the four residuals as follows:

$$R_{total} = R_{f_p} + R_{r_{max}} + R_{n_{rmax}} + R_{n_{total}} \quad \text{Equation 6.1}$$

where

$$\begin{aligned} R_{f_p} &= \sum_{i=1}^n \left(\frac{f_{cal}^p - f_{XMT}^p}{f_{XMT}^p} \right)^2, \\ R_{r_{max}} &= \sum_{i=1}^n \left(\frac{r_{cal}^{max} - r_{XMT}^{max}}{r_{XMT}^{max}} \right)^2, \\ R_{n_{rmax}} &= \sum_{i=1}^n \left(\frac{n_{cal}^{rmax} - n_{XMT}^{rmax}}{n_{XMT}^{rmax}} \right)^2, \\ R_{n_{total}} &= \sum_{i=1}^n \left(\frac{n_{cal}^{total} - n_{XMT}^{total}}{n_{XMT}^{total}} \right)^2. \end{aligned} \quad \text{Equation 6.2}$$

Additionally f_{cal}^p (-) and f_{XMT}^p (-) are the predicted and measured pore volume fractions respectively, r_{cal}^{max} (μm) and r_{XMT}^{max} (μm) are the predicted and measured maximum pore radii, n_{cal}^{rmax} (mm^{-3}) and n_{XMT}^{rmax} (mm^{-3}) are the predicted and measured total number of pores in the maximum pore size bin and n_{cal}^{total} (mm^{-3}) and n_{XMT}^{total} (mm^{-3}) are the predicted and measured total number of pores at each location within the casting. The individual residuals are summed $i=1 \sim n$, where n is the number of points in the casting where XMT data was obtained which is equal to 3 in the present work.

The procedure used to determine the fitting parameter m appearing in the impingement factor, φ , is described in Chapter 4. As m is dependent on the microstructure it is principally a function of alloy chemistry and cooling rate for a given alloy. In this chapter because two alloys were used it was necessary to employ two cooling rate dependent relationships for m , one for the LF-based tests that utilized an Alcoa alloy as the primary feedstock and a second for the UBC-based experiments that utilized a Rio Tinto Alcan alloy. Because the results are dependent on all three parameters m , A , ss_0 and σ , finding the optimum fit can be a challenge. To address this challenge a two-stage fitting procedure was adopted.

Coarse fitting - The purpose of coarse fit was to find an estimate of the fitting parameters for each casting. This was performed by calculating the contour map of residual R as a function of ss_0 and σ using a trial function for m of the form previously found in Chapter 5. Full integration of Equation 5.8 gives A , which is the total number of available nucleation sites. A can therefore be estimated from the XMT data, provided that during solidification the maximum hydrogen supersaturation reaches $ss_0+3\sigma$, which is assumed to occur near the chill (this assumption is based on the argument that the largest melt supersaturation is achieved in association with the largest cooling rates as there is limited time for hydrogen transport and pore growth to occur). A 2-D map of R was generated by inputting a series of ss_0 and σ values into the program, with an interval of 0.2 mol/m^3 and calculating the resultant residual R .

Finer fitting - Once an estimate for ss_0 and σ was found that had the potential to yield low residuals for a reasonable combination of A , ss_0 and σ , a trial and error approach was used for each casting to determine the optimum values for these three parameters based on the

results of the coarse fit. At this stage a visual assessment of the fit of the model predictions to the XMT measurements was also made.

6.3 Experimental results

6.3.1 Inclusion analysis based on PoDFA measurement

Table 6.3 shows the types and quantity (expressed in the unit of mm^2/kg) of the main inclusions identified through PoDFA analysis for both the Alcoa and Rio Tinto Alcan alloys under different pouring conditions. In addition to the inclusions shown in Table 6.3, traces of chlorides, MgO, graphite and refractory material were also observed. The PoDFA proved to be ineffective in quantifying the oxide film content in the base metals and any difference in the oxide film content amongst the various pouring methods used in the experiments. Possible explanations are that the oxide films formed during the pouring process are too small to be easily identified in the standard analysis of the inclusion cake and/or did not end up in the inclusion cake and instead passed through the PoDFA filter. One interesting observation from Table 6.3 is that from a comparison of the results it would appear that the filter used in the UBC high surface area pouring test was effective in reducing the Al_4C_3 , MgAl_2O_4 , $(\text{TiV})\text{B}_2$ and TiB_2/TiC contents.

Table 6.3: Results from PoDFA analysis showing major inclusions found in samples cast at local foundry (LF) and UBC.

Local Foundry (LF)		
Type	Normal Pouring (mm ² /kg)	Ar shielded Pouring (mm ² /kg)
Carbides Al ₄ C ₃ (≤ 3μm)	0.47	0.49
Carbides Al ₄ C ₃ (≥3μm)	0.86	0.49
UBC		
Type	Normal pouring (mm ² /kg)	High Surface Area Pouring (mm ² /kg)
Carbides Al ₄ C ₃ (≤ 3μm)	0.26	0.03
Spinel MgAl ₂ O ₄	0.22	Trace
(TiV)B ₂	0.06	Trace
TiB ₂ /TiC	1.46	0.79

To attempt to find evidence of oxide films some additional analysis of the inclusion cake was performed. Figure 6.3(a) and (b) show optical and SEM images, respectively, of what are believed to be oxide films in the PoDFA filter residue. The width of the film shown in Figure 6.3(b) is in the range of 1 - 3 μm. Figure 6.3(c) shows the results of an EDX analysis conducted at locations A and B in Figure 6.3(b). As can be seen the oxygen concentration in the vicinity of the film like structure, at location A, is approximately double that of the concentration in the matrix, at location B, suggesting that the structure may be an oxide film. Unfortunately, the exact oxygen concentration within the film could not be determined due to the spatial resolution limitations of the equipment.

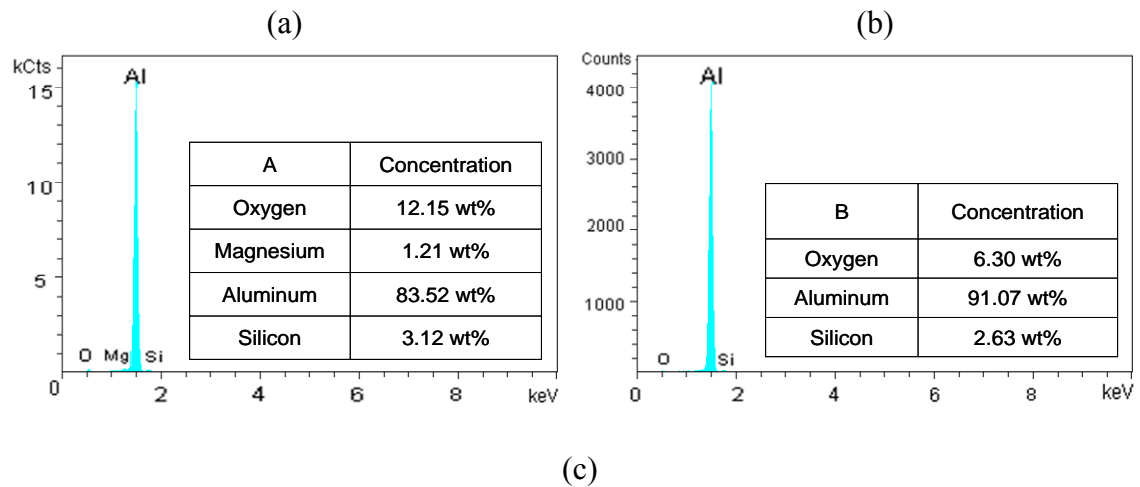
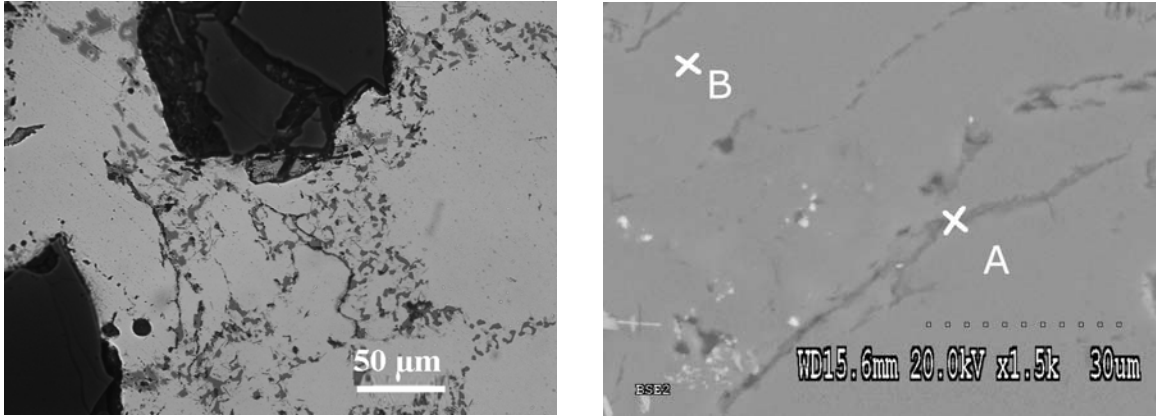


Figure 6.3: (a) Optical and (b) SEM image with (c) EDX analysis of a micrometer scale oxide film in the PoDFA samples.

SEM analysis of pores observed in the A356 castings was also undertaken in an attempt to find evidence of oxide films in association with the pores. The results for two pores are shown in Figure 6.4 (a) and (b). The SEM image of the pore appears on the left-hand-side of the figure and the associated EDX-based compositional map of oxygen appears on the right-hand-side. The results clearly show areas of elevated oxygen concentration association with the pores.

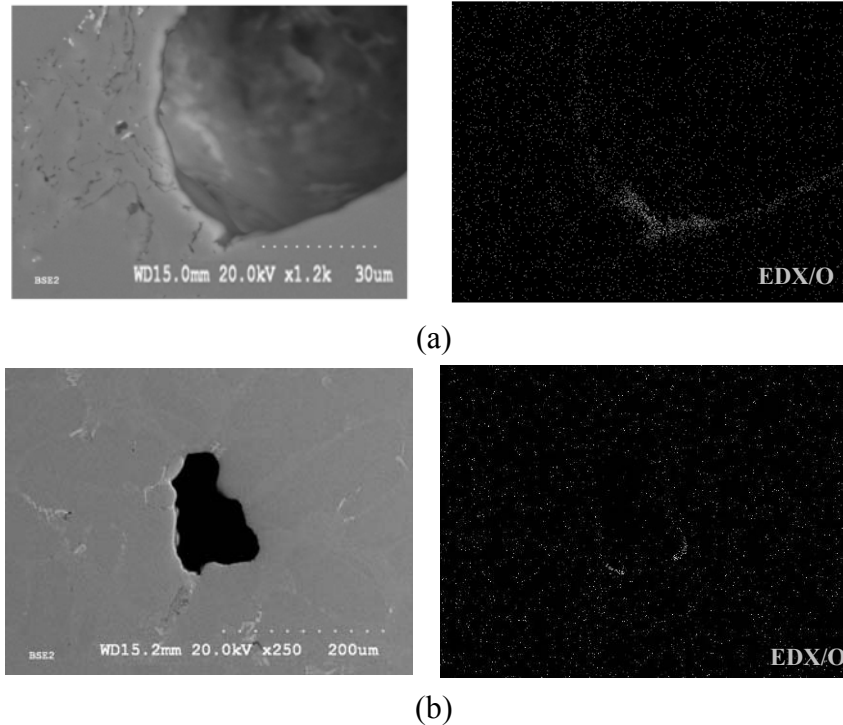


Figure 6.4: An example of EDX mapping analysis that shows presence of oxygen associated with pores in (a) PoDFA samples and (b) casting samples.

6.3.2 Microporosity analysis from XMT measurement

The XMT data from the samples cast under the different conditions was analyzed and the volume fraction, number density and size distribution of the pores, as a function of distance from the chill was determined. The data is presented as: 1) plots of volume fraction and number density vs. distance from the chill - see Figure 6.5 and Figure 6.7; 2) as 2-D projections of the 3-D rendered pores at 10, 30 and 50mm from the chill - see left-hand-side of Figure 6.6 and Figure 6.8; and 3) as a size distribution bar plot (number density vs. pore radius) - see right-hand-side of Figure 6.6 and Figure 6.8. In the line graphs, the experimental results appear as symbols, where as in the size distribution plot (bar chart) the experimental data appears as shaded bars. The error bars represent the deviation in the measurement associated with determination of grayscale threshold used

to distinguish the pores from matrix in the XMT analysis, as discussed in 4.2.2. The variation is based on the adjustment that lead to mistaking or obvious loss of porosity, as shown in Figure 4.4.

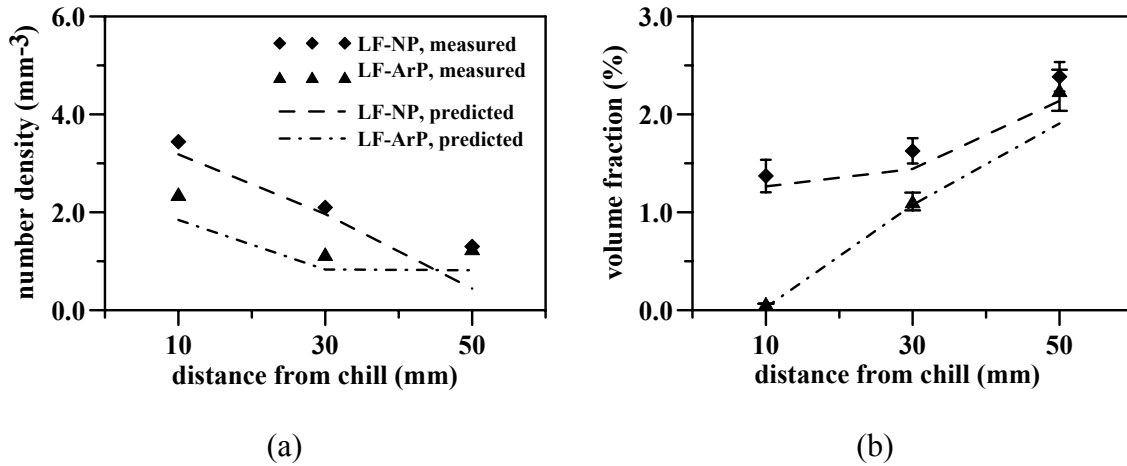


Figure 6.5: Comparison between measured (symbol) and predicted (dashed line) (a) pore number density and (b) volume fraction in samples resulted from normal pouring (LF-NP) and Ar shielded pouring (LF-ArP) conditions.

Effect of Ar shielded pouring - The results from the XMT measurement of the pore number density, pore volume fraction, and pore size distribution under normal pouring (NP) and argon shielded pouring (ArP) conditions are shown in Figure 6.5 and Figure 6.6. It is clear that the volume fraction, pore number and pore size all decrease under Ar shielded pouring. The reduction of the total number of pores indicates that the sites available for nucleation are reduced in number. The decreased pore size under the Ar shielded pouring condition indicates a delay in pore nucleation within the melt. Therefore, it would appear that a reduction in tendency to form oxide films affects the pore nucleation site distribution by reducing both the number of available nucleation sites and decreasing the potency of heterogeneous nucleation site population. The effect of Ar

shielding on nucleation site distribution will be discussed in a quantitative manner later in this chapter.

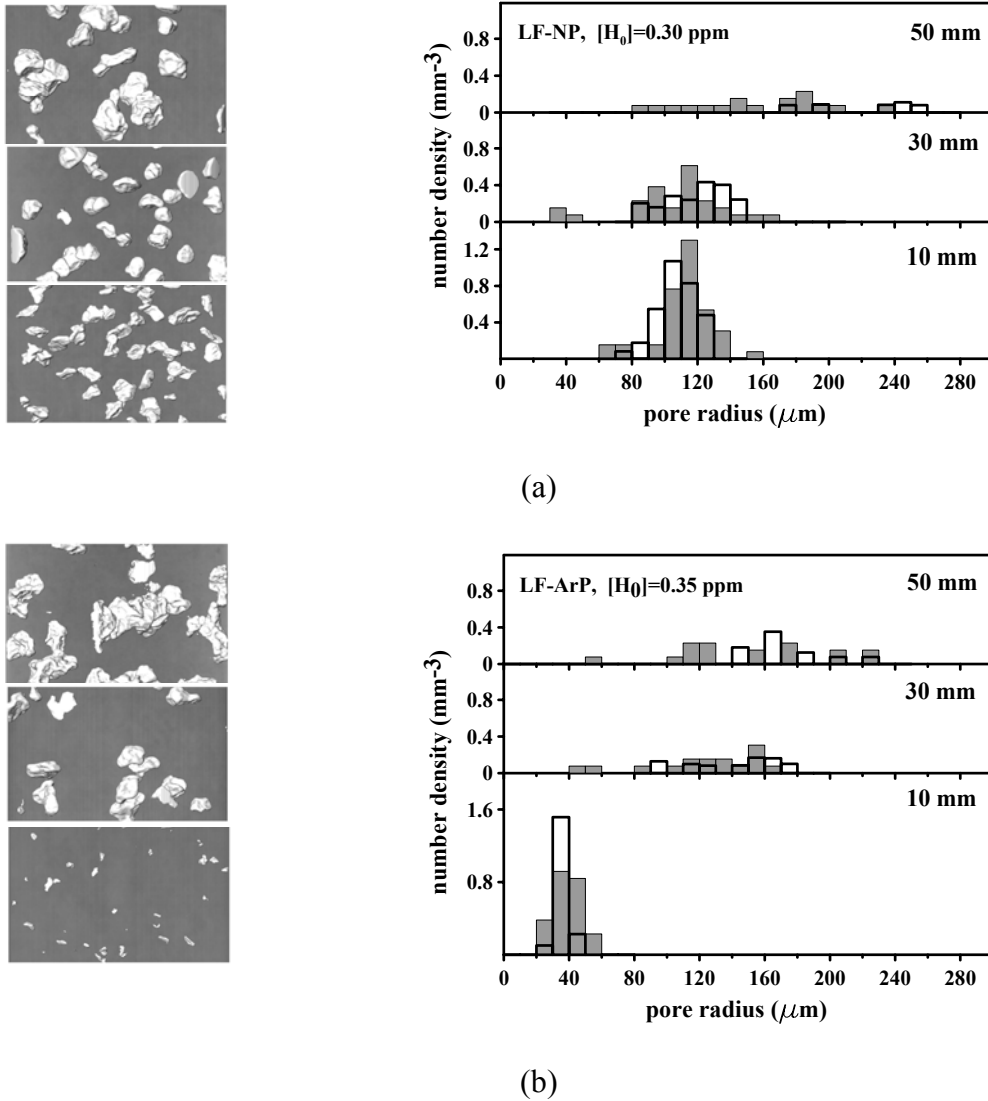


Figure 6.6: Comparison between measured (shaded bars) and predicted (un-shaded bars) pore size distribution at different distances from the chill in samples resulted from (a) normal pouring (LF-NP) and (b) Ar shielded pouring (LF-ArP) conditions.

Effect of high-surface-area pouring - The results from the XMT measurement of the pore number density, pore volume fraction, and pore size distribution under normal (NP) and high-surface-area (HSAP) pouring conditions are shown in Figure 6.7 and Figure 6.8.

Note: the UBC-HSAP casting contained slightly more hydrogen than the UBC-NP casting (0.30 vs 0.28ppm). The measurement shows that the high surface area pouring results in a pore volume fraction two times higher compared with normal pouring condition. By comparison of the measured pore size at the same locations in the two samples, it is obvious that the pore size increases significantly under the high-surface-area pouring condition, indicating earlier pore nucleation within the more oxidized melt. However, there is not much change in number density of the pores.

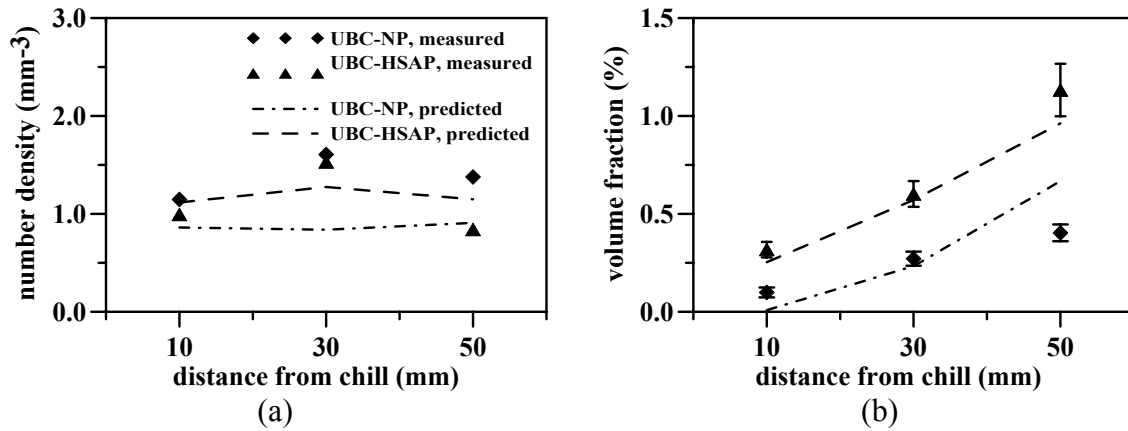


Figure 6.7: Comparison between measured (symbol) and predicted (dashed line) (a) pore number density and (b) volume fraction in samples resulted from normal pouring (UBC-NP) and high-surface-area pouring (UBC-HSAP) conditions.

It should be noted that the inclusion content was lower in the HSAP condition as previously shown in Table 6.3, and thus the enhanced pore formation can be attributed to an increase in metal surface area during pouring associated with the use of the unsaturated filter. This is consistent with literature that states carbides wet the liquid well and as such will not provide good heterogeneous nucleation sites for porosity, whereas they would provide good nucleation sites for solid grains [14].

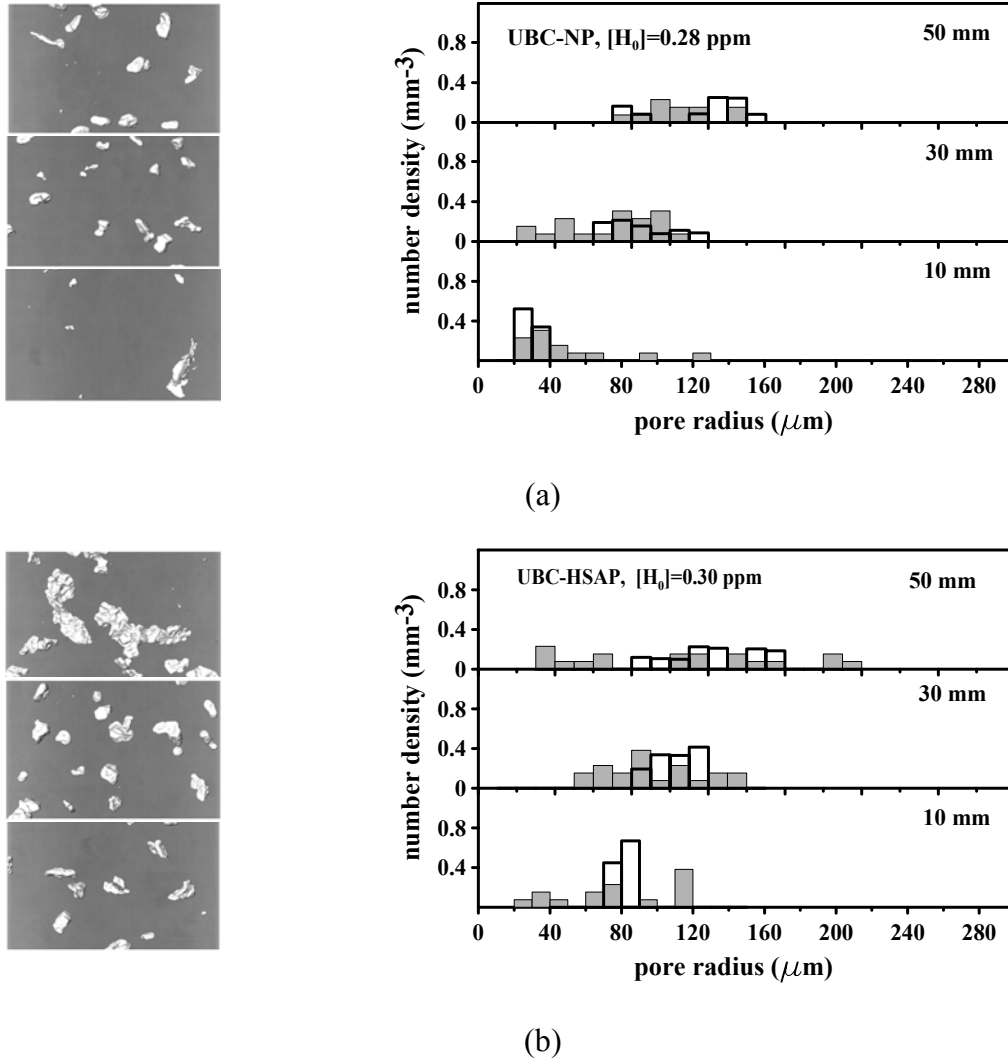


Figure 6.8: Comparison between measured (shaded bars) and predicted (un-shaded bars) pore size distribution at different distances from the chill in samples resulted from (a) normal pouring (UBC-NP) and (b) high-surface-area pouring (UBC-HSAP) conditions.

6.4 Mathematical model analysis

As previously described, with the pore nucleation and growth model in Chapter 5 it is possible to de-convolute the relative contributions of hydrogen content, cooling rate and heterogeneous nucleation population, all of which are varying from casting-to-casting. Thus it is possible to single-out the effect of changes in the pouring conditions on pore nucleation kinetics.

6.4.1 Determination of fitting parameter m

Figure 6.9 shows the impingement factor exponent m as a function of cooling rate determined by fitting with the experimental measurements. As the impingement factor is linked to the solidification morphology, it should only be dependent on cooling rate and alloy composition, not the pouring conditions. The variation of m with cooling rate is consistent with a reduction in impingement with decreasing cooling rate (increasing grain size). It can also be seen that a smaller m was needed for the LF samples, corresponding to a lower impingement between pores and solid grains at a given fraction solid. This can be explained by comparing the microstructures of the LF and UBC metal, shown in Figure 6.10. There is no apparent difference in grain size. The most obvious difference is that LF metal (Figure 6.10(a)) solidifies into a structure that is more globular dendritic than the UBC material (Figure 6.10(b)). As a result, one would expect a smaller pore/solid impingement in the LF structure at a given solid fraction. Within a given alloy group – i.e. LF vs UBC metal – it was possible to use a single cooling rate dependent m , for evaluation of the various pouring conditions. Additionally, it was found that the impingement factor in UBC castings is closer to the castings in Chapter 5, which are also unmodified.

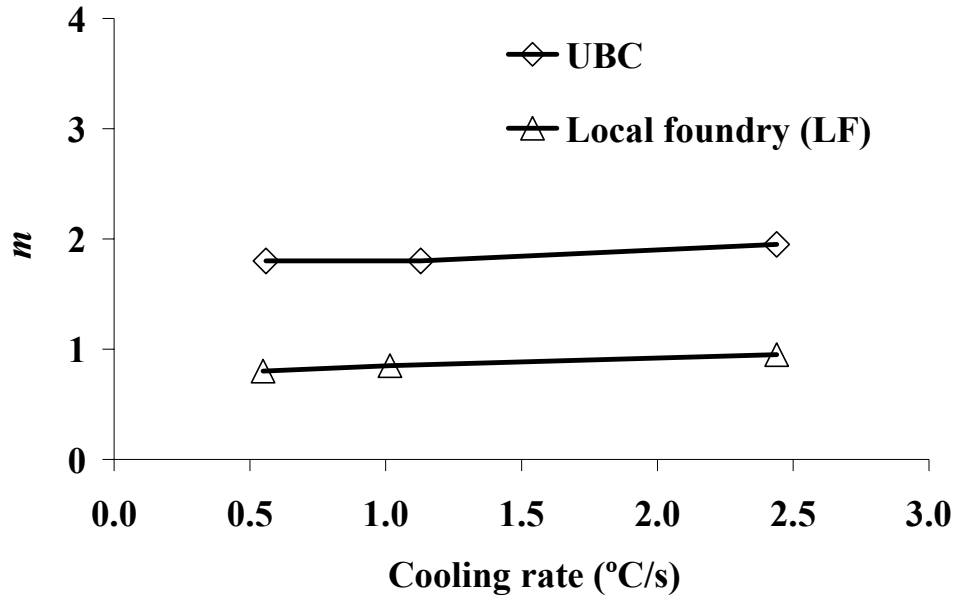


Figure 6.9: m in the impingement factor as a function of cooling rate determined by fitting the model predictions with experimental measurement.

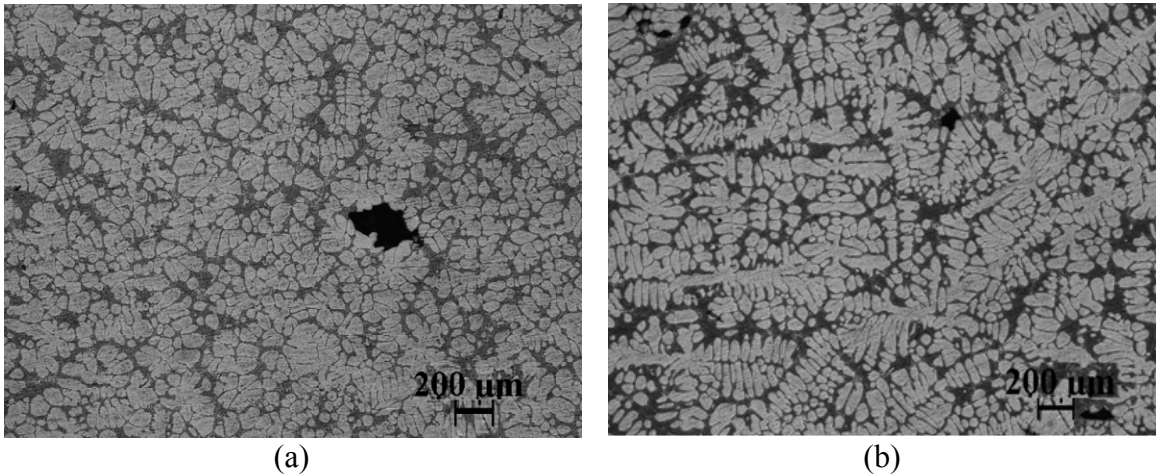


Figure 6.10: Optical micrograph of as-cast microstructures in samples resulted from different metal sources at (a) local foundry (LF) and (b) UBC.

6.4.2 Determination of nucleation parameters

Figure 6.11 shows plots of the residual, R , obtained for various combinations of ss_0 and σ for the four experimental castings using the coarse fitting procedure previously outlined. Referring to the legend that appears above the plots, low residuals can be

obtained for values of σ between 0.2 and 2 mol/m³, and, values of ss_0 between 1 and 3 mol/m³ for the LF-NP casting; low residuals can be obtained for values of σ between 0.5 and 2 mol/m³, and, values of ss_0 between 8 and 10 mol/m³ for the LF-ArP casting; low residuals can be obtained for values of σ between 0.2 and 1.2 mol/m³, and, values of ss_0 between 0.2 and 0.5 mol/m³ for the UBC-NP casting; and low residuals can be obtained for values of σ between 0.2 and 1.0 mol/m³, and, values of ss_0 between 0.2 and 0.5 mol/m³ for the UBC-HSP casting. Clearly the addition of argon shielding has greatly increased the supersaturation necessary for pore nucleation. Also it would appear that in general lower supersaturations are required in the UBC castings compared with the LF castings.

6.4.3 Model fit to experimental data

Following coarse fitting, the values for ss_0 and σ were fine-tuned for each casting condition to obtain what may be termed an “optimum” fit. The resulting comparisons between the model predictions and XMT measurements can be found in Figure 6.5 through Figure 6.8. In the x - y plots, the model predictions appear as the lines. In the distribution plots (bar charts) the model predictions appear as the un-shaded bars. As can be seen, the model is able to reproduce the variation in volume fraction and number density of pores with distance from the chill at 10, 30 and 50mm from the chill. Furthermore, the model is also able to reproduce the correct trend in pore size distribution observed in the sample to a reasonable degree of accuracy.

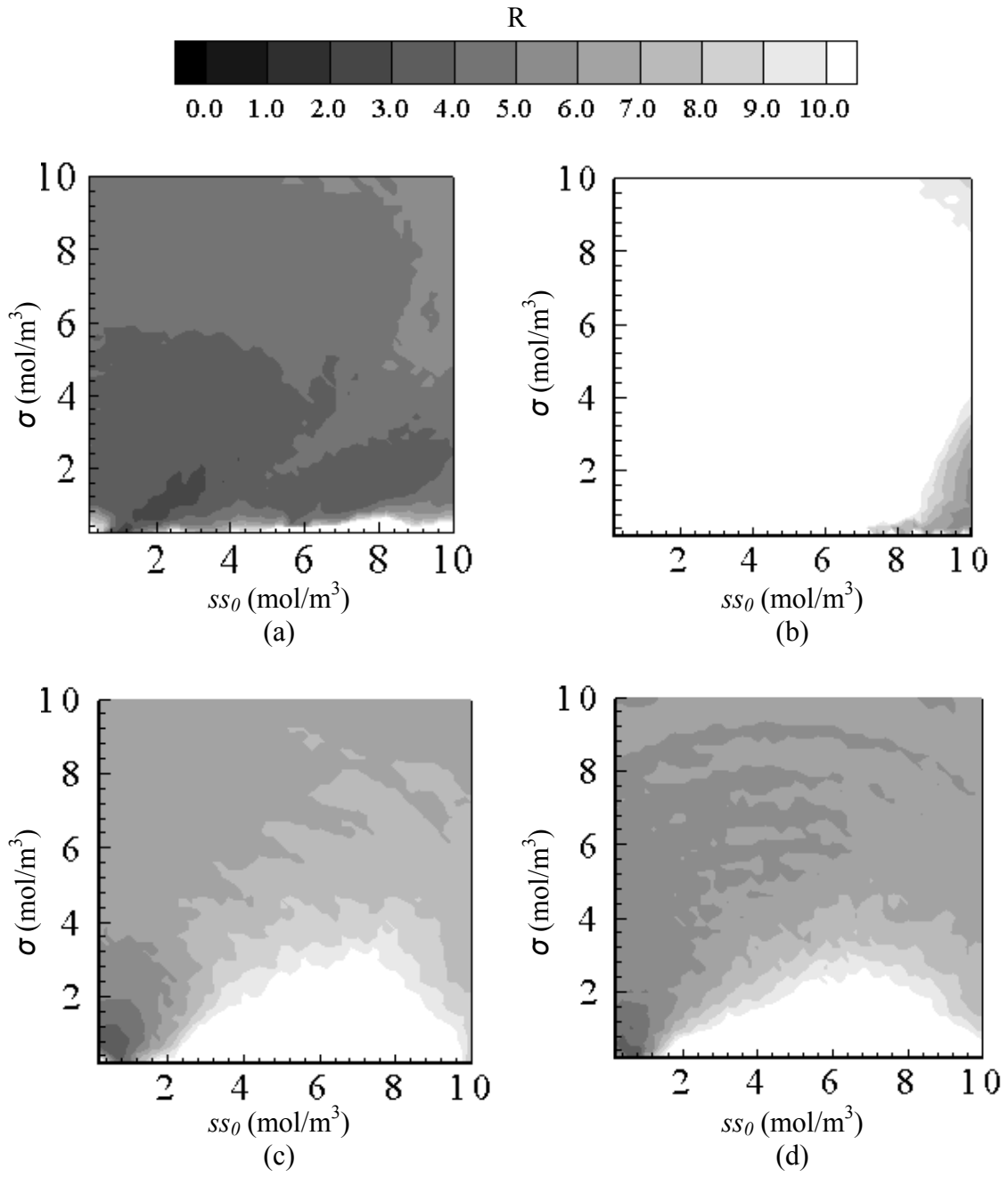


Figure 6.11: Plots showing residual R as a function of ss_0 and σ used in the coarse fitting process for samples (a) LF-NP, (b) LF-ArP, (c) UBC-NP and (d) UBC-HSAP.

6.4.4 Pore nucleation kinetics

Figure 6.12 shows the model-predicted nucleation site distribution under the four different casting conditions: LF-NP, LF-ArP, UBC-NP and UBC-HSAP. As can be seen, both the pouring conditions and the metal source have a quantifiable effect on the nucleation kinetics.

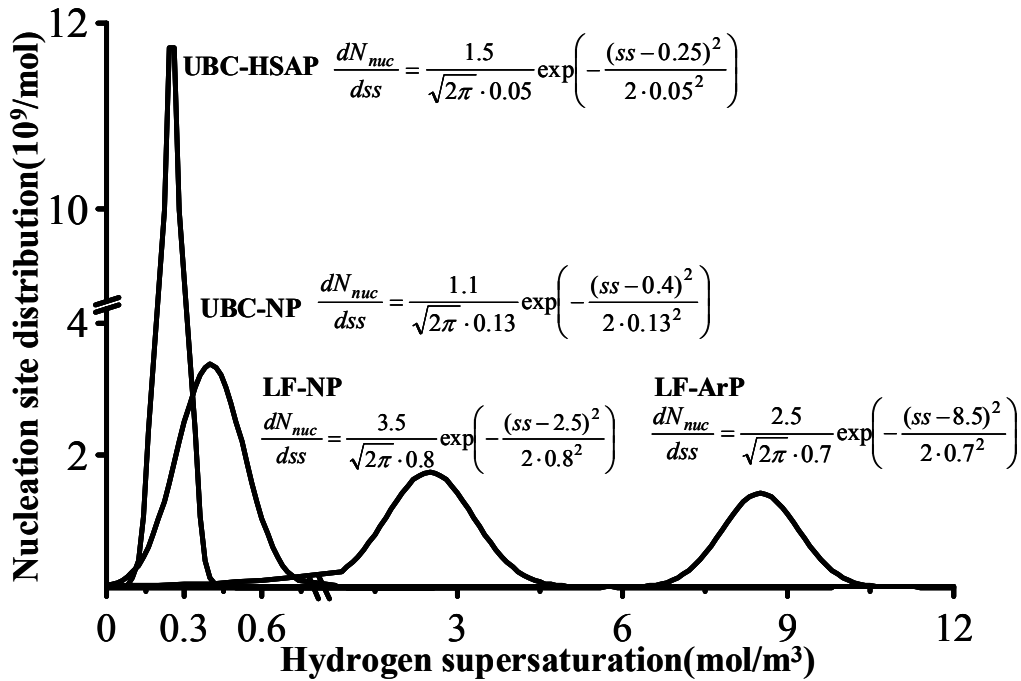


Figure 6.12: Pore nucleation site distribution under various casting conditions derived by fitting the model predictions with experimental measurement.

Starting with the pouring method, the effect of Ar shielding on nucleation site distribution can be seen by comparing the plot for LF-NP and LF-ArP in Figure 6.12. The nucleation potency is reduced when Ar shielding is applied, as indicated by an increase of ss_0 from 2.5 mol/m³ to 8.5 mol/m³. The total number of nucleation sites is also reduced for the Ar shielded pouring condition, indicated by a decrease of A from 3.5 per mm³ to 2.5 per mm³. As discussed previously, Ar would reduce the tendency to form oxide films

during pouring and therefore the amount entrained within the melt. It is difficult to conclude whether the nucleation sites present in the ArP casting are as a result of some oxidation of the pour stream, which is likely as the argon shielding would not have been complete, or are as a result of oxides formed during liquid metal processing (upstream of the casting process).

Comparing the plots for UBC-NP and UBC-HSAP in Figure 6.12 shows the effect of pour surface area. The nucleation potency increases with pour surface area as indicated by a decrease of ss_0 from 0.40 mol/m^3 to 0.25 mol/m^3 . In addition, there is an increase in total number of nucleation sites, from 1.1 per mm^3 to 1.5 per mm^3 . This result is obtained despite a decrease in the Al_4C_3 , MgAl_2O_4 , $(\text{TiV})\text{B}_2$ and TiB_2/TiC content in the HSAP sample as shown in Table 6.3 as a result of passing the metal through the filter. The relatively small difference as compared with the previous comparison may be due to the fact that the so-called “normal” pouring process used in this study has a relatively high surface area and is effective in oxidizing the melt. It should be noted that there is an inconsistency between the measured number density of the pores and the predicted number density of nucleation sites: there is not much change in pore number density (Figure 6.7), but an increase in total number of nucleation sites (Figure 6.12). The reason for this is unclear and could relate to the loss of the small pores below the resolution limit of the XMT analysis, especially near the chill of the castings.

Both the ArP/NP comparison and the HSAP/NP comparison support the notion that oxide films formed during pouring are effective nucleation sites for porosity. Moreover, this result is consistent with the EDX results discussed earlier in this work that showed areas of increased oxygen concentration associated with pores. The HSAP/NP

comparison also is consistent with literature in-so-far-as the increased presence of carbides did not appear to be a factor affecting the nucleation kinetics and hence they are not effective as nucleation sites for hydrogen porosity [14].

By comparing the LF-NP and UBC-NP plots in Figure 6.12, which were poured in the same way, the effect of metal source on the nucleation site distribution can be seen. The model predicts that the number of nucleation sites (A) in the LF casting relative to the UBC sample increased from 1.1 to 3.5 mm⁻³ and that the hydrogen supersaturation required for pore nucleation (ss_0) increased from 0.4 mol/m³ to 2.5 mol/m³. Both differences are substantial, offsetting and therefore warrant some discussion.

As the role of non-pour-related inclusions has been discounted the only possible additional factor that warrants discussion is the difference in the Sr content between the two alloys as can be seen in Table 6.2. Higher levels of Sr (normally added to modify the eutectic structure) may increase the amount of oxides in the melt due to its higher affinity for oxygen and thus increase the number of nucleation sites. This theory has been proposed before based on an increase in the porosity fraction observed at higher Sr levels [34, 37, 138]. This is consistent with the increase observed in the LF-NP casting. As to the opposing effect, it has been reported that Sr modification reduces the surface tension of liquid A356 alloy [118, 119]. Application of the well-know Young's equation to Figure 3.6 (a) results in the following expressions:

$$\gamma_{gs} + \gamma_{gl} \cos \theta = \gamma_{ls} \quad \text{Equation 6.3}$$

where γ_{gs} , γ_{gl} and γ_{ls} are the surface tensions (N/m) at the gas/substrate, gas/liquid and liquid /substrate interfaces, respectively. In Equation 6.3, when γ_{ls} is small, θ is large, indicating less spreading-out of the gas phase on the substrate (Figure 3.6(b)) and an

increase in the critical free-energy for nucleation, as discussed in 3.2.2. Therefore, a decrease of γ_{1s} in the LF castings due to the higher Sr content would cause a decrease in the effectiveness of the substrate as a site for heterogeneous nucleation of hydrogen pores. This is consistent with the higher hydrogen supersaturation required for pore nucleation in the castings conducted at the local foundry. A delay in pore initiation related to an increase in Sr concentration has also been discussed in Campbell's bifilm theory [163], where it was proposed that Sr modification increases the impermeability of the bi-films and thus suppresses initiation of hydrogen diffusion into the unbonded interfaces. Thus, the behaviour predicted by the model, related to the higher level of Sr (both the increase in the number of nucleation sites and the decrease in their potency) is fully consistent with previous work appearing in the literature. On balance, clearly there is a marked increase in the volume fraction of porosity and in the number of large pores in the LF cast sample relative to the UBC cast sample. However, the analysis with the model reveals that this is principally due to the decrease in the impingement factor limiting pore growth in LF alloy due to modification of the grain structure and not due to a change in the nucleation kinetics of pores.

6.5 Summary and conclusions

The effect of the tendency to generate oxide films/inclusions during pouring on hydrogen based porosity formation has been examined in detail. The volume fraction, pore number density and pore size distribution in directionally solidified castings resulting from different pouring conditions in which oxidation was enhanced and suppressed relative to a base case has been characterized via 3-D XMT analysis. By

fitting a comprehensive pore nucleation and growth numerical model with the 3-D XMT measurements the nucleation kinetics have been quantified using a nucleation site distribution based on a Gaussian function of hydrogen supersaturation. The conclusions obtained are as follows:

- 1) Oxide films/inclusions formed during pouring and subsequently entrained into the melt provide effective sites for pore nucleation and as such can greatly enhance the pore volume fraction and maximum pore size for a given hydrogen content.
- 2) Increasing the tendency to oxidize the melt during pouring results in a small increase in the number of nucleation sites and a small increase in the potency of the nucleation sites.
- 3) Decreasing the tendency to oxidize the melt during pouring results in both a substantial decrease in the number of nucleation sites and in the potency of the nucleation sites.
- 4) The addition of Sr appears to both increase the tendency of the melt to be oxidized (increase the number of pore nucleation sites) and decrease the potency of the oxides as heterogeneous nucleation sites for hydrogen porosity. The later effect is due to the effect of Sr on the liquid/solid substrate surface tension.
- 5) The dominant effect of Sr on the pore volume fraction and maximum pore size is to reduce hydrogen pore impingement on solid grains thereby leading to an increase in the number of large pores. This is realized through the impact of modification on the primary grain morphology.

The results of this work at this stage appear to support both of the two predominant theories of pore nucleation in aluminum alloys – i.e., that pores nucleate on oxide film substrates or that they form via preexisting trapped bubbles associated with oxide bi-films proposed by Campbell. The role of Sr as a means of decreasing the potency of heterogeneous nucleation population appears to support the more traditional heterogeneous nucleation theory. Clearly more work is needed.

7 Summary and Conclusions

This work has studied the formation of hydrogen-induced microporosity in A356 alloy castings. First, conventional metallography and X-ray microtomography (XMT) analysis on microporosity formed in directionally solidified A356 castings was performed to study the effect of cooling rate and degassing time on microporosity formation. The volume fraction and size distribution of the pores were measured and used to validate a model that was developed to predict microporosity formation. The model developed in this program is comprehensive and accounts for pore nucleation and growth kinetics, varying initial hydrogen content and varying microstructure via an impingement factor. The model was shown to be capable of predicting the final pore size distribution in the castings under the conditions examined in the study. The novel and new contributions of this work include the development of an expression for the nucleation kinetics in terms of hydrogen supersaturation and the application of a comprehensive model to predict nucleation kinetics under a variety of conditions. The later has helped to delineate quantitatively for the first time the effect of degassing, pouring and Sr on the pore nucleation population in A356.

7.1 Conclusions

The findings of this PhD research project can be summarized as below:

- 1) The initial hydrogen content and cooling rate of aluminum A356 alloy have a strong impact on microporosity formation in directionally solidified A356 castings. The experimental results show that the porosity volume fraction and pore size increase with initial hydrogen content and with decreasing cooling rate;

- 2) Comparison of 2-D optical image analysis and 3-D XMT analysis of microporosity in A356 casting samples reveals that both are able to measure the trend in variation of porosity with distance from the chill and degassing time. The optical image based 2-D analysis however results in a qualitative measurement only and can lead to estimations that are not representative of the pore size distribution;
- 3) The 3-D XMT analysis of the size distribution of porosity found in the 0.5-min and 1.0-min degassed sample shows a bimodal distribution of the pores. The bimodal distribution contained a population of pores of large equivalent radii and a second population of small radii, with few found in the intermediate size range;
- 4) A microporosity simulation model predicting both the porosity volume fraction and the pore size distribution has been developed and validated. The results show that the heterogeneous nucleation site distribution can be simulated as a Gaussian function of hydrogen supersaturation in the melt and that once nucleated, pore growth is a hydrogen diffusion controlled process under directional solidification of A356 alloy;
- 5) Sensitivity analysis of the model to different input parameters shows the role of various factors on pore formation. The model is sufficiently complex in its formulation that the effect of pore/solid impingement, surface tension of the melt and local pressure drop can be considered;
- 6) The model shows a dependence of the heterogeneous nucleation population on degassing time. Degassing acts to both reduce the hydrogen in solution available for pore nucleation and growth and also reduces the tendency to nucleate pores;
- 7) XMT measurement of pores formed under different pouring conditions shows that the pore volume fraction, size and number density increase with increased tendency to form

and entrain oxide films in the melt. The nucleation site distribution determined by fitting with the microporosity model indicates that oxide film inclusions formed during pouring and subsequently entrained into the melt provide effective sites for pore nucleation;

8) Quantification of inclusions with PoDFA analysis shows the presence of carbides (Al_4C_3), spinels (MgAlO_4) and grain refiners as the major inclusions, and traces of chlorides, MgO, graphite and refractory material in A356 castings. The PoDFA analysis is not able, though, to measure oxide film content in the melt. EDX mapping analysis of pores in the PoDFA samples and in the castings shows areas of increased oxygen concentration associated with the pores;

9) This work for the first time de-convolutes various mechanisms by which strontium can influence pore formation. First, higher level of Sr increases the amount of oxides in the melt due to its higher affinity for oxygen and thus increases the number of nucleation sites. Second, Sr modification increases the wettability of the substrate by the liquid and thus decreases the effectiveness of the substrate as a site for heterogeneous nucleation of hydrogen pores. Therefore, the nucleation potency is reduced. The dominant effect of Sr derived from the model analysis, however, is to reduce pore impingement on solid grains due to modification of the grain structure thereby leading to an increase in pore growth.

7.2 Future work

The microporosity model in this work is developed and validated based on hydrogen induced microporosity formation in tapered cylindrical castings. Application of the model can be extended to prediction of pore size in cast components with more complicated geometries. However in more complex castings macro-transport of hydrogen within the

liquid arises as an issue and should not be neglected. A term related to mass transport in and out of the volume element should be added to Equation 5.9. The model developed in this work considers the effect of pressure drop by Equation 5.3, Equation 5.4 and Equation 5.12 and therefore the model could be applied to cases where there is a significant pressure drop. However, the growth of shrinkage pores requires an accurate simulation of pressure drop in the mushy zone during solidification. Additional work is also needed to better quantify the effect of S_r .

Reference

- [1] J.D. Edwards, F.C. Frary, Z. Jeffries, *The Aluminum Industry*, McGraw-Hill, New York and London, 1930.
- [2] F. Wohler, *Annalen der Physik und Chemie* (1827).
- [3] C. Karmarsch, *Polytechnisches Journal* 171(1) (1864).
- [4] I.J. Polmear, *Production of Aluminium - Light Alloys from Traditional Alloys to Nanocrystals*, Oxford: Elsevier/Butterworth-Heinemann, 2006.
- [5] C.M. Hall, *Process of Reducing Aluminium from its Fluoride Salts by Electrolysis*, in: vol US patent 400664., 1889-04-02
- [6] D.H. Wallace, *Market Control in the Aluminum Industry*, Harvard University Press, 1977.
- [7] *Mineral Commodity Summaries*, in: 2011.
- [8] A.M. Howatson, P.G. Lund, J.D. Todd, *Engineering Tables and Data*, Chapman & Hall, 1992.
- [9] K. Louisville, *The ABC's of aluminum Reynolds Metals Company*, 1953.
- [10] J.G. Kaufman, *Introduction to Aluminum Alloys and Tempers*, ASM International, 2000.
- [11] Q. Han, *ASM Handbook*, ASM International Handbook Committee © 2008 ASM International, 2010.
- [12] M. Lalpoor, D.G. Eskin, G. ten Brink, L. Katgerman, *Materials Science and Engineering A-Structural Materials Properties Microstructure and Processing* 527 (2010) 1828-1834.
- [13] B.G. Thomas, M. Bellet, *ASM Handbook*, ASM International Handbook Committee © 2008 ASM International, 2010.
- [14] J. Campbell, *Castings*, Butterworth-Heinemann, Oxford, 2003.
- [15] B. Zhang, S.L. Cockcroft, D.M. Maijer, J.D. Zhu, A.B. Phillion, *Journal of Minerals, Metals and Materials Society* 57(11) (2005) 36-43.
- [16] H.R. Ammar, A.M. Samuel, F.H. Samuel, *Materials Science and Engineering A-Structural Materials Properties Microstructure and Processing* 473 (2008) 65-75.
- [17] M.H. Lee, J.J. Kim, K.H. Kim, N.J. Kim, S. Lee, E.W. Lee, *Materials Science and Engineering A-Structural Materials Properties Microstructure and Processing* 340 (2003) 123-129.

- [18] Q.G. Wang, D. Apelian, D.A. Lados, *Journal of Light Metals* 1 (2001) 85-97.
- [19] G. Rading, J. Li, J.T. Berry, *AFS Trans.* 102 (1994) 5.
- [20] B. Skallerud, T. Iveland, G. Härkegård, *Engineering Fracture Mechanics* 44 (1993) 857-874.
- [21] A.A. Dabayeh, R.X. Xu, B.P. Du, T.H. Topper, *International Journal of Fatigue* 18 (1996) 95-104.
- [22] J.F. Major, *AFS Trans.* 105 (1997) 6.
- [23] X. Zhu, J.Z. Yi, J.W. Jones, J.E. Allison, *Metallurgical and Materials Transactions A-Physical Metallurgy and Materials Science* 38A (2007) 1111-1122.
- [24] J.Z. Yi, X. Zhu, J.W. Jones, J.E. Allison, *Metallurgical and Materials Transactions A-Physical Metallurgy and Materials Science* 38A (2007) 1123-1135.
- [25] P. Li, P.D. Lee, D.M. Maijer, T.C. Lindley, *Acta Materialia* 57 (2009) 3539-3548.
- [26] G. Nicoletto, G. Anzelotti, R. Konecna, X-ray computed tomography vs. metallography for pore sizing and fatigue of cast Al-alloys, in: P. Lukas (Ed.) *Fatigue* 2010, vol 2, 2010, pp. 547-554.
- [27] Q.G. Wang, C.H. Caceres, *Materials Science and Engineering A-Structural Materials Properties Microstructure and Processing* 241 (1998) 72-82.
- [28] C.H. Caceres, *Scripta Metallurgica Et Materialia* 32 (1995) 1851-1856.
- [29] C.H. Caceres, B.I. Selling, *Materials Science and Engineering A-Structural Materials Properties Microstructure and Processing* 220 (1996) 109-116.
- [30] X. Teng, H. Mae, Y. Bai, T. Wierzbicki, *Engineering Fracture Mechanics* 76 (2009) 983-996.
- [31] A.K. Dahle, S.D. McDonald, K. Nogita, Eutectic solidification in hypoeutectic Al-Si alloys and its effect on porosity, in: *The 17th International Conference of Australian Society for Ey*, ASM International, Member/Customer Service Center, *Materials Solutions* 2002, Columbus, OH, USA, 2002, p. 10.
- [32] L. Liu, A.M. Samuel, F.H. Samuel, *Journal of Materials Science* 38 (2003) 1255-1267.
- [33] X.G. Chen, S. Engler, *AFS Transactions* 102 (1994) 673-682.
- [34] D. Emadi, J.E. Gruzleski, *AFS Transactions* 102 (1994) 307-312.
- [35] D. Emadi, J.E. Gruzleski, M. Pekguleryuz, *AFS Transactions* 104 (1996) 763-768.

- [36] G. Laslaz, P. Laty, AFS Transactions 99 (1991) 673-680.
- [37] K. Tynelius, M.J. F., A. D., AFS Transactions 101 (1993) 401-413.
- [38] J. Campbell, Materials Science and Technology 22 (2006) 127-145.
- [39] D. Dispinar, J. Campbell, International Journal of Cast Metals Research 17 (2004) 280-286.
- [40] D. Dispinar, J. Campbell, International Journal of Cast Metals Research 17 (2004) 287-294.
- [41] P.D. Lee, A. Chirazi, D. See, Journal of Light Metals 1 (2001) 15-30.
- [42] D.M. Stefanescu, International Journal of Cast Metals Research 18 (2005) 129-143.
- [43] N. Roy, A.M. Samuel, F.H. Samuel, Metallurgical and Materials Transactions A-Physical Metallurgy and Materials Science 27 (1996) 415-429.
- [44] K. Gall, N. Yang, M. Horstemeyer, D.L. McDowell, J. Fan, Fatigue & Fracture of Engineering Materials & Structures 23 (2000) 159-172.
- [45] W. Ludwig, J.Y. Buffiere, S. Savelli, P. Cloetens, Acta Materialia 51 (2003) 585-598.
- [46] P.D. Lee, T.C. Lindley, Shape Casting of Metals: The John Campbell Symposium, 2005, p. 225-234.
- [47] S. Gungor, L. Edwards, Fatigue & Fracture of Engineering Materials & Structures 16 (1993) 391-403.
- [48] J.Y. Buffiere, S. Savelli, P.H. Jouneau, E. Maire, R. Fougères, Materials Science and Engineering A-Structural Materials Properties Microstructure and Processing 316 (2001) 115-126.
- [49] Q.G. Wang, D. Apelian, D.A. Lados, Journal of Light Metals 1 (2001) 73-84.
- [50] P.C. Paris, M.P. Gomez, W.E. Anderson, The Trend in Engineering 13 (1961) 9-14.
- [51] Y. Murakami, Metal Fatigue: Effects of Small Defects and Nonmetallic Inclusions, Elsevier Ltd., 2002.
- [52] K.J. Miller, Fatigue of Engineering Materials and Structures 5 (1982) 223-232.
- [53] Miller KJ, d.l.R. ER, The behaviour of short fatigue cracks, European Group of Fracture, London, 1986.
- [54] S.F. Jones, G.M. Evans, K.P. Galvin, Advances in Colloid and Interface Science 80 (1999) 27-50.

- [55] K.D. Li, E. Chang, *Acta Materialia* 52 (2004) 219-231.
- [56] J.C. Fisher, *Journal of Applied Physics* 19 (1948) 1062-1067.
- [57] R.C. Atwood, S. Sridhar, W. Zhang, P.D. Lee, *Acta Materialia* 48 (2000) 405-417.
- [58] R.C. Atwood, S. Sridhar, P.D. Lee, *Scripta Materialia* 41 (1999) 1255-1259.
- [59] P.D. Lee, J.D. Hunt, *Scripta Materialia* 36 (1997) 399-404.
- [60] P.D. Lee, A. Chirazi, R.C. Atwood, W. Wang, *Materials Science and Engineering A-Structural Materials Properties Microstructure and Processing* 365 (2004) 57-65.
- [61] L. Arnberg, R.H. Mathiesen, *Jom* 59 (2007) 20-26.
- [62] R.C. Atwood, P.D. Lee, A combined cellular automaton and diffusion model for the prediction of porosity formation during solidification, in: *Modeling of Casting, Welding and Advanced Solidification Processes*, 2000, pp. 2-9.
- [63] P.D. Lee, J.D. Hunt, *Modeling of Casting, Welding and Advanced Solidification Processes VII* (1995) 585-592.
- [64] M. Felberbaum, Porosity in aluminum alloys: visualization, characterization, and modeling, in: *École Polytechnique Fédérale de Lausanne, Ph. D. Thesis, Lausanne, 2010.*
- [65] D.A. Porter, K.E. Easterling, *Phase Transformations in Metals and Alloys*, Van Nostrand Reinhold, Berkshire, 1981.
- [66] M. Massoud, *Engineering thermofluids: thermodynamics, fluid mechanics, and heat transfer*, Springer, 2005.
- [67] S. Fox, J. Campbell, *Scripta Materialia* 43 (2000) 881-886.
- [68] W.D. Griffiths, R. Raiszadeh, *Journal of Materials Science* 44 (2009) 3402-3407.
- [69] H.D. Zhao, C.Z. Wu, Y.Y. Li, *International Journal of Cast Metals Research* 21 (2008) 313-318.
- [70] J.A. Pryde, C.G. Titcomb, *Journal of Physics Part C Solid State Physics* 5 (1972) 1293-&.
- [71] R.N. Hills, D.E. Loper, P.H. Roberts, *Quarterly Journal of Mechanics and Applied Mathematics* 36 (1983) 505-539.
- [72] C. Pequet, M. Gremaud, M. Rappaz, *Metallurgical and Materials Transactions A-Physical Metallurgy and Materials Science* 33 (2002) 2095-2106.
- [73] H.B. Aaron, Fainstei.D, G.R. Kotler, *Journal of Applied Physics* 41 (1970) 4404-4410.

- [74] A.N. Kolmogorov, *Izvestiya Akademii Nauk SSSR Seriya Matematika* 3 (1937) 355-360.
- [75] W.A. Johnson, R.F. Mehl, *Trans. AIME* 135 (1939) 416-441.
- [76] M. Avrami, *J. Chem. Phys.* 8 (1940) 212-224.
- [77] G.R. Speich, R.M. Fisher, American Society for Metals, Metal Park, OH (1966) 563-598.
- [78] K.D. Carlson, Z.P. Lin, C. Beckermann, *Metallurgical and Materials Transactions B-Process Metallurgy and Materials Processing Science* 38 (2007) 541-555.
- [79] J. Zou, S. Shivkumar, D. Apelian, *AFS Transactions* 98 (1990) 871-878.
- [80] P.M. Thomas, J.E. Cruzleski, *Metallurgical and Materials Transactions B* 9B (1978) 139-141.
- [81] G.K. Sigworth, C. Wang, *AFS Transactions* 100 (1992) 989-1004.
- [82] A.M. Samuel, F.H. Samuel, *AFS Transactions* 100 (1992) 657-666.
- [83] J.G. Conley, J. Huang, J. Asada, K. Akiba, *Materials Science and Engineering A-Structural Materials Properties Microstructure and Processing* 285 (2000) 49-55.
- [84] J.P. Anson, *AFS Transactions* 107 (1999) 135-142.
- [85] P.D. Lee, R.C. Atwood, R.J. Dashwood, H. Nagaumi, *Materials Science and Engineering A-Structural Materials Properties Microstructure and Processing* 328 (2002) 213-222.
- [86] R.C. Atwood, P.D. Lee, *Acta Materialia* 51 (2003) 5447-5466.
- [87] D.V. Neff, *ASM Handbook*, ASM International, 2010.
- [88] D. Dispinar, S. Akhtar, A. Nordmark, M. Di Sabatino, L. Arnberg, *Materials Science and Engineering A-Structural Materials Properties Microstructure and Processing* 527 (2010) 3719-3725.
- [89] P.L. Schaffer, A.K. Dahle, *Metallurgical and Materials Transactions A-Physical Metallurgy and Materials Science* 40A (2009) 481-485.
- [90] V.S. Warke, S. Shankar, M.M. Makhlof, *Journal of Materials Processing Technology* 168 (2005) 119-126.
- [91] D. Apelian, Aluminum cast alloys: enabling tools for improved performance, in: *World Wide Report*, North American Die Casting Association, 2009.

- [92] O. Lashkari, L. Yao, S. Cockcroft, D. Maijer, *Metallurgical and Materials Transactions A-Physical Metallurgy and Materials Science* 40A (2009) 991-999.
- [93] V.d.L. Davies, *AFS Cast Metals Res. J.* (1975, June) 33-44.
- [94] E. Niyama, T. Uchida, M. Morikawa, S. Salto, A method of shrinkage prediction and its application to steel castings, in: 49th International Foundry Congress, 1982, pp. 1-12.
- [95] J. Lecomte-Beckers, *Metallurgical and Materials Transactions A* 19(9) (1988) 2341-2348.
- [96] C. Tian, J. Law, J. van der Touw, M. Murray, J.Y. Yao, D. Graham, D.S. John, *Journal of Materials Processing Technology* 122 (2002) 82-93.
- [97] B.D. Sun, W.J. Ding, D. Shu, Y.H. Zhou, *Journal of Central South University of Technology* 11 (2004) 134-141.
- [98] D. Apelian, How clean is the metal you cast? The issue of assessment: a status report, in: *Proceeding of 3rd Int. Conf. on Molten Aluminum Processing*, 1992, pp. 1-15.
- [99] E.C. Kurum, H.B. Dong, J.D. Hunt, *Metallurgical and Materials Transactions A-Physical Metallurgy and Materials Science* 36A (2005) 3103-3110.
- [100] Suyitno, D.G. Eskin, L. Katgerman, *Materials Science and Engineering A-Structural Materials Properties Microstructure and Processing* 420 (2006) 1-7.
- [101] D.R. Gunasegaram, A.K. Dahle, T.T. Nguyen, A.F.S. Afs, Mechanism of gap formation during solidification of commercial Al-Si alloys, in: *Transactions of the American Foundrymen's Society*, Vol 107, vol 107, 1999, pp. 257-263.
- [102] J. Ampuero, C. Charbon, F.A. Hoadley, M. Rappaz, *Materials Processing in the Computer Age* 17-21 February (1991) 377-388.
- [103] J. Ampuero, A.F.A. Hoadley, M. Rappaz, Numerical and experimental study of microporosity evolution during the solidification of metallic alloys, in: *Modelling of Casting, Welding and Advanced Solidification Processes*, vol V, 1991, pp. 449-454.
- [104] S.C. Flood, J.D. Hunt, *Met. Sci.* 15 (1981) 287-294.
- [105] H. Iwahori, K. Yonekura, Y. Yamamoto, M. Nakamura, *AFS Transactions* 98 (1990) 167-173.
- [106] P.N. Anyalebechi, *Scripta Metallurgica et Materialia* 33 (1995) 1209-1216.
- [107] P.N. Anyalebechi, *Scripta Materialia* 34 (1996) 513-517.
- [108] Q.T. Fang, P.N. Anyalebechi, D.A. Granger, *Light Alloys* (1988) 477-486.
- [109] X. Bian, Z. Zhang, X. Liu, *Materials Science Forum* 331 (2000) 361-366.

- [110] F.A. Fasoyinu, AFS Transactions 102 (1994) 515-528.
- [111] G.R. Wakefield, R.M. Sharp, Applied Surface Science 51(1-2) (1991) 95-102.
- [112] L.W. Huang, W.J. Shu, T.S. Shih, AFS Transactions 108 (2000) 547-560.
- [113] K. Shimizu, G.M. Brown, K. Kobayashi, P. Skeldon, G.E. Thompson, G.C. Wood, Corrosion Science 40(4-5) (1998) 557-575.
- [114] K. Shimizu, G.M. Brown, K. Kobayashi, P. Skeldon, G.E. Thompson, G.C. Wood, The nucleation sites of γ -Al₂O₃ crystals in thermal oxide films on aluminum, in: Proceedings of 1st Int.Conf. - Microscopy of oxidation, Cambridge UK, 1991, pp. 144-148.
- [115] C.N. Cochran, D.L. Belitskus, D.L. Kinosz, Metallurgical and Materials Transactions B 8B (1977) 323-332.
- [116] M.P. Silva, D.E.J. Talbot, Light Metals (1989) 1035-1040.
- [117] L. Liu, A.M. Samuel, H.W. Doty, S. Valtierra, AFS Transactions 110 (2002) 449-462.
- [118] J.P. Anson, R.A.L. Drew, J.E. Gruzleski, Metallurgical and Materials Transactions B-Process Metallurgy and Materials Processing Science 30 (1999) 1027-1032.
- [119] D. Emadi, J.E. Gruzleski, J.M. Toguri, Metallurgical Transactions B-Process Metallurgy 24 (1993) 1055-1063.
- [120] P. Mohanty, J.E. Gruzleski, Acta Materialia 44 (1996) 3749-3760.
- [121] N. Roy, L. Zhang, P.R. Louchez, F.H. Samuel, Journal of Materials Science 31 (1996) 1243-1254.
- [122] Q.T. Fang, D.A. Granger, AFS Transactions 97 (1989) 989-1000.
- [123] A. Knuutinen, K. Nogita, S.D. McDonald, A.K. Dahle, Journal of Light Metals 1 (2001) 241-249.
- [124] R. DasGupta, ASM Handbook, ASM International Handbook Committee © 2008 ASM International, 2008.
- [125] L.F. Mondolfo, Metallography of aluminum alloys, John Wiley & Sons, Inc., New York, 1943.
- [126] J.P. Anson, J.E. Gruzleski, Materials Characterization 43 (1999) 319-335.
- [127] K.M. Hanson, Journal of Computer Assisted Tomography 4 (1980) 361-363.
- [128] B.P. Flannery, W.G. Roberge, Journal of Applied Physics 62 (1987) 4668-4674.

- [129] P. Cloetens, R. Barrett, J. Baruchel, J.P. Guigay, M. Schlenker, *Journal of Physics D-Applied Physics* 29 (1996) 133-146.
- [130] L. Salvo, P. Cloetens, E. Maire, S. Zabler, J.J. Blandin, J.Y. Buffiere, W. Ludwig, E. Boller, D. Bellet, C. Josserond, *Nuclear Instruments & Methods in Physics Research Section B-Beam Interactions with Materials and Atoms* 200 (2003) 273-286.
- [131] A. Chaijaruwanich, R.J. Dashwood, P.D. Lee, H. Nagaumi, *Acta Materialia* 54 (2006) 5185-5194.
- [132] A. Chaijaruwanich, P.D. Lee, R.J. Dashwood, Y.M. Youssef, H. Nagaumi, *Acta Materialia* 55 (2007) 285-293.
- [133] G. Couturier, M. Rappaz, Modeling of porosity formation in multicomponent alloys in the presence of several dissolved gases and volatile solute elements, in: *TMS Annual Meeting, San Antonio, TX, 2006*, pp. 143–152.
- [134] A.B. Phillion, S.L. Cockcroft, P.D. Lee, *Materials Science and Engineering A-Structural Materials Properties Microstructure and Processing* 491 (2008) 237-247.
- [135] A.B. Phillion, S.L. Cockcroft, P.D. Lee, *Scripta Materialia* 55 (2006) 489-492.
- [136] S. Terzi, L. Salvo, M. Suery, N. Limodin, J. Adrien, E. Maire, Y. Pannier, M. Bornert, D. Bernard, M. Felberbaum, M. Rappaz, E. Bollerr, *Scripta Materialia* 61 (2009) 449-452.
- [137] D. Kakas, L. Kovacevic, P. Terek, D. Krumes, Z. Kolumbic, *Metalurgija* 48 (2009) 171-174.
- [138] L. Liu, A.M. Samuel, F.H. Samuel, 38 (2003) 1255-1267.
- [139] E. Niyama, T. Uchida, M. Morikawa, S. Saito, *AFS Int. Cast Met. J.* 9 (1982) 52-63.
- [140] P. Vo, Mathematical modeling of microporosity in A356 aluminum alloy, in: *Department of Materials Engineering, Master of Applied Science, Univeristy of British Columbia, Vancouver, 2001*.
- [141] W.S. Pellini, *AFS Trans.* 61 (1953) 1157-1165.
- [142] N. Roy, P.R. Louchez, F.H. Samuel, *Journal of Materials Science* 31 (1996) 4725-4740.
- [143] D.R. Irani, V. Kondic, *AFS Trans.* 77 (1969) 208-211.
- [144] Y.W. Lee, E. Chang, C.F. Chieu, *Metallurgical Transactions B-Process Metallurgy* 21 (1990) 715-722.
- [145] V. Laurent, C. Rigault, *AFS Trans* 100 (1992) 647-655.

- [146] J.A. Spittle, M. Almeshhedani, S.G.R. Brown, *Cast Met.* 7 (1994) 51-56.
- [147] V.K. Suri, A.J. Paul, N. El-Kaddah, J.T. Berry, *AFS Trans* 102 (1995) 861-867.
- [148] G.K. Sigworth, C. Wang, H. Huang, J.T. Berry, *AFS Trans.* 102 (1995) 245-261.
- [149] K. Kubo, R.D. Pehlke, *Metallurgical Transactions B-Process Metallurgy* 16 (1985) 359-366.
- [150] A.S. Sabau, S. Viswanathan, *Metallurgical and Materials Transactions B-Process Metallurgy and Materials Processing Science* 33 (2002) 243-255.
- [151] G. Backer, Q.G. Wang, *Metallurgical and Materials Transactions B-Process Metallurgy and Materials Processing Science* 38 (2007) 533-540.
- [152] J.D. Zhu, S.L. Cockcroft, D.M. Maijer, *Metallurgical and Materials Transactions A-Physical Metallurgy and Materials Science* 37A (2006) 1075-1085.
- [153] J. Ni, C. Beckermann, *Metallurgical Transactions B-Process Metallurgy* 22 (1991) 349-361.
- [154] S.D. Felicelli, L. Wang, C.M. Pita, E.E. De Obaldia, *Metallurgical and Materials Transactions B-Process Metallurgy and Materials Processing Science* 40 (2009) 169-181.
- [155] J. Huang, T. Mori, J.G. Conley, *Metallurgical and Materials Transactions B-Process Metallurgy and Materials Processing Science* 29 (1998) 1249-1260.
- [156] S. Pan, W. Liou, A. Shih, M.S. Park, G. Wang, S.P. Newberry, H. Kim, D.M. Shinozaki, P.C. Cheng, *Microscopy and Microanalysis* 4 (1998) 56-62.
- [157] L.A. Feldkamp, L.C. Davis, J.W. Kress, *Journal of the Optical Society of America A-Optics Image Science and Vision* 1 (1984) 612-619.
- [158] S. Thompson, S.L. Cockcroft, M.A. Wells, *Materials Science and Technology* 20 (2004) 194-200.
- [159] L. Orgeas, J.P. Gabathuler, T. Imwinkelried, C. Paradies, M. Rappaz, *Modelling and Simulation in Materials Science and Engineering* 11 (2003) 553-574.
- [160] B. Zhang, D.M. Maijer, S.L. Cockcroft, *Materials Science and Engineering A-Structural Materials Properties Microstructure and Processing* 464 (2007) 295-305.
- [161] S.V. Akhonin, N.P. Trigub, V.N. Zamkov, S.L. Semiatin, *Metallurgical and Materials Transactions B-Process Metallurgy and Materials Processing Science* 34 (2003) 447-454.
- [162] W. Kurz, D.J. Fisher, *Fundamentals of Solidification*, Trans. Tech. Publications, Switzerland, 1986.

- [163] J. Campbell, M. Tiryakioglu, *Materials Science and Technology* 26 (2010) 262-268.
- [164] C.M. Dinnis, M.O. Otte, A.K. Dahle, J.A. Taylor, *Metallurgical and Materials Transactions A-Physical Metallurgy and Materials Science* 35A (2004) 3531-3541.
- [165] N.W. Lai, W.D. Griffiths, J. Campbell, Modeling of the potential for oxide film entrainment in light metal alloy castings, in: *10th International Conference on Modeling of Casting, Welding and Advanced Solidification Processes*, 2003.
- [166] PoDFA user's manual, ABB Inc., March 1999.